A Flow Field Study of a Film Cooling Hole Featuring an Orifice

Yingjie Zheng

A Thesis

in

The Department

of

Mechanical and Industrial Engineering

Presented in Partial Fulfilment of the Requirements

For the Degree of Master of Applied Science

Concordia University

Montréal, Québec, Canada

December 2013

CONCORDIA UNIVERSITY
School of Graduate Studies

This is to certify that the thesis prepared

By: Yingjie Zheng

Entitled: A Flow Field Study of a Film Cooling Hole Featuring an Orifice

and submitted in partial fulfillment of the requirements for the degree of

Master of Applied Science (Mechanical Engineering)

complies with the regulations of the University and meets the accepted standards with respect to originality and quality.

Signed by the final examining committee:

Dr. M. Medraj _____ Chair

Dr. H. D. Ng _____ Examiner

Dr. O. Ait Mohamed _____ Examiner

Dr. I. Hassan _____ Supervisor

Approved by _____
Chair of Department or Graduate Program Director

_____
Dean of Faculty

Date _____

Abstract

A Flow Field Study of a Film Cooling Hole Featuring an Orifice

Yingjie Zheng

Concordia University, 2013

Film cooling is a jet-in-crossflow application in gas turbines used to protect high temperature parts. Understanding the physical phenomena in the flow field, for example the detrimental counter-rotating vortex pair, is highly critical. Experimental investigations were conducted using stereoscopic PIV to study the flow field downstream from film cooling holes featuring an orifice, under blowing ratios from 0.5 to 2.0. The original geometry of a short injection hole that was proposed in a previous numerical study was examined. The results reported a significant reduction in counter-rotating vortex pair strength of nozzle hole injection in comparison with cylindrical hole injection. The streamwise vorticity of the nozzle hole jet averaged a drop of 55% at a low blowing ratio of 0.5, and a 30%–40% drop at high blowing ratios of 1.0, 1.5 and 2.0. Due to the reduction in counter-rotating vortex pair strength, a round jet bulk was observed forming from the two legs of a typical kidney-shaped jet. The merged jet bulk delivered better coverage over the surface.

The effect of the geometrical parameters of the orifice and the effect of the blowing ratio were also investigated using long injection hole geometry to isolate the impact of the short hole length. It was found that under high blowing ratio conditions, no structural difference occurred in the jet when altering the value of blowing ratio. The most important geometrical parameters were the opening width and the in-hole position of the orifice. The measurement results suggested that the width of the orifice had a major impact on downstream counter-rotating vortex pair strength, and the in-hole position of the orifice mainly affected the penetration characteristics of the jet. The mechanism of the counter-rotating vortex suppressing effect of the orifice was studied from the flow field data. It is proven that the orifice greatly eliminated the hanging vortices developing from the in-hole boundary layer vorticity, which was the major contributor to counter-rotating vortex formation in inclined jets.

Contents

List of Figures

List of Tables

Nomenclature

AR	Area ratio of exit and inlet
a	Interrogation window dimension (pixel)
BR	Blowing ratio
DR	Density ratio
D_0	Object distance (mm)
d	Diameter (mm)
f	Focal length (mm)
F	Magnification factor
I	Momentum flux ratio
L	Injection hole length (mm)
Ma	Mach number
$\dot{m}$	Mass flow rate (kg/s)
n	Turbulent flow velocity approximation index
P	Static pressure (psi); Orifice in-hole position (mm)
p	Pitch of CCD pixel (pixel)
Q	Volume flow rate (CFM); Q value for vortex identification

Re	Reynolds number
r_p	Overall pressure ratio across compressor stages
S	Strain rate tensor, $(\partial v/\partial z + \partial w/\partial y)/2$
T	Static temperature (°C, K)
t	Light sheet thickness (mm), time (s)
TI	Turbulence intensity
U_j	Mean velocity of jet (m/s)
U_m	Mean velocity of mainstream (m/s)
U, u	X-direction velocity component (m/s)
$\vec{U}$	Velocity vector (m/s)
V, v	Y-direction velocity component (m/s)
W, w	Z-direction velocity component (m/s); Orifice opening width (mm)
x	Streamwise position (mm)
y	Altitudinal position (mm)
z	Spanwise position (mm)
α	Injection angle; camera tilt-shift angle (deg)
η_{cyc}	Cycle thermal efficiency
η_f	Film cooling effectiveness
η_{poly}	Stage polytropic efficiency
φ	Coolant flow rate fraction
ρ	Density (kg/m^3)
θ	Camera mount angle (deg)
ω	Vorticity (1/s)

ω^*	Dimensionless vorticity, normalised by U_m and d
Ω	Vorticity tensor, $(\partial v/\partial z - \partial w/\partial y)/2$

Subscripts

j	Jet
m	Mainstream
x	X-component
y	Y-component
z	Z-component

Abbreviation

CRVP	Counter-rotating vortex pair
DLT	Direct linear transformation
GTCC	Gas turbine combined cycle
JICF	Jet in crossflow
TIT	Turbine inlet temperature

Chapter 1

Introduction

1.1 Background

In the recent developments of gas turbines, Mitsubishi Heavy Industry (MHI) has achieved a record high turbine inlet temperature (TIT) of 1600 °C on its "J-Series" gas turbines. Hada et al. (2012) reported the world's highest gross thermal efficiency of over 61.5% during the test operation of J-Series gas turbine combined-cycle (GTCC) power generation. MHI's 1700 °C class gas turbines, currently under development, aim to provide 62–65% thermal efficiency in a GTCC. The tremendously high TIT plays a pivotal role in achieving such great efficiency. Apart from industrial applications, aviation applications demand high-efficiency gas turbines, as well in the consideration of fuel costs and emissions. Due to the restriction of weight, aero engines have very limited measures to increase cycle thermal efficiency η_{cyc}. Utilising a heat recovery system as for ground use is not feasible in aero applications. Higher turbine inlet temperature is continuingly a highly effective solution. However, an increase in pressure ratio r_p across

compressor stages could provide a more significant performance boost. Efforts are also being made to find better aerodynamic designs in order to achieve higher turbine and compressor polytropic efficiency η_{poly} so as to increase cycle efficiency. Monotonically increasing TIT does not promise greater η_{cyc} due to the penalty for large amount of protective coolant injected into turbine stages. Advanced film cooling technology with higher cooling effectiveness η_f and reduced coolant flow rate fraction φ is in great demand for high-polytropic-efficiency, high-TIT and high-pressure-ratio gas turbines. Wilcock et al. (2005) created a comprehensive computer code, taking into account real gas model, and generated the cycle efficiency of a simple-cycle industrial turbine under various operating conditions, such as η_{poly}, TIT, r_p, η_f and φ. The authors pointed out that under the probable maximum achievable polytropic efficiency of around 92.5%, the current film cooling technology hinders gas turbines from achieving higher cycle efficiency at a specific TIT and r_p.

1.2 Motivation

As mentioned above, advanced film cooling technology is necessary for the development of high efficiency gas turbines. The heat transfer characteristics in film cooling are primarily the consequence of the cooling flow structure. Understanding the fundamentals of flow physics in film cooling will lead industry to the achievement of higher cooling effectiveness. Counter-rotating vortex pair (CRVP) is a key phenomenon in the flow field of film cooling and brings negative effect of

cooling performance as they entrain hot gas under the coolant and break the thermal barrier. The original source of CRVP formation is currently a subject of debate. Meanwhile, finding anti-CRVP injection hole designs is the focus of many researchers and industry actors. This thesis aims to provide insight into the flow structure of film cooling and to reveal the CRVP suppressing effect of a new anti-CRVP injection hole geometry equipped with an orifice. Finding new evidence for the major contributor to CRVP formation is also a consideration in this thesis.

Following the introductory chapter, Chapter 2 presents an extensive literature review of the basis of CRVP structure and anti-CRVP schemes. Chapter 3 introduces the approaches used in the present study, including experimental facilities, measurement procedures and data analysis methods. Chapter 4 reveals the velocity field and vorticity field downstream of the orifice-featured hole and the decrease of CRVP strength in comparison with the cylindrical hole. The effect of each geometrical parameter of the orifice on the flow structure is presented in Chapter 5. This chapter also describes the CRVP-suppressing effect of the orifice and provides evidence in determining a major contributor to CRVP formation. Chapter 6 concludes the work and suggests directions for future work.

Chapter 2

Literature Review

2.1 Jet in Crossflow and Film Cooling

Film cooling introduces coolant fluid into a hot gas mainstream through an injection hole. It is an application of jet in crossflow (JICF) with an inclination angle, though the applications of jet in crossflow are not limited to film cooling. Some other applications include: flow discharged from a chimney, fuel injection in combustor and lifting jet of a V/STOL aircraft. The interaction between jet and crossflow results in a complex flow field featuring many vortical structures. Fric and Roshko (1994) depict the flow structure in their study on JICF, as in Figure 2.1. As shown, the crossflow passes through the obstacle-like jet. A horseshoe vortex is therefore generated from the injection hole leading edge and goes downstream along the lateral edges. At the shear surface between the jet and the crossflow, vortex ring (shear-layer vortices) shedding occurs at a certain frequency. Downstream of the injection, there are counter-rotating vortex pair and wall-normal vortices (wake vortices) at both sides of the jet.

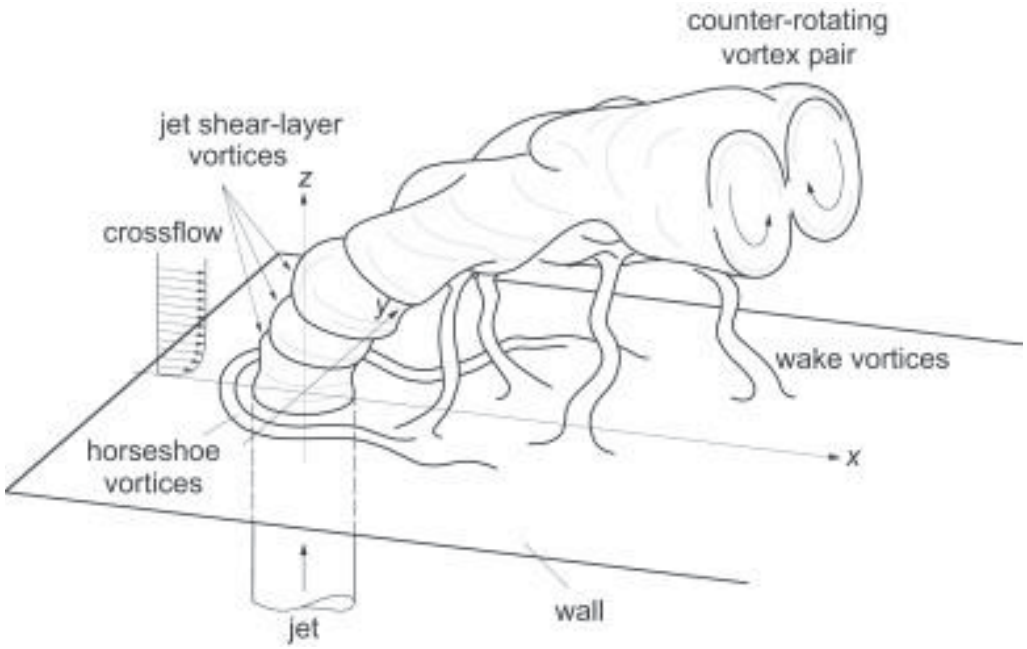

Figure 2.1: Flow structure of a jet in crossflow (Fric and Roshko 1994)

Different jet and crossflow parameters, such as density and velocity, may change the jet and vortex structure greatly. In a jet-in-crossflow problem, some important parameters are listed below. Density ratio is defined as:

$$DR = \frac{\rho_j}{\rho_m}$$

where ρ is fluid density, j and m are the subscripts for jet and crossflow. In the film cooling application-related sections, mainstream will refer to the crossflow.

Blowing ratio is defined to be the mass flux ratio of jet and crossflow as:

$$BR = \frac{\rho_j U_j}{\rho_m U_m}$$

where ρ is fluid density, and U is flow mean velocity.

Momentum flux ratio is defined to be the fluid momentum ratio of jet and crossflow as following:

$$I = \frac{\rho_j {U_j}^2}{\rho_m {U_m}^2}$$

The most phenomenal feature in the flow field downstream of injection is counter-rotating vortex pair, as shown in the above figure. Many applications have the demand of understanding CRVP formation mechanism and reducing the strength of CRVP. For example, in film cooling, the rotational motion of jet entrains hot gas under the jet bulk, wiping out the coolant coverage. Moreover, the two vortices mutually induce each other and cause upwash flow in the middle of the wake, therefore driving the coolant away from the surface. Hence, suppressing the effect of CRVP will directly help increase cooling performance.

In the early studies of CRVP formation, researchers held the opinion that the shearing effect between the two streams was the main cause of CRVP. The unmatched velocities of jet and crossflow interacted at the contacting surface where the jet was wrapped by the crossflow passing by. As the jet penetrated further into the crossflow, the wrapped portion at both lateral sides grew and bent to form the vortex pair. Later studies suggested that the origin of CRVP was not only in mainstream wrapping. Kelso et al. (1996) performed water tunnel investigation using flying-hot-wire and wind tunnel investigation using smoke visualisation. They suggested that the in-hole separation pattern was important in the initial roll-up of CRVP. The vortex ring in the jet-crossflow shear surface had contribution to a component of CRVP. The authors also pointed out the contribution of wall-normal vorticity component. They concluded that all the vortex ingredients had a certain connection to the formation of CRVP.

Marzouk and Ghoniem (2007) confirmed the roll-up in jet-crossflow shear layer as the source of CRVP according to the ensemble-averaged images in their transient numerical simulation. They reported that the crossflow entrainment was enhanced by the roll-up and formation of CRVP. In addition, they suggested that the upstream boundary layer separating around the jet and moving upward at the jet lee side was the origin of wake vortices.

The origin of CRVP is currently debated in the academia. Recently, Recker et al. (2010) conducted stereo PIV measurements on a perpendicular round jet in crossflow, which was motivated by a JICF application in hydrogen combustion. The application targeted "Micromix" hydrogen combustion optimisation in liquid hydrogen-fuelled aircraft. They suggested that the combination of hanging vortices (x-direction) at lateral edges, in-hole vortices (y-direction) and wake vortices (y-direction) was the origin of CRVP, in which the hanging vortices were major contributors. The in-hole vortices merged into wake vortices downstream. They used Q criterion technique to determine whether a vorticity was caused by vortex or shear. In addition to the primary CRVP, a secondary CVRP located above the primary was identified in some time frames. They also found that in the injection region, some crossflow entrained into the injection hole. At momentum ratio 1, the jet penetrated the crossflow by 2d.

Issakhanian et al. (2012) used magnetic resonance velocimetry, a non-instructive and non-optical flow field measurement technique, to obtain the volumetric flow field data of the secondary stream inside the injection hole at 30°, 60° and 90°. They found that a *4d* long injection hole was enough for the in-hole

flow to develop to a radial uniform flow after the separation caused by the acute angle of the hole inlet, which pushed the flow towards the upstream side wall. They documented the secondary flow in cross plane of the hole axis created by a pressure gradient, which was a result of the curved flow due to the separation mentioned above. Combining the in-hole flow patterns, the authors explained the mechanism of CRVP formation and confirmed the effect of hanging vortices and wall-normal vortices.

Studies are not limited to investigating the formation of CRVP. Schlegel et al. (2011) examined the effect of the crossflow boundary layer on the jet structure using numerical simulations, showing how the crossflow was entrained into the jet wake. They reported that in the case where there was a *0.5d* thick boundary layer, the jet roll-up occurred closer to the hole exit and the jet penetrated to a higher trajectory in comparison with a zero-thickness boundary layer case. They also showed the differences in wall-normal vorticity structures, where the boundary layer case had two clusters of vorticity, one along the hole edge and one downstream of the jet injection.

Film cooling has inclined jet injection, so it has some particular considerations with regards to the flow field. Walters and Leylek (2000) documented this in their numerical investigations, suggesting that the streamwise vorticity inside the injection hole boundary layer was the major contributing source for the formation of CRVP in film cooling flow field. The shear between the jet and the mainstream was not as significant as the in-hole vorticity for three reasons. The first was that film cooling injection was not like the offset jet away from the wall, where the

interaction with the high velocity mainstream was strong. Secondly, the film cooling application had a shallow discharge angle, and the wall-normal vorticity by the shear did not significantly realign to a streamwise direction, as in a vertical injection. The third was that the wall-normal vorticity generated by the interface was opposite to the wall-normal component of vorticity in the hole boundary layer. They also suggested that the turbulence in the near field had a significant effect on the diffusion and dissipation of the jet. At a low blowing ratio, turbulence was produced at the interface of the two flows due to the mismatched momentum of jet and mainstream. At a high blowing ratio, turbulence was mainly located at the inside of the hole. Regarding the effect of CRVP, they pointed out that it was opposite to the jet diffusion towards the lateral direction and towards the wall, which lowered the cooling effectiveness.

Bernsdorf et al. (2008) conducted an experimental study on the flow structure of a round jet. The flow field was measured by stereo particle image velocimetry (2D3C) in a closed-loop wind tunnel. The mainstream was heated up to 120 °C and the jet was cooled down to -50 °C, which enabled the variation of the jet-to-mainstream density ratio. Two different hole angles, 30° and 50°, were examined with varying blowing ratios, density ratios and momentum ratios. They suggested that under the same BR, the momentum flux ratio would decide the jet strength, and a high DR would entrain more low velocity fluid into the centre of the kidney-shaped jet. They also demonstrated the vorticity field of film cooling flow. It was also found that the surface vorticity revealed the dominant shear around the jet.

2.2 Flow Structure Altering Approaches

2.2.1 Shaped hole injection

In order to reduce CRVP strength, many anti-CRVP injection hole schemes have been proposed. Shaped hole is a commonly employed approach for reducing CRVP and jet lift-off, as a shaped hole has a diffusive exit section after the cylindrical entrance section. The diffusor section greatly reduces the jet flow momentum, resulting in a better lateral spreading and uniform coverage over the surface. The diffusor geometry designs vary from case to case. According to Bunker (2005), there are four main types of shaped hole geometry. The first type features both lateral expansion angle and forward-diffusion angle, which is the most common design of a shaped hole, often referred to as fan-shaped hole. The second type of shaped hole geometry has a diffusor section with only a lateral expansion angle. In contrast, the third type is designed only to have a forward-diffusion angle. Yet the lateral expansion angle is actually thought to have a better CRVP-suppression effect than the forward-diffusion angle. It plays a more important role in the first type of geometry. The last type of shaped hole does not have a separate entrance section and a diffusive section. It is basically a conical hole with gradually increasing diameter from inlet to exit.

The study of shaped hole approaches has drawn researchers' efforts for a long time. Haven and Kurosaka (1997) conducted water tunnel experiments of several shaped holes, presenting trends of how the hole shape affects jet lift-off

characteristics. A hole that was wider in its spanwise direction than its streamwise direction was more likely to have an anti-vortex feature. The wider exit separated vortices generated from the side wall inside the cooling hole, which means the mutual induction between the two vortices were weak. This study confirmed a better attachment to the flat plate of the secondary stream at a velocity ratio of 1.6.

Miao and Wu (2006) numerically investigated a cylindrical hole, forward diffused hole and lateral diffused hole on flat plate. It was reported that in the lateral diffused hole case at a blowing ratio of 1.5, almost no CRVP was observed, and consequently the best spanwise averaged film cooling effectiveness was achieved using a lateral diffused hole.

Porter et al. (2008) compared a round hole and a fan-shaped hole at low blowing ratios of 0.5 and 0.6 using hot-wire probes and two different CDF codes. The experimental results compared different turbulence intensity gradients from the wall. It was found the fan-shaped hole contributed to less mainstream-only turbulence intensity after $x/d = 6$, because the fan-shaped jet diminished quickly, in contrast to round jet's aggressive turbulence gradient further downstream, which suggested the round jet diminished slowly. They also compared the CFD results to the experimental results, which suggested the two-equation k-e turbulence model tended to underpredict turbulence intensity where large shear existed, such as in the boundary layer, since the RANS scheme averaged the high-turbulence intensity out. They pointed out the jet lateral contraction at the hole lateral edges at the examined blowing ratios, and considered it to be the acceleration effect exerted by the mainstream.

Kampe et al. (2013) conducted experimental and numerical investigations of the flow field of a diffuser-shaped film cooling hole using PIV, LDA and CFD. The data acquired from all three techniques were compared with each other. They investigated a cylindrical hole and a diffuser-shaped with an inclination angle of 35°. The lateral and forward angles of the diffuser portion were both 10°. The mainstream was heated to 330 K and 420 K to achieve different density ratios of 1.1 and 1.4. Regarding the flow field experiments, detailed PIV measurement uncertainties were listed. They documented the streamwise, wall-normal and lateral velocity components of the flow field. The diffuser-shaped hole showed less wall-normal momentum and it was reported that no jet lift-off was detected at a high blowing ratio of 2.0 and a density ratio of 1.1. The observation of lateral velocity distribution revealed less secondary flow velocity in comparison to the counter-rotating vortex structure downstream of the cylindrical hole. They also reported the bifurcation of the diffuser-shaped hole flow field, where a recirculation region existed in the middle of the two branches. The infrared thermal measurement in their study showed a cooling effectiveness three times higher with a diffuser-shaped hole.

2.2.2 Slot hole injection

In the very early stages of film cooling research, a coolant was designed to be issued from a rectangular slot on the blade surface. However, due to a weakness in structural strength, a complete slot geometry was almost impossible for an actual application. Oldfield and Lock (1998) proposed a modified slot hole geometry,

named the converging slot hole or console, which incorporated a round inlet and a slot-shaped exit. The inlet and exit were connected smoothly by gradual shape transformation. The adjacent exits were conjoined to forming a continuous slot that covered a large spanwise portion. In an early study of slot-hole film cooling, Sargison et al. (2002) presented the film cooling performance of a console injection at 35° using a thermochromic liquid crystal technique. The authors reported that the heat transfer coefficient distribution was similar to slot holes, but higher than cylindrical and shaped-hole injection. Moreover, it was suggested that the thin boundary layer of console injection was beneficial in aerodynamic loss characteristics compared to the thick boundary layer in cylindrical and shaped-hole cases. Sargison et al. (2005) visualised the film flow downstream of the console injection hole. The authors used a thermochromic liquid crystal technique to measure the temperature field and visualise the flow using water/dry-ice fog at engine operative conditions. They reported a strong similarity between the console and slot injection flow fields. No jet lift-off, as in cylindrical injection and coolant diffusion with shaped-hole injection, was found.

Azzi and Jubran (2007) performed a numerical investigation on the converging slot hole at blowing ratios of 0.5 and 1.0. The converging slot hole had an inclined angle of 35° and a total length of *1.75d*. The slot width was *0.2d* and the pitch was *3d*. The simulation results showed that the console injection had an impressive span-averaged film cooling effectiveness when compared with the cylindrical hole and shape-hole injection at both blowing ratios, especially in the near-exit region, where the effectiveness approached 1. The superiority of span-averaged effectiveness was

attributed to the uniform spanwise temperature distribution. The author also mentioned that the vortical structure of converging slot hole injection was completely from that of cylindrical and shaped-hole injection.

Liu et al. (2010) performed experimental investigations of converging slot-hole rows on a turbine blade and made a comparison with cylindrical injection. Several injection rows were configured on both sides of the blade to achieve complete coverage. The momentum flux ratio ranged between 1.1 and 4.0. Two coolant flux ratios were tested: 3% and 5%. The temperature fields were obtained using wide-band thermochromic liquid crystal. The authors concluded that the jet of the converging slot-hole injection was more resistant to the passage vortex due to great attaching characteristics. Also, because of the concave shape at the pressure side, the jet of the converging slot-hole showed an increasing trend as the momentum flux ratio increased. On the suction side, the jet flow tended to separate as coolant flux increased, while the film cooling effectiveness did not increase.

The original slot hole geometry is not structurally preferable in applications since the slot runs through from the outer surface to the inner surface, which drastically reduces structural strength. In order to solve this problem, Bruce-Black et al. (2009) proposed a practical slot hole geometry that only cuts partially into the material. The coolant was supplied through impinging tubes. Both continuous and discrete slots were investigated under a density ratio of 1.3 and blowing ratios ranging from 1.0 to 4.0. The authors reported that cooling effectiveness would increase as the slot width decreased at high blowing ratios in continuous slot injection, since the slimmer exit could offer better film uniformity and less

turbulence. For discrete slots, the effect of slot depth was stronger than slot width. On the other hand, decreasing hole diameter improved cooling performance for fixed slot width and depth. According to the authors, continuous slot injection generally performed better than discrete slots.

2.2.3 Compound-angle hole

Compound-angle injection is another approach to the problem of the vortex pairs downstream of the injection. The jet injection direction is inclined from mainstream direction, where the angle projected in wall-normal surface is referred to as the compound angle. In inclined injection, the vortices after injection are inclined from the mainstream direction as well. The impact of mainstream flow, such as impingement and blockage, changes the vortical structure significantly and yields weaker downstream vortices. In early study of compound-angle injection, Ligrani et al. (1994b) performed experimental measurements on a single row of injection holes with a compound angle orientation of 35°. The injection angle from the surface was 30°. The blowing ratio ranged from 0.5 to 1.5 and the density ratio was around 1.0. The authors investigated the effect of the compound angle value with constant spanwise spacing of holes, and vice versa. They reported little difference far downstream in the investigation of the effect of compound angle with constant spacing. The effect of spanwise spacing was obvious in terms of span-averaged cooling effectiveness.

Azzi et al. (2001) investigated the flow field and heat transfer characteristics numerically using a standard $k-\varepsilon$ turbulence model with wall functions. The

authors reported that at a low blowing ratio of 0.5, the span-averaged adiabatic cooling effectiveness decreased farther downstream. Yet in high blowing ratio cases, they suggested that jet lift-off, a well-known feature in the film cooling flow field, existed right after the coolant issued from the holes. This resulted in a decrease and increase of the spanwise cooling effectiveness downstream of the compound-angle holes. The authors also mentioned that farther downstream, higher blowing ratios (1.0 and 1.5) offered better film cooling performance than low blowing ratios. Generally, compound-angle injection was reported to provide superior performance than a streamwise injection configuration.

Aga et al. (2008) used stereo PIV to reveal the flow field of a compound-angle cylindrical hole at *M=0.3*; *BR=1,2,3*; *DR=1, 1.55*; *IR=0.64, 1, 2.6, 4, 6, 9*. They reported that the CRVP was eliminated due to compound-angle injection, and a jet with wider lateral spread for better film cooling effectiveness.. One vortex of the pair disappeared while the other became a large asymmetrical vortex. Although the large single vortex arose mainstream entrainment under the jet and may increase surface heat transfer in some regions, particularly along the line of compound angle, the spreading of coolant is greater than without streamwise injection hole, and film cooling effectiveness is increased. They also indicated that under the same BR, higher IR would result in a wider jet. In another study, Aga and Abhari (2011) used stereo PIV and IR cameras to investigate the flow field and film cooling effectiveness of single row of compound-angle cylindrical holes. The tested compound angles of 15°, 60° and 90°, blowing ratios from 1.0 to 2.0, and density ratios from 1.0 to 1.5. Flow field features similar to the above were observed, but along with cooling

effectiveness. With higher compound angles, up to 90°, greater jet spreading occurred and brought higher average lateral effectiveness, though near the hole a lower effectiveness was observed than 0 compound angle. On the other hand, the authors found that the great spreading of jet could counteract jet lift-off.

Compound-angle injection often incorporates basic cylindrical holes to make comparisons between them. Yet shaped holes can also be configured with compound angle orientations. Brittingham and Leylek (2000) compared the flow field and film cooling effectiveness of two shaped hole injections with a compound angle to that of a streamwise injection cylindrical hole. The first shaped hole had a forward-diffusion angle of 15° and was inclined in mainstream flow direction at 60°. The other shaped hole only had a lateral expansion angle of 12° and the compound angle was 45°. According to the authors, the effects of compound angle and shaped hole cannot be superposed directly. The shaped hole geometry had more weight in altering the flow structure. The flow field of such kinds of injection was highly complicated, and a minor change in hole geometry would bring a significant influence to the flow structure; often the change was not intuitively predictable due to non-linearity and non-uniformity. For example, the flow field of compound-angle forward-diffusion injection shared many similarities to streamwise cylindrical injections, characterised by only very basic film cooling performance. However, the compound-angle forward-diffusion injection featured superior span-averaged adiabatic cooling effectiveness.

A similar effect of shaped hole diffusion in compound-angle injection was reported in the work of Hyung et al. (2001). In this study, a compound-angle

cylindrical hole, a compound-angle conical hole and a compound-angle forward-diffusion hole were investigated experimentally and numerically for blowing ratios from 0.5 to 2.0. The compound angle ranges were 0°, 45° and 90°. The authors presented the velocity field of each case and suggested that the shaped holes weakened the CRVP greatly and hence limited the jet lift-off at the centre. Using Naphthalene Sublimation Method, they measured the mass transfer coefficient at the plate surface to determine heat transfer characteristics. The authors confirmed a lower mass/heat transfer coefficient in shaped hole cases due to the contribution of jet diffusion. Additionally, the cooling performance was reported to increase as the compound angle increased. However, the use of shaped hole at compound angle was not necessarily helpful at low blowing ratios, because the low momentum led to similar flow structures across different injection configurations.

2.2.4 Double rows of injection holes

In many cases, compound-angle injection holes are arranged in a configuration of two staggered rows in order to further improve performance. The jet from the upstream injection hole interacts with the jet of downstream injection hole. Since both holes inject coolant at a compound angle, usually in opposite directions, the counteraction between the jets results in more uniform jet spreading, lower vorticity and lower jet trajectory. Ligrani et al. (1994a) constructed a flow field development downstream of two staggered rows of compound-angle injection holes from their experimental results of mass transfer measurements. The holes of each row had a spacing of *3d*. The injection angle was 30° and the compound angle was

35°. The blowing ratio and density ratio were 0.5 – 1.5 and 1.0, respectively. The investigation is similar to the single-row compound-angle hole study mentioned in the previous section. Similar coolant coverage results were obtained far downstream, as in the single-row case. Near the injection region, the double-row configuration demonstrated better cooling performance than the single-row configuration.

Kusterer et al. (2007) performed numerical simulations on the flow field downstream of two consecutive cylindrical injection holes. The upstream and downstream holes had compound angles of 45° and -45°, respectively. 0d, 1d and 2d offset was applied to the alignment of the holes. The blowing ratio was set to approximately 1.7. The authors reported that the offset had a strong effect on the vortex structure. For the offset of 1d and 2d, similar counter rotating vortex structures were observed, as in the single streamwise cylindrical injection jet. Yet, in the 0d offset case, an anti-CRVP vortex pair was found, which contributed to a reduction of downstream vortex strength and improved coolant spanwise spreading. The temperature field data confirmed better cooling effectiveness in the 0d offset case. The authors also introduced the double-jet configuration to the suction side of a realistic turbine blade. It was reported that the double-jet could successfully replace a row of shaped holea in terms of cooling performance.

A similar configuration was numerically investigated by Graf and Kleiser (2011) using a Large-Eddy Simulation. The authors pointed out that the two jets, upstream and downstream, did not mix well. Instead, they showed strong individuality in downstream region, as the upstream jet took a narrow and tall form as a result of

similar exit conditions as the single-hole injection, while the downstream jet became widely distributed and flat due to the strong vortex and downwash effect of the upstream jet. In a follow-up work, Graf and Kleiser (2012) presented a highly detailed flow field analysis of double rows of compound-angle injection. They demonstrated the importance of vortex structure inside the injection holes, with which the anti-CRVP vortices were associated. The authors applied novel techniques to identify the jet trajectory in the boundary layer and demonstrated a link between the trajectory and film cooling effectiveness.

Some studies are focused on the double row configuration without compound angles. The interaction of upstream and downstream streamwise injection jets also shows noteworthy features and effects on flow field and film cooling performance. Asghar and Hyder (2011) used the standard $k-\varepsilon$ model to simulate two staggered rows of semi-cylindrical holes in order to weaken CRVP. Both rows of holes were aligned to the mainstream flow direction and the injection angle was 30°. The semi-circular holes issued half the amount of coolant of a complete circular hole. The simulation results show that the vortical strength was effectively reduced and the jet from double-row injection had a lower trajectory than a single cylindrical streamwise injection. Additionally, the centreline effectiveness was found to be much higher than that of typical cylindrical holes. The centre line and span-averaged cooling effectiveness downstream for double-row injection were found to be much higher than for a single row cylindrical hole.

2.2.5 Accompanying holes

Compound-angle injection takes advantage of the combination of coolant holes and the interaction of multiple jets to minimize the counter rotating vortex pair. The combination of holes can also be in the form of branching holes, often referred to as sister holes or triple jets. Two accompanying injection holes of smaller diameter are assigned to the main injection hole at both lateral sides. The injection direction of these branches can be either streamwise or at a compound angle. The inlet of the accompanying holes can be either at the plenum or at the main injection hole tube. Vortices of opposite direction to the main CRVP are generated through the accompanying holes. This concept was first proposed by Heidmann (2008) from the NASA Glenn Research Center as an anti-vortex film cooling hole. The accompanying holes were initially designed near the main hole exit, but since the pressure was low in that region, the branches face a problem of insufficient coolant. In a later design, the accompanying holes were relocated upstream of the main hole. Heidmann and Ekkad (2008) conducted a numerical investigation of both designs at a blowing ratio of 1.0 and density ratio ranging from 1.05 to 2.0. The author presented area-averaged streamwise vorticity over the range. They reported that the initial design had minor effect in reducing main jet CRVP, while the modified design showed strong anti-vortex characteristics, as the average vorticity hit the opposite direction to the main jet vorticity. On the other hand, the modified design significantly increases downstream span-averaged cooling effectiveness from 0.15 to 0.25 at a density ratio 1.05 and 0.2 to 0.35 at higher density ratio of 2.0.

Dhungel et al. (2009) experimentally investigated several accompanying hole designs using a transient infrared thermography technique in a wind tunnel. The designs included the original Heidmann spanwise-injection anti-vortex hole and the author's modification, according to which the accompanying holes were oriented at a compound angle between streamwise orientation and spanwise orientation. Different accompanying hole diameters were tested, and blowing ratios ranged from 0.5 to 2.0. It was documented by the authors that accompanying holes with relatively large diameters and early branching from the main hole tube demonstrated better performance than single cylindrical injection at all blowing ratios, especially at 2.0, since jet-lift caused it almost no film cooling from single cylindrical injection. Although compared to shaped hole injection, the performance boost from adding anti-vortex accompanying holes was not obvious, the machinability of round holes earned points.

In the numerical investigation conducted by Farhadi-Azar et al. (2011), a combination of three rectangular injection holes was positioned vertical to the mainstream. The small accompanying holes were located slightly downstream to the main hole on both sides. The main hole had a broad exit aspect ratio while the accompanying holes had longer edge in streamwise direction. The authors pointed out that each of the three holes produce a pair of counter rotating vortices. The two lateral ones counteracted the major pair in the middle, resulting in small-size CRVP and less mixing between the jets and the mainstream. The sensitivity to density ratio and velocity ratio was also investigated. Increasing the density ratio of accompanying jets benefited downstream heat transfer characteristics. Increasing

the velocity ratio of accompanying jets further brought down the main jet towards the surface and enhanced film cooling.

2.2.6 Vortex generator

Some researchers have introduced an extra device to the injection hole to alter the flow structure and counteract downstream CRVP. These devices often generate extra vortices with an opposite rotation to the CRVP. Zaman et al. (2010) studied the vortex generator placed downstream from the injection hole. They used hot-wire anemometry to investigate the flow field with varying vortex generator geometry, location and momentum flux ratio. They suggested that the vortices produced by the vortex generator had opposite sense to CRVP, which effectively cancelled the CRVP. Actually, in their results, the anti-vortex pair was too strong, and exceeded the needs for cancelling CRVP. They suggested a smaller one would be enough. The anti-vortex pair drew the jet towards to the wall, but due to turbulence, the jet core dissipated quickly, which could also be considered a consequence of excessive vortex generator size.

Shinn and Pratap Vanka (2013) numerically investigated a similar vortex generator geometry using a Large Eddy Simulation for two jet flow configurations. One configuration employed precursor simulation to the jet and the second a plenum as commonly used in most computational works. The authors reported that in the case of vortex generator, downwash flow was created by the vortices created by the vortex generator, resulting in enhanced film cooling effectiveness. The authors also pointed out a common problem when comparing computational and

experimental results. The difference in the boundary layer of upstream crossflow could lead to discrepancy in the downstream region between experimental and CFD results.

An et al. (2013) investigated an anti-vortex scheme featuring a crescent-shaped block downstream from the injection hole. The block generated an extra pair of vortices with an opposite sense to the CRVP and also improved the lateral spreading of coolant. They used mass a transfer analogy to predict the heat transfer phenomena. Pressure sensitive paint was used in the experiments to measure the concentrations of different gases. Over a blowing ratio ranging from 0.5 to 1.25, the block-featured configuration demonstrated better lateral cooling effectiveness, therefore resulting in improved lateral averaged cooling effectiveness. The authors also summarised the effect of each geometrical parameter of the crescent-shaped block.

2.3 The Nozzle Hole Scheme

In previous flow structure altering and anti-CRVP approaches, shaped hole injection featured a different exit local blowing ratio and momentum flux ratio from the hole inlet, since the nominal BR and I were calculated based on the cylindrical part before the shaped part of the hole. Compound angle hole injected jet fluid at an angle to the mainstream direction, and some schemes employed additional holes that had multiple jets. Studies that focus on the particular effects of CRVP on flow structure of single injection in a classic round-jet-in-crossflow arrangement are rare. In order to study the sole effect of CRVP strength on film cooling performance, Li et

al. (2011) proposed a new film cooling hole geometry, referred to as the nozzle hole scheme. The orifice changes the in-hole flow structure before injection, and the round exit issues jet fluid like a cylindrical hole does. This keeps the blowing ratio and momentum flux ratio the same from hole inlet to exit, enabling a better understanding of the particular effect of CRVP. Li et al. (2011) performed a CFD simulation using a RANS turbulence model to investigate the nozzle hole. The results showed a remarkable CRVP strength reduction and a cooling effectiveness increase in comparison to the cylindrical hole. It was reported that at all the studied blowing ratios, the nozzle hole demonstrates an impressive increase in performance, though the improvement is more obvious at higher blowing ratios. The nozzle hole achieved a cooling effectiveness of 0.10 – 0.15, while the effectiveness provided by a cylindrical hole is almost zero.

2.4 Summary and Objectives

Film cooling is an important application of jets in crossflow. A major phenomenon in film cooling flow field is the counter-rotating vortex pair, which has been well recognised as a critical and detrimental factor to film cooling effectiveness. The origin of CRVP has interested many researchers and is continuously argued about in academia. Due to the determinate effect on film cooling performance, dozens of studies have been conducted on suppressing CRVP and improving film cooling effectiveness. The nozzle hole, an orifice-based anti-CRVP scheme, was proposed by Li et al. (2011). The scheme can help better understand the evolution and effect of CRVP due to its unique design. Meanwhile, superior performance was demonstrated

in the application of nozzle hole using a CFD simulation. The present study looks into the flow field using experimental methods. The objectives of the present study are to:

- Experimentally examine the flow field downstream of the nozzle hole.
- Compare the flow field of nozzle hole and cylindrical hole.
- Propose explanations for the CRVP suppression effect of an orifice.
- Investigate the effect of geometrical parameters of orifice injection hole on the flow field and CRVP suppression performance.

Chapter 3

Experimental Investigations

The experimental investigations were conducted in an open loop low-speed wind tunnel. The wind tunnel is versatile and serves different measurement types, including velocity field measurement and temperature field measurement for both flat plate configuration and vane configuration. It has been used in many previous investigations involving thermal measurement, such as Ghorab et al. (2011) and Elnady et al. (2013). The present experiments involved several modifications to the wind tunnel in order to better serve the emphasis on the flow field of film cooling. The velocity field measurement was achieved using Particle Image Velocimetry (PIV). This chapter presents the wind tunnel system and the PIV system, as well as the procedures and concerns of measurement and data processing.

3.1 Wind Tunnel Facility

The schematic diagram of the wind tunnel is shown in Figure 3.1. Three major branches constitute the wind tunnel: mainstream path, secondary stream path and

seeding particle path. A compressor and reservoir system supply all the branches. The seeding particle path is a sub-branch of the secondary stream path and isolated by pressure regulator to precisely adjust the pressure inside the seeding material container.

The mainstream path employs a pressure regulator to adjust pressure and flow rate. A digital flow meter (Rosemont 3095 MV) provides comprehensive measuring information, such as volumetric flow rate Q_1, static pressure P_1 and static temperature T_1. Mainstream density at the point of flow meter ρ_1 is then calculated from static pressure and static temperature using the equation of state. Mainstream mass flow rate $\dot{m}_m$ is then obtained from Q_1 and ρ_1. Detailed condition parameters are stated in the results and discussion chapter.

Mainstream airflow goes through a divergent-convergent section to damp possible instability of the air supply system, especially in the situation when the reservoir has low air amount and the compressor is engaged, since the compressor produces periodical gushes. Following the DC section, a turbulence grid is installed before airflow entry to a 1.6 m long entrance section with a rectangular cross section, measuring 99 × 53 mm. At the end of the entrance section, there is a flange for mounting various test sections. Test sections can be straight and rectangular for flat plate investigation, such as in the present study, or a cascade-simulating section for on-vane measurement. An extraction system is installed near the test section exit to remove the airflow seeded with oil-based particles for PIV measurement.

The currently utilised test section has a rectangular flow path as shown in Figure 3.2, measuring 550 mm long (x-direction), 99 mm wide (z-direction) and 53

mm high (y-direction). It is made of acrylic to provide necessary optical access. The top and bottom plates are removable for convenience in experiment operations, and the removability makes it easy to clean the section as well, which is important for optical access. A square open is positioned 180 mm from the inlet of the test section for mounting the assembly of hole module and plenum. The plenum is basically a cubic chamber measuring 64 × 64 × 50 mm. It has a diverter (not shown in the figure) inside to fill up the plenum uniformly without directly jetting out the secondary stream towards the injection hole inlet. Thermocouples can be installed in the plenum to monitor flow temperature.

The secondary stream path uses an adjustable rotameter at location 3 to adjust its flow rate. Secondary stream mass flow rate is obtained by the same means as for the mainstream. The parameters used for mass flow rate calculation were read from another rotameter and a pressure gauge at location 2. The secondary stream temperature at the pressure gauge is taken at ambient room temperature of 21 °C. The rotameter is designed to give a direct flow rate reading at a back pressure of 1 atm, or zero gauge pressure. Since the plenum and injection hole create resistance to the flow, a correlation provided by the manufacturer is necessary to obtain correct flow rate. The correlation is as following:

$$flow\ rate = flow\ rate\ reading\ \times \sqrt{\frac{14.7}{back\ pressure + 14.7}}$$

where the back pressure unit is *psi* and read at P_2.

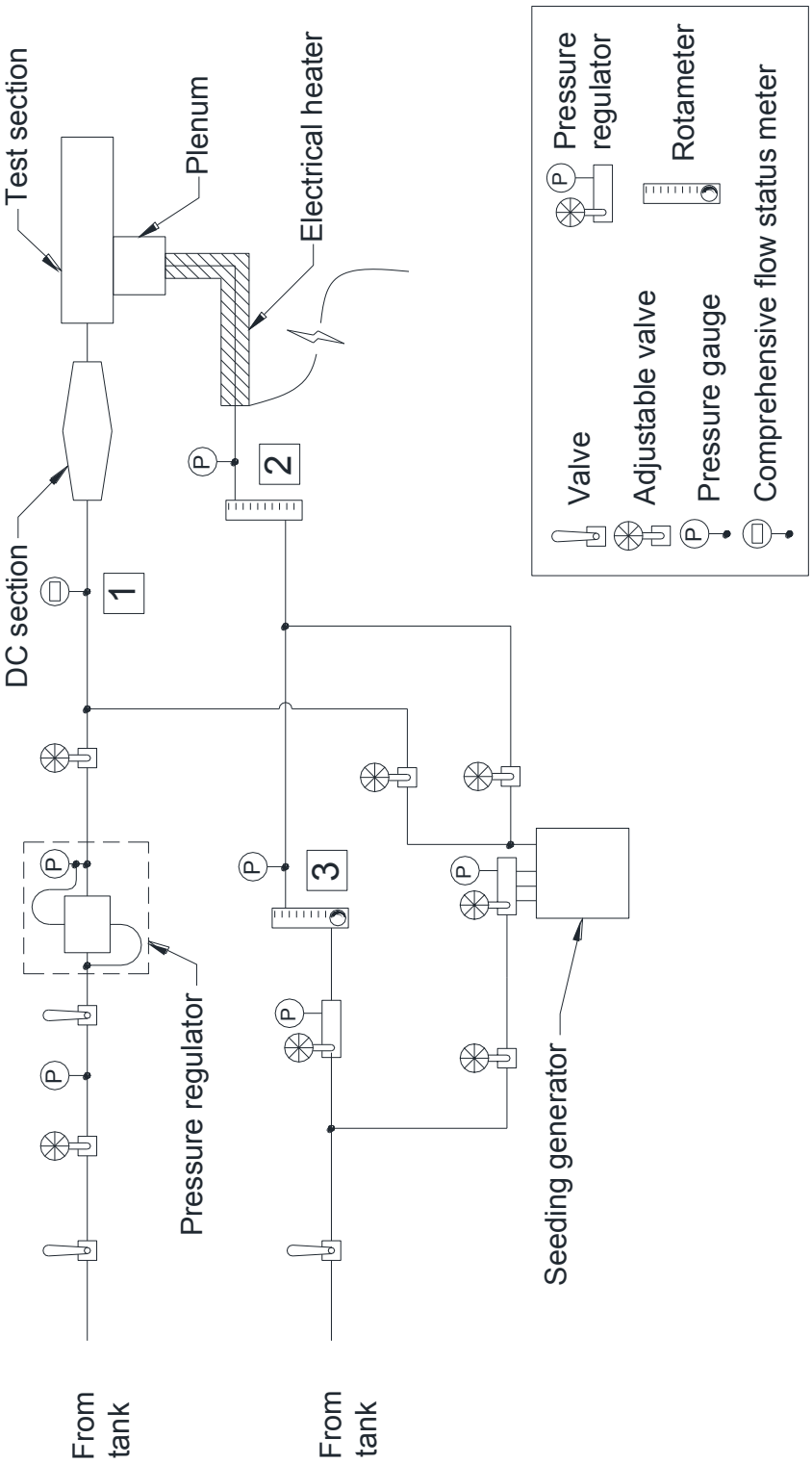

Figure 3.1: Schematic of the wind tunnel

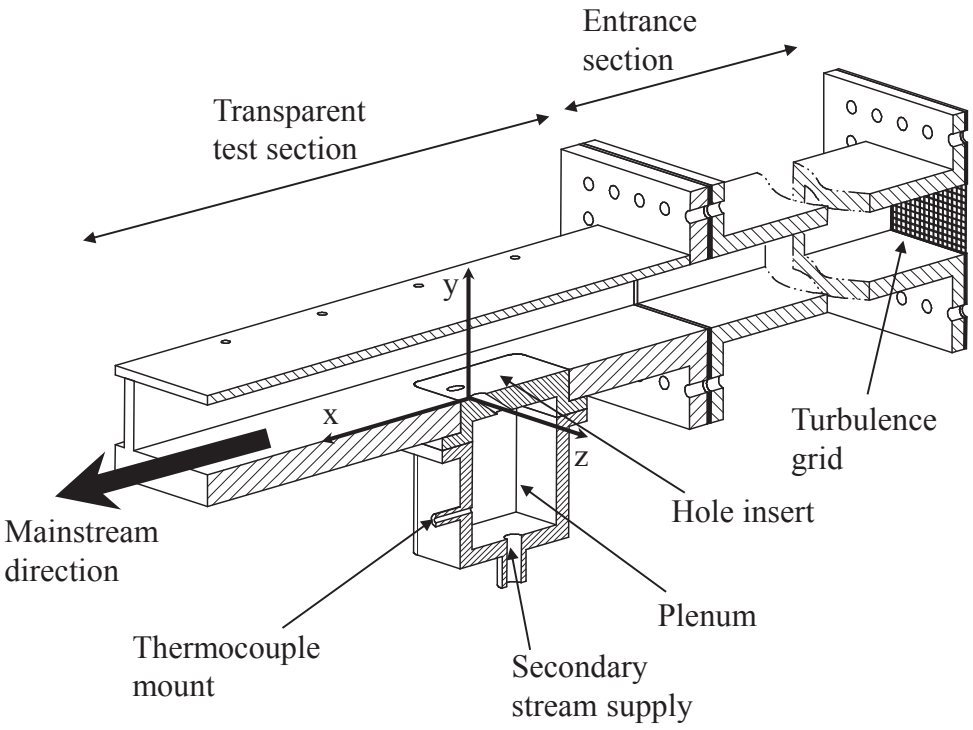

Figure 3.2: Test section

3.2 Particle Image Velocimetry

Particle Image Velocimetry tracks the velocity of the particles dispersed in a flow field to determine the fluid velocity. The particles are illuminated by a laser sheet and captured by cameras. The most common recording technique is double-frame single exposure, by which a pair of two sequential images is recorded. Some other recording techniques are single-frame double exposure or single exposure, where only one image is taken and particle movement appears as either a shifted location or as a streak, respectively. It can also be multi-frame and single/double exposure. Different recording techniques require different image processing methods. In the present study, double-frame single exposure is used. PIV techniques can be categorised into either steady measurement and transient measurement. The former presents a time-average velocity map, while the latter can provide the flow field development along the time axis. For each category, 2D2C measurement, often referred to as 2D PIV, provides a two-dimensional velocity map with two velocity components. 2D3C measurement, often referred to as stereoscopic PIV, is able to measure all the three velocity components on a two-dimensional plane.

The camera captures two sequential images with a well-controlled time interval, and the images are divided into many interrogation windows. The particles in each window are analysed to compute the movement for that window. The velocity of the particle is hence calculated according to the time interval between the two sequential images. The PIV algorithm determines a statistical displacement vector for each interrogation window instead of tracking the displacement vector of each

individual particle. The statistical velocity result of the interrogation window offers a more robust measurement than outputting each particle's velocity. A common analysis approach to the images is the cross-correlation method, which is widely used in the signal process. In PIV data processes, the Cartesian coordinate axis can be analogous to the time axis in signal process. Cross-correlation is also the basis of other PIV correlations, such as the adaptive correlation used in the present investigations. The cross-correlation function can be expressed as follows:

$$R(\Delta x, \Delta y) = \sum_{x=-\infty}^{x=\infty} \sum_{y=-\infty}^{y=\infty} f(x, y) \cdot g(x + \Delta x, y + \Delta y)$$

where f and g are the first and second image frame respectively.

The process could be imagined as finding a function through which the particle pattern in the first frame shifts to the new location in the second frame. A large summation operation is required, which consumes a lot of time. Fast Fourier Transform is thus often used to shorten this process by transforming the signal into a spatial frequency domain.

Since seeding particles may not have the same density as the fluid carrying them, considering the gravitational acceleration and local acceleration in the flow, velocity difference may occur between the particles and the fluid. The particle's success at tracing the fluid velocity is very important in PIV measurement. Due to small diameter of the particles, the Reynolds number of the fluid around a single particle is very low, so Stoke's law is applied to calculate the settling velocity of particles in fluid as follows:

$$U_s = U_p - U_f = d_p^2 \frac{\rho_p - \rho_f}{18\mu} a$$

where U_s is the settling velocity of particle, U_p and U_f are particle and fluid velocity, ρ_p and ρ_f are particle and fluid density, d_p is particle diameter, μ is fluid dynamic viscosity, and a is acceleration. The response of particles to velocity change in the flow can be expressed as

$$\frac{U_p}{U_f} = 1 - exp(-\frac{t}{\tau_s})$$

and τ_s is relaxation time as

$$\tau_s = d_p^2 \frac{\rho_p}{18\mu}$$

Figure 3.3 plots the response of particles of various diameters. It can be seen that small particles have better tracing characteristics compared to bigger ones of the same density.

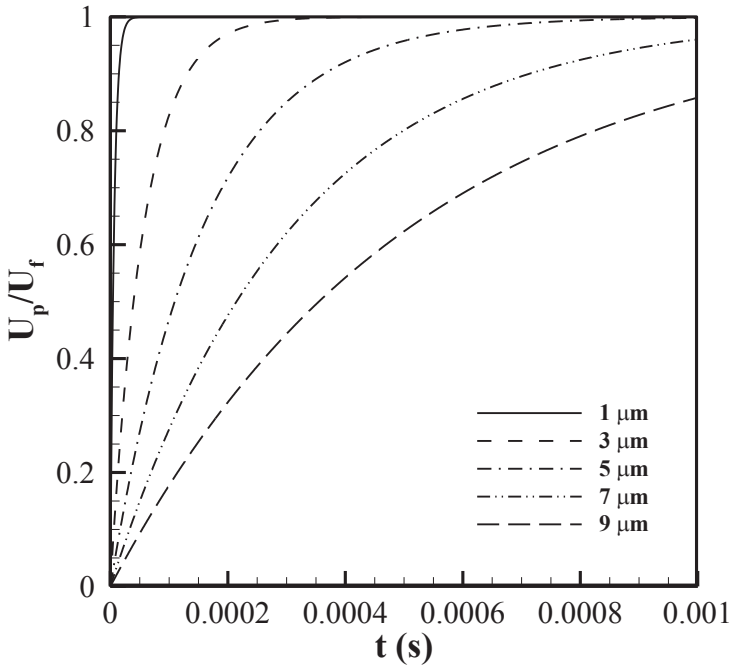

Figure 3.3: Response time of particle velocity

Olive oil was chosen to generate seeding particles in the present study. They were produced by an aerosol generator using Laskin nozzles. The mean diameter of the particles was 1 μm. Excellent velocity tracing characteristics were obtained. There are three Laskin nozzles inside the generator container, and each has 2, 4 or 8 tiny holes at the end, respectively. Control of particle density was effected by combining different nozzles. Air supply is taken from the upstream of the pressure regulator in secondary stream path and goes through a pressure regulator before the inlet of the nozzles. The nozzles are immersed in olive oil, and the pressurised air ejects into the oil from the tiny holes at sonic speed, which creates air bubbles in the surrounding oil liquid. Meanwhile, the shear stress transforms the liquid to particles. The bubbles enclose and carry the particles moving upwards. An impact plate is mounted above the liquid leaving a small gap to the container inner wall. It prevents large particles but allows small particles to get through and enter the wind tunnel system. The inlet and outlet pressure are monitored by two gauges. Raffel et al. (2002) suggested that a preferred pressure difference between the inlet and the outlet is between 0.5 and 1.5 bar. The seeding flows join the main and secondary streams through two adjustable gate valves, which fine-tune the seeding particle allocation between the mainstream and the secondary stream for uniform particle dispersion in the flow field.

The present study employed time-averaged 2D2C and 2D3C PIV measurements and double-frame single exposure recording techniques. For 2D3C measurements, two charge-coupled device (CCD) cameras were required. Each camera features 1344 × 1024 pixel resolution and 12-bit dynamic range for grey-scale image

recording. The pixel size is 6.45 μm, which gives a sensing area of 8.669 × 6.605 mm. Each camera is equipped with a 35 mm film format macro lens, which has a focal length of 60 mm and maximum f/2.8 aperture capacity. Since the CCD sensing area is quite small compared to image field of the 35 mm format, the chip covers only a small portion in the centre of the lens image field. Thus, image aberration, usually severe when away from the centre, could be avoided. The illumination source is a double pulse Nd:YAG laser, with a maximum repetition rate of 15 Hz and a 532 nm green laser beam. The beam is transformed into a light sheet by an external lens attached to the laser head. The thickness of this sheet can be adjusted through a lever on the lens.

The laser and the cameras are mounted on a movable test platform with four degrees of freedom. In the present study, the platform was limited to two movement directions, as shown in Figure 3.4. The vertical position of laser and cameras can be adjusted through a screw bar and guide system. The streamwise movement is achieved through a slide guide. A synchroniser connects the cameras and the laser to a workstation where measurement data are stored and processed. The workstation also commands the synchroniser to trigger laser pulse and camera snap. The minimal achievable time interval between two frames is 0.2 ms. The commercial software package FlowManager by Dantec is run on the workstation to execute measurements and data process.

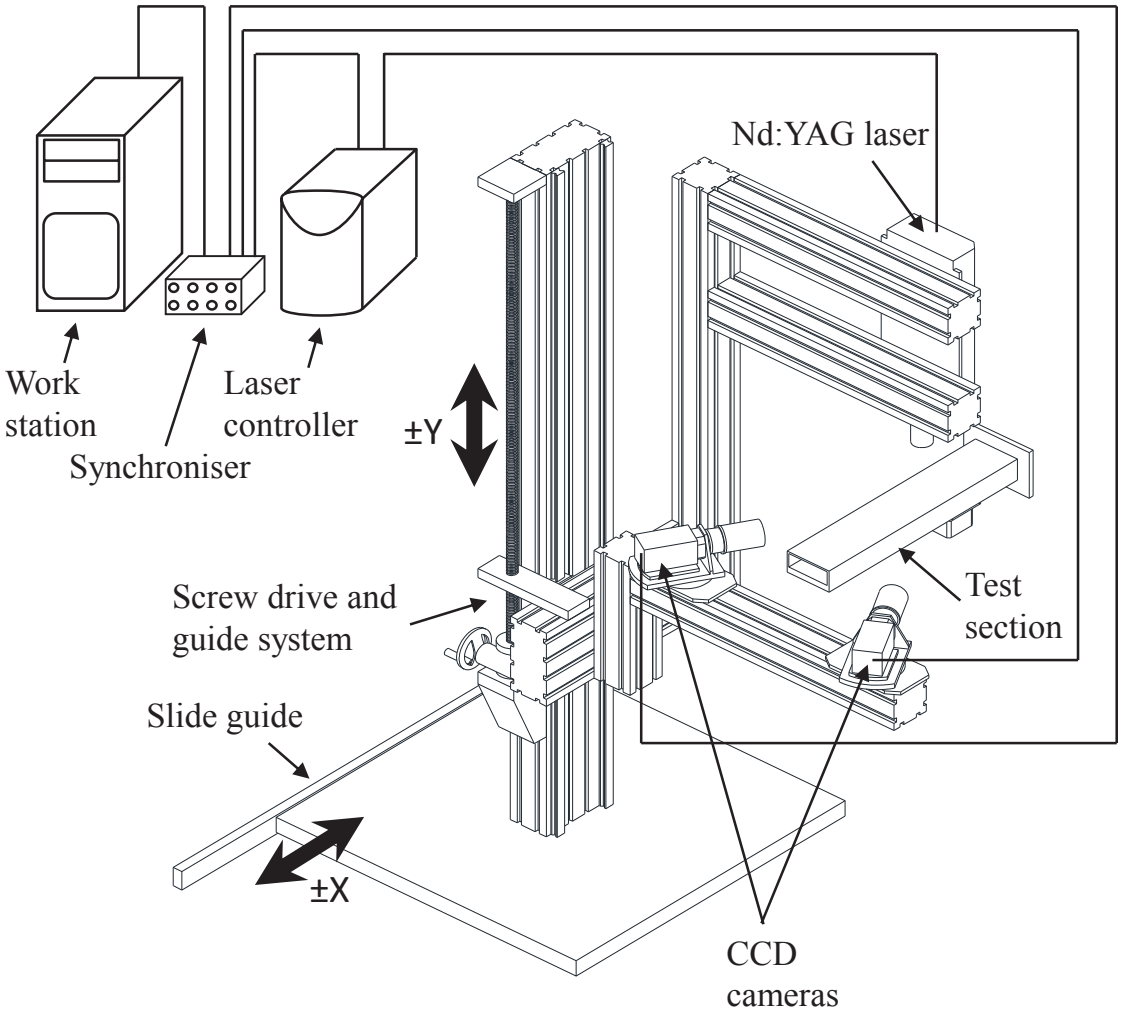

Figure 3.4: Stereo PIV facility

3.3 Measurement Procedures

In PIV measurement, the laser has very high energy intensity during operation. Strong reflection from the test section wall would cause brightened-out pixels in image, and no velocity information would be obtained. Usually reflection happens on the surface of the test section, where the boundary layer velocity information is highly important. Therefore reducing the reflection of laser sheet is one of the most important aspects of PIV measurement. Before conducting PIV measurements, the flat plate surface and hole module top surface were painted with black ink in order to minimise the reflection of laser sheet. In addition, the side walls and top plate of the test section were carefully cleaned for better optical access.

Live preview images were taken to monitor seeding particle density and allocation while adjusting the flow rate of the secondary stream. The procedure continued until the required blowing ratio was obtained and the preview image showed appropriate particle density in both streams. The particle density used in the present study is approximately 15 to 20 particles per 32 × 32 pixel interrogation window.

3.3.1 Camera and Laser Setup

In 2D3C PIV measurements, the two cameras were arranged at either side of the test section. A Scheimpflug configuration was applied to ensure clear sight of the object plane, and the camera body axis was deflected from the lens axis. The tilt angle α for the body could be calculated from the following equation

$$\alpha = arctan\left(\frac{f \cdot tan(\theta)}{D_0 - f}\right)$$

where f is the lens focal length, θ is the angle between lens centreline and test section centre plane and D_0 is the distance between lens optical centre and target plane.

Since a 32 × 32 pixel interrogation window would be used, the required light sheet thickness for 2D3C measurement was calculated using the following equation

$$t = 2a \cdot p/F$$

where a is the dimension of the interrogation window, p is the pitch between CCD pixels and F is the magnification factor. In the present setup, the required thickness of the light sheet was approximately 2.1 mm. Particles illuminated by the laser sheet were extremely bright, so an insufficient depth of field (DOF) would cause a tremendous amount of noise due to the blurred bright particles outside of the DOF. Generally, contrasting aperture diameter gives larger DOF, but a drawback is reduced light through the lens. In the present study, the aperture was adjusted to $f/5.6$ in most cases, which gave a good balance of enough DOF to cover the laser sheet thickness and enough light through the lens. The camera arrangement parameters used in the present study are listed in Table 3.1.

Table 3.1: Camera arrangement parameters

	Phase 1, *yz*-plane	Phase 2, *yz*-plane	Phase 2, *xy*-plane
θ (deg)	30	40	30
α (deg)	5	9	6
D_0 (mm)	450	380	390
f number	$f/5.6$	$f/5.6$	L: $f/4$; R: $f/5.6$
F	$\sim 1/4.6$	$\sim 1/4.2$	$\sim 1/4.2$
Average DOF (mm)	~ 6	~ 4	~ 4

3.3.2 Image Calibration

The calibration of cameras in 2D3C measurements in the first phase of the investigation was done with a calibration target from the instrument manufacturer, featuring a 10 x 8 dot array distributed in two layers. The upper layer is literally the surface of the target and the lower layer consists of concave holes. The target was put in the test section at a potential measurement location to have exactly the same optical environment. The edge of one concave hole was aligned with the plate surface so as to identity the *y*-coordinate of injection hole exit. Each camera took one image of the calibration target, as shown in Figure 3.5. The bigger dot in the centre would be recognised as the origin of coordinate system. The distance between the two neighbouring dots is 10 mm, and the radius of the holes is 5 mm. Thus, the plate surface position would be -15 mm from the origin. The double layer feature was used to identify the origin and calibrate the scale along the *z*-axis.

The dots array was extracted as a warped grid as shown in the figure. The red crosses represent the origin of the coordinate system. As described before, the image aberration at image field centre of the macro lens is fairly small. Neglecting the effect of aberration, direct linear transformation (DLT) was employed to calibrate the images. DLT is directly developed from the optical relation of object and image, assuming zero image aberration. Due to the limitation of calibration target size, a small dot count was covered in calibration images. Imaging model fit parameters were adjusted in accordance with dot count and are listed in Table 3.2.

The calibration established a local magnification factor map and orientation parameters for each camera. The 2D3C measurement results covered an area of 59 × 41 mm, effectively observing most of the mainstream bulk, the boundary layer of mainstream and the interaction between the two flows. 2D2C measurements had similar calibration procedures and covered an area of 70 × 48 mm.

In order to acquire better calibration, a printing-based calibration target was developed and employed in the second phase of investigations to solve the problem of having small number of dots as described in the last section. A dot array patter with smaller pitch 2.5 mm was printed precisely and fixed to the original target. Since the printed target does not have a depth feature, it had to be snapped by the cameras at different locations along the axis normal to the measurement plane. A positioning tool was made to precisely position the target at the measurement location. Seven target images at different locations $x = -3, -2, -1, 0, +1, +2, +3$ mm were taken for calibration and $x = 0$ was the centre of laser sheet. The small pitch made it possible to have large amount of dots, get a close-up image and

perform third-order polynomial calibration, which can correct the aberration of lens. Table 3.3 lists the imaging model fit parameters for third-order polynomial calibration. The target images at $x = 0$ are shown in Figure 3.6. The plate surface was at $y = -10$ mm.

3.3.3 Data Acquisition

The measurement process began by choosing the time interval and image pair number. The time interval was determined with respect to particle travelling distance and interrogation window dimension, which was taken from the preview step in previous sections. The travelling distance of a single particle was limited to about 1/4 of the interrogation window dimension in order not to lose the trace of it, since the particle might move out of the interrogation window or the laser sheet thickness.

A time-averaged PIV measurement gives the statistical result of velocity maps for a series of instants. Having more samples would provide more objective results. However, due to the limitation of memory capacity of the workstation, only 100 pairs of images were taken for each measurement. The time interval was adjusted to 5 ms, which is fairly small and might cause some flaws in the synchronisation between the laser and the cameras. Manual filtration would be necessary in order to remove the un-synced image pairs. As a result, 80 to 100 image pairs would finally be sent for processing.

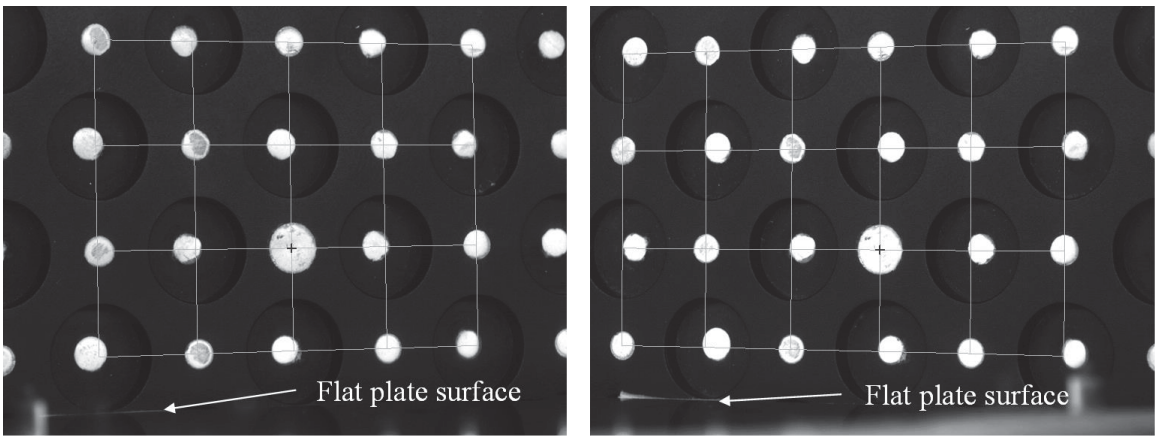

Left camera view Right camera view

Figure 3.5: Grid extracted from the calibration target

Table 3.2: Imaging model fit parameters for DLT calibration

Border	0
Dot area tolerance	1.5
Zero/axis ratio tolerance	0.5
Dot position tolerance	0.2
Minimum dot area	21
Minimum dot count	9

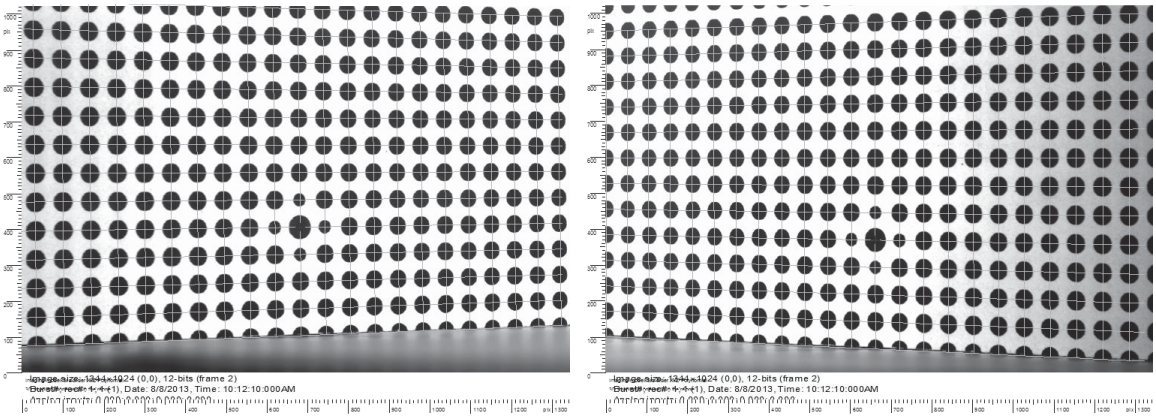

Figure 3.6: Third order polynomial calibration at *x=0*

Table 3.3: Imaging model fit parameters for calibration

Border	0
Dot area tolerance	1.5
Zero/axis ratio tolerance	0.5
Dot position tolerance	0.05
Minimum dot area	21
Minimum dot count	25

3.4 Image Data Process and Post-process

The adaptive correlation method is able to track the particles moving out of the interrogation window of interest by applying an offset to the window. Tracking the out-of-window particles allows more matched particles between the two frames, and consequently a higher signal-to-noise ratio can be gained. The offset value is based on the vector obtained from an initial interrogation window that is larger than the final interrogation window. Details of this technique can be found in Westerweel et al. (1997). The present experiments used a 32 × 32 pixel final interrogation window and a 128 × 128 pixel initial interrogation window. There was 50% overlap between the two windows.

During the adaptive correlation process, the vector maps were validated by peak validation and moving average validation. The minimum peak height relative to peak 2 was set to 1.2, and the moving average validation in a 3 × 3 neighbourhood used an acceptance factor of 0.1. Figure 3.7 shows the histogram of peak width of a correlated vector map. Most peaks are distributed in the recommended optimal range of 3 to 6 pixels.

Each vector map represents the flow field at the instant of recording, which results in a time-averaged vector map of the flow throughout the measurement period. At the same time, possessing instant vector map and time-averaged velocity field can also give turbulence intensity as follows

$$TI = \sqrt{\frac{1}{n}\sum_{i=1}^{n}(U_i - U)^2}$$

where U_i is the instant streamwise velocity at the same location of the time-averaged velocity U.

The vector maps contained three velocity components and velocity magnitude for each test condition. The data points were discrete in all three directions. Kriging interpolation was used to generate volumetric flow field data. The technique uses the assumption that the unknown data at a certain point is the average of the neighbouring points weighted by their distance to the unknown point. Details about the Kriging algorithm can be found in Dai et al. (2003). The present investigation has fewer known data points in *x*-direction than in the other two, since the data were acquired using a "tomoscan" technique. Although it was found that the direction of CRVP is not perfectly aligned with the *x*-axis, the *x*-component of the vorticity is the most important and representative in the flow field. The focus in the present study is more on the gradients in *y*- and *z*-direction. The variation along the *x*-axis could be used as a good visualisation of the flow structure. During the post-process, the length scale of flow field data was non-dimensionalised by injection hole diameter, and the velocity components were non-dimensionalised by the mean velocity of mainstream.

3.5 Experimental Uncertainties

The main uncertainties in the experiments existed in the flow rate of each stream and the measurement error of PIV. The mainstream flow rate has an uncertainty from +2% to -5% and it is ±3% for the secondary stream. The PIV measurement quality was monitored through the pixel histogram of particle images and accuracy

verification case of mainstream velocity profile. The experimental velocity profile result at test section centre plane was compared to a theoretical velocity profile according to the $1/7^{th}$ power law. In Figure 3.8, the experimental results show some deviation from the theoretical profile around the half height of the test section due to the fact that the $1/7^{th}$ power law profile provides an exponential approximation to external turbulent flow over a plate. The experimental results were for an internal turbulent flow with a symmetric velocity profile. Measurement error was estimated by unit-length flow rate acquired by integrating the velocity profile. Directly integrating the velocity field of a cross-sectional plane for area flow rate was not applicable since PIV measurement does not cover the entire cross-sectional plane. The results suggest that 2D3C PIV measurement has an error of 2% and 2D2C has 5%.

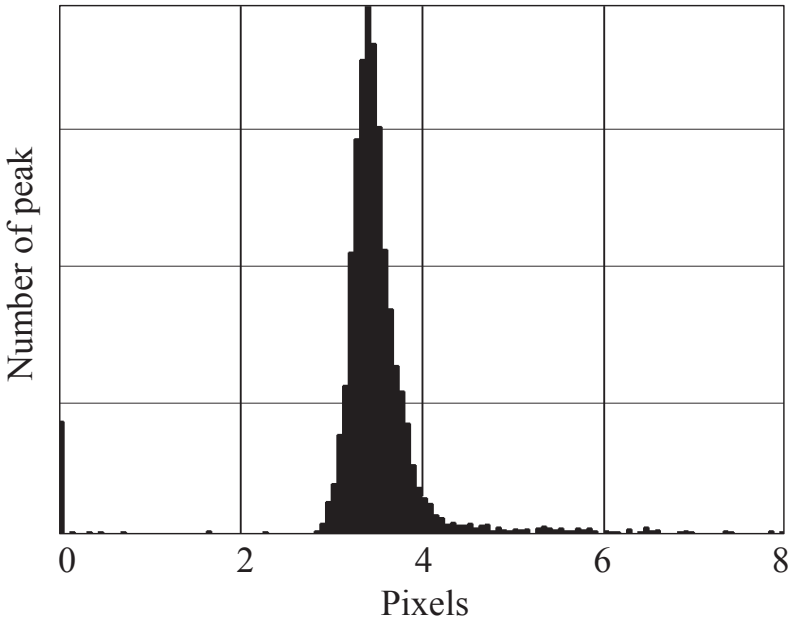

Figure 3.7: Histogram of peak width

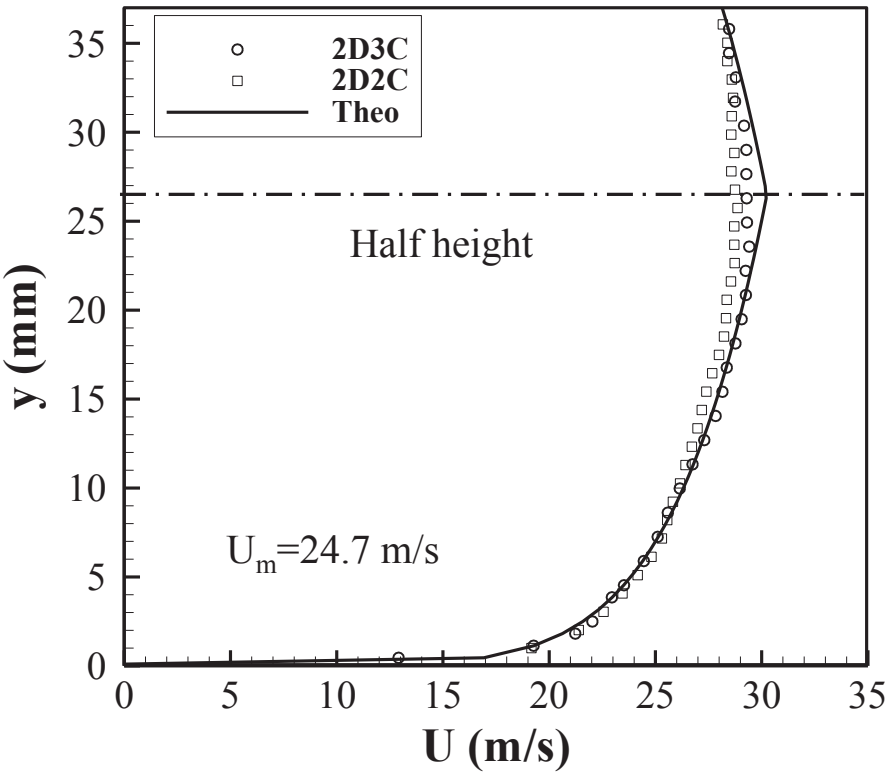

Figure 3.8: Mainstream velocity profile for measurement accuracy verification

3.6 Flow Field Evaluation

In the present study, the flow field analysis is focused on velocity distribution and vortex structure. The velocity fields are obtained through experimental measurements. Upon the acquisition of velocity fields, the velocity gradient in all directions at each location can be computed. These gradients are the basic elements required to perform evaluations on many other fluid dynamical characteristics, such as strain rate, vorticity and Q value. In the present study, the gradients at each location of the flow field are computed from the velocity fields based on a first-order central difference scheme, which incorporates only directly neighbouring data points to calculate the derivative.

3.6.1 Vorticity

Vorticity is by definition the circulation of a unit area in a flow and could be expressed as

$$\omega = \frac{d\Gamma}{ds}$$

where Γ is the circulation of the flow, which is the line integral of velocity along a closed curve, and by Stokes' theorem

$$\Gamma = \oint_C \vec{U} dl = \iint_S \omega ds$$

It should be noted that the equation is only valid when closed curve C is not only a closed curve, but also the boundary of the surface S.

Mathematically, vorticity could be written as the cross product of the Nabla vector and the velocity vector as

$$\omega = \nabla \times \vec{U}$$

where $\nabla = (\frac{\partial}{\partial x}, \frac{\partial}{\partial y}, \frac{\partial}{\partial z})$

The x-component of vorticity is of more interest in the present study. It could be expressed as

$$\omega_x = \frac{\partial w}{\partial y} - \frac{\partial v}{\partial z}$$

The vorticity was non-dimensionalised by the mainstream velocity U_m and the injection hole diameter d as

$$\omega^* = \frac{\omega}{U_m/d}$$

3.6.2 Q-Criterion

Due to the existence of large shear strain, the calculated vorticity may not represent a vortex objectively. The Q-criterion was employed to assist with vortex field identification, whose value could be determined by the following equation by Haller (2005).

$$Q = \frac{1}{2}(|\Omega|^2 - |S|^2)$$

where Ω is the vorticity tensor $(\partial w/\partial y - \partial v/\partial z)/2$, and S is the strain rate tensor $(\partial w/\partial y + \partial v/\partial z)/2$. A positive Q value indicates a vortical region where rotation prevails instead of shear.

An example of a vorticity not representing a vortex is that in a 2d laminar boundary layer over a flat plate, the shear in wall-normal direction becomes the only non-zero part in the equation of calculating the vorticity. Apparently there exists vorticity in the flow field, but the boundary layer in fact does not contain a vortex.

Chapter 4

Flow Field Downstream of Nozzle Hole

4.1 Introduction

As a new film cooling hole geometry is proposed, it is highly important to have detailed knowledge, such as the velocity distribution and the vorticity distribution, of the flow field downstream of the injection, because the jet flow structure and CRVP are directly responsible for the film cooling performance. Exposing and understanding the phenomena and features in the flow fields is a key step in studying the effects of using an orifice for film cooling. Many features in the film cooling effectiveness map and heat transfer coefficient map can be explained by the flow field characteristics. This chapter is focused on establishing a structural view of the flow field downstream of the nozzle hole at both low and high blowing ratios. The velocity fields and vorticity fields of the nozzle hole and cylindrical hole are presented and compared at several downstream locations. The CRVP suppressing effect of the nozzle hole and the benefits brought about by the reduced CRVP strength are also demonstrated.

4.2 Test Module

The test section of the wind tunnel has the ability to change hole geometry easily using various test modules. The nozzle hole geometry was designed using a basic type test module, to which the hole geometry is integrated as a fixed feature of the module. The test module is mounted to the bottom of the wind tunnel section along with the plenum module. Figure 4.1 presents the geometry of the nozzle hole, which is the original design by Li et al. (2011). The flow field and cooling effectiveness of this design were investigated numerically by the authors. Nozzle hole is a cylinder-based cooling hole, which means the entrance and exit of the cooling hole are both circular-shaped and of the same diameter. The hole length is 1.75d and the injection angle is 35°. No compound angle was included in the present study. Based on the cylindrical hole, a slot type orifice is placed before the hole exit. The orifice is configured perpendicularly to the axis of hole and located 0.3d from the leading edge of the hole exit. The two plates at both lateral sides of the wall form a channel opening of 0.5d. The thickness of the orifice plates is 0.07d and half thickness 0.035d is added to both sides of the plate plane used for positioning. Three nozzle holes are arranged on the test module with an interval of 3d as shown in Figure 4.1 b. The trailing edge of the hole exit is 3mm away from the module edge. During the experiments, only the centre hole was used and the two side holes were closed, since this study focuses on a more fundamental view of the flow field of one hole injection. The origin of the coordinate system is at the trailing edge of the hole exit. This coordinate system configuration is used throughout the present thesis. The test

module was fabricated using 3D printing technology, which is important in forming the orifice plates. The material of the test module is a sort of semi-transparent plastic. The top surface of the test module was painted with a black ink, often used in experiments involving thermochromic liquid crystal temperature measurement. The purpose of painting is to reduce the reflection of strong laser sheet during measurement. The black ink was found highly important and effective in tackling with the reflection.

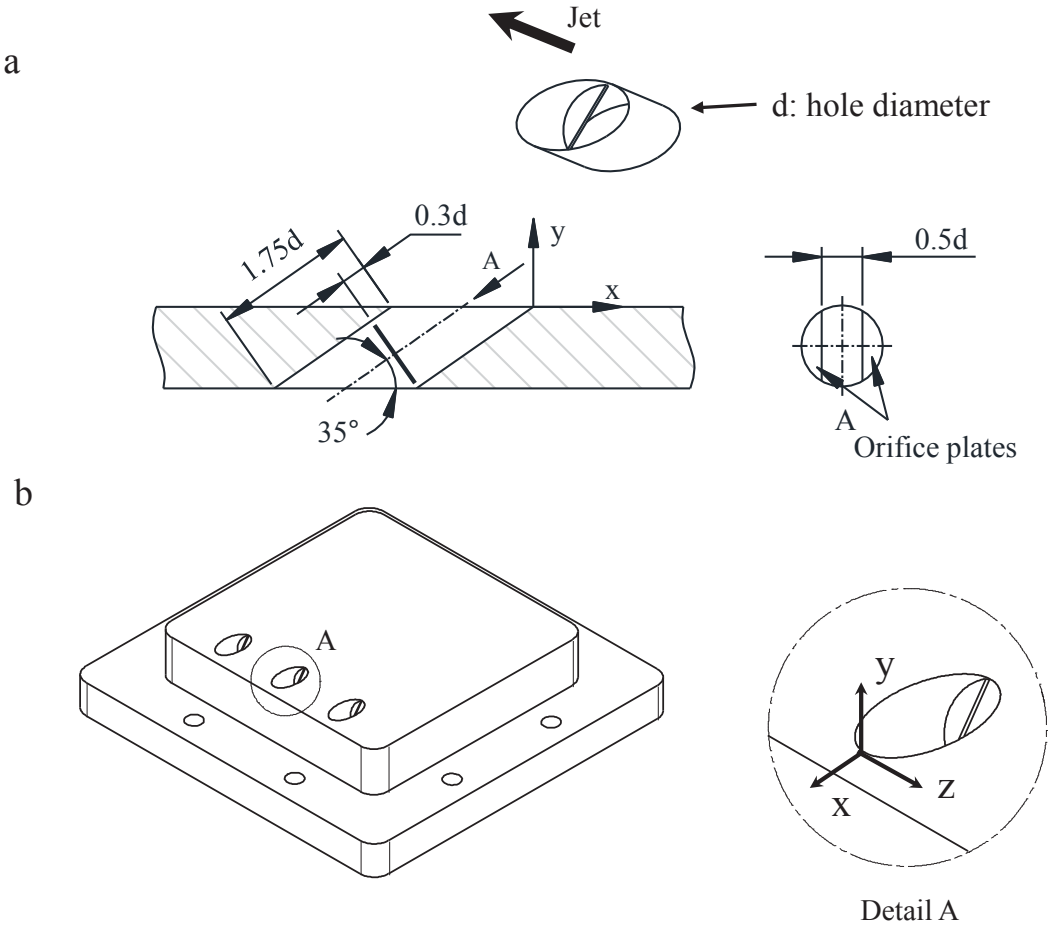

Figure 4.1: Nozzle hole geometry, a) Conceptual sketch, b) Test module

4.3 Test Matrix for Flow Field Structure Study

In the first phase of the study, the jet structure in the flow field downstream of the nozzle hole was investigated and compared with cylindrical injection across blowing ratios of 0.5 to 2.0, which are commonly used in both the literature and actual applications. The experiments were conducted under four blowing ratios in this range. The lowest blowing ratio is $BR = 0.5$, considered a typical low blowing ratio injection. Higher ratios of 1.0, 1.5 and 2.0 are categorised as high. Jet penetration characteristics is deemed the major criterion determining the categorisation, since low blowing ratio injection features jet flow attached to the surface and on the hand jet lift-off occurs at high blowing radio. The density ratio of the jet and the mainstream was approximately 1.0.

Table 4.1: Phase 1 test matrix

Case	Description	BR	DR	d (mm)	Q_2 (SCFM)	P_2 (psi)	T_2 (°C)
CYL-05	Cylindrical	0.5	1.0	7	1.01	0.2	21
CYL-10	Cylindrical	1.0		7	2.1	0.5	
CYL-15	Cylindrical	1.5		7	2.97	0.9	
CYL-20	Cylindrical	2.0		7	4	1.5	
NOZ-05	Nozzle	0.5		6.4	0.83	0.2	
NOZ-10	Nozzle	1.0		6.4	1.7	0.4	
NOZ-15	Nozzle	1.5		6.4	2.4	0.9	
NOZ-20	Nozzle	2.0		6.4	3.2	1.5	

The test matrix of nozzle hole and cylindrical hole with various blowing ratios is summarised in Table 4.1. It should be clarified that in this phase of study, the nozzle hole diameter was 6.4 mm, while the cylindrical hole had a diameter of 7mm. The dimension deviation is due to manufacturing flaws in 3d printing the nozzle hole. During the experiments, the secondary stream flow rate was adjusted according to each hole diameter. The difference in diameter was later eliminated by non-dimensionalising.

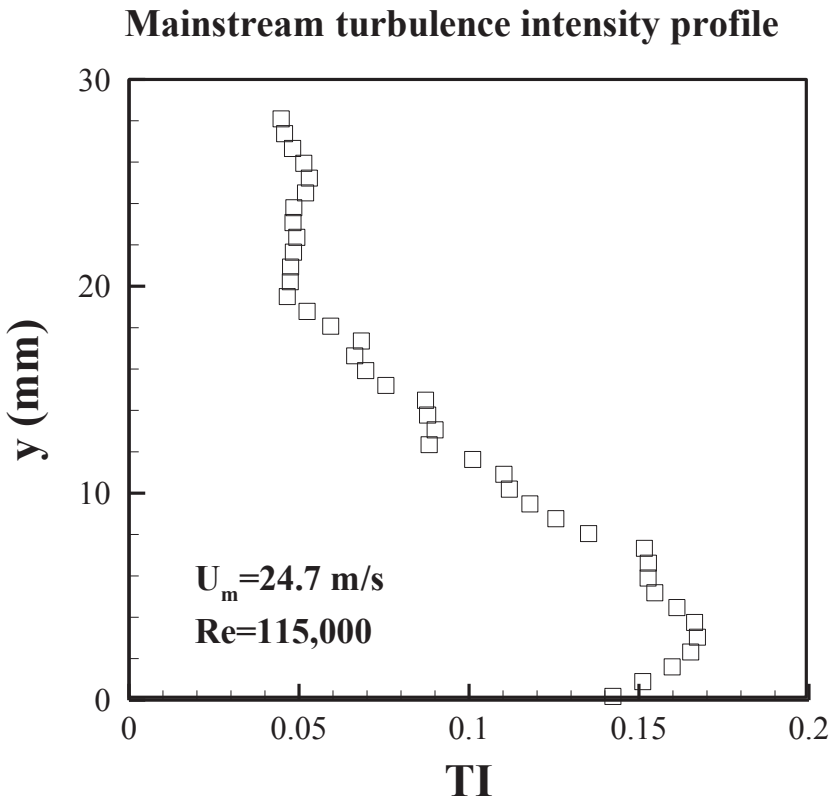

Figure 4.2: Mainstream turbulence intensity of U_m=24.7 m/s, Re=115,000

In all the experiments, the variation in blowing ratio was achieved only by altering the secondary stream flow rate. The mainstream was kept at a constant condition. Table 4.2 summarises the test conditions of the mainstream in this phase. The volumetric flow rate of the mainstream at the digital flow meter was 275 CFM. The static pressure of the mainstream was 0.19 psi and the static temperature was 21 °C. Therefore the mass flow rate of the mainstream was 0.1578 kg/s, providing a mainstream mean velocity of 24.7 m/s in the test section. The Reynolds number of the mainstream was 111,500, based on the hydraulic diameter of the test section. The mainstream had a fully developed turbulent flow after the 1.6 m long entrance section. The area-averaged turbulence intensity of the mainstream was 10%. Figure 4.2 shows the mainstream turbulence intensity profile.

Table 4.2: Phase 1 mainstream conditions

Q_1	275 CFM
P_1	0.19 psi
T_1	21 °C
$\dot{m}_m$	0.1578 kg/s
U_m	24.7 m/s
ρ_m	1.217 kg/m3
Re_m	115,000
Ma	0.07
$\overline{TI}_m$	10%

4.4 Downstream Vorticity Variation

To get a first glance at the anti-CRVP effect of the nozzle hole, the major component of CRVP vorticity, the streamwise vorticity, was recorded and compared quantitatively. The magnitudes of streamwise vorticity at different downstream locations are presented in Figure 4.3. The values in the figure represent the average value of the magnitude of both positive and negative peak vorticity at corresponding locations. Zaman et al. (2010) used a similar method to describe the variation of downstream vorticity in their study, which provided a direct perspective of the downstream vorticity variation. For the multi-core vortices to be introduced in later sections of the present study, the peak vorticity measures the highest value among the cores. It is apparent that the streamwise vorticity gets more and more intense with the increase of blowing ratio. For cylindrical injection, the streamwise vorticity magnitude immediately after injection at $BR = 2.0$ is almost four times higher than that at $BR = 0.5$.

It can be seen in all the cases in Figure 4.3 that the nozzle jet shows much less streamwise vorticity at most of the downstream locations in comparison with the cylindrical jet, despite the fact that the reduction in vorticity is limited immediately after the injection at all blowing ratios. Based on the vorticity variation, the average vorticity reduction in the measured range of $x/d = 0$ to 10 was obtained at all blowing ratios. The greatest decrease appears at a low blowing ratio 0.5, which averages an ω_x^* decrease of 55%. The average drop is 38%, 40% and 34% for a blowing ratio of 1.0, 1.5 and 2.0, respectively.

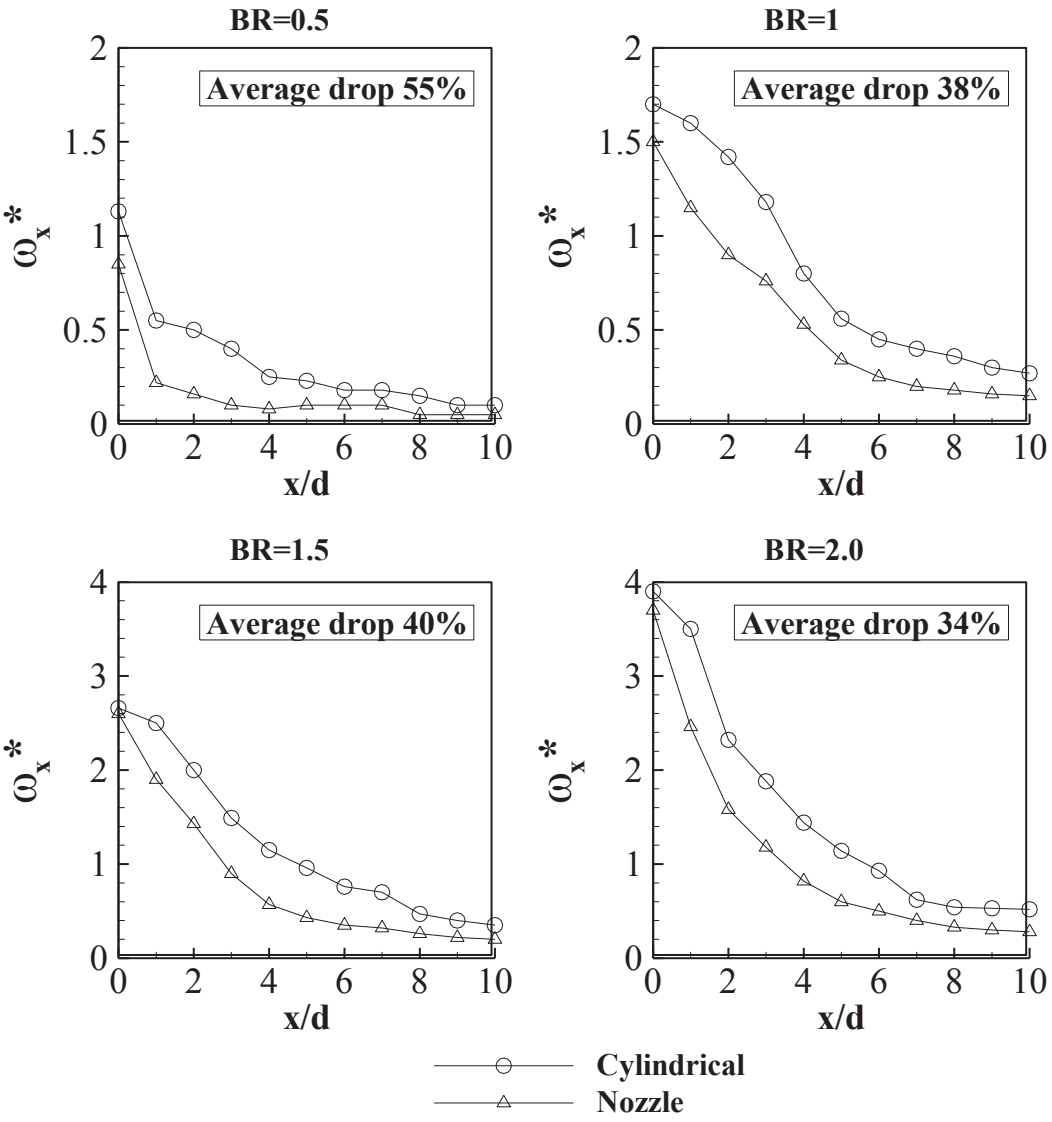

Figure 4.3: Streamwise vorticity peak variation

4.5 Flow Field at Low Blowing Ratio

4.5.1 Velocity fields

At a low blowing ratio of 0.5, both the cylindrical jet and nozzle jet are attached to the surface while evolving. Figure 4.4 shows the streamwise velocity contours and

the V and W vectors of both hole schemes at $x/d = 0$ and $x/d = 2$. Due to the squeezing effect of the orifice, the nozzle jet shows a slightly higher penetration immediately after injection, as shown in Figure 4.4 $x/d = 0$. Both jets slow down quickly after injection due to lateral diffusion and low streamwise momentum. At $x/d = 2$ in Figure 4.4, similar velocity contours are observed in both cases. Both cases show vaulted jet bulk fully attached to the surface. The streamwise velocity at the centre of the jet bulk is greatly lower than mainstream velocity. In the figure, CRVP cannot be clearly observed through the velocity vectors since they are very weak due to low blowing ratio. The plate surface also limits the development of vortices as the jets are attached to the surface.

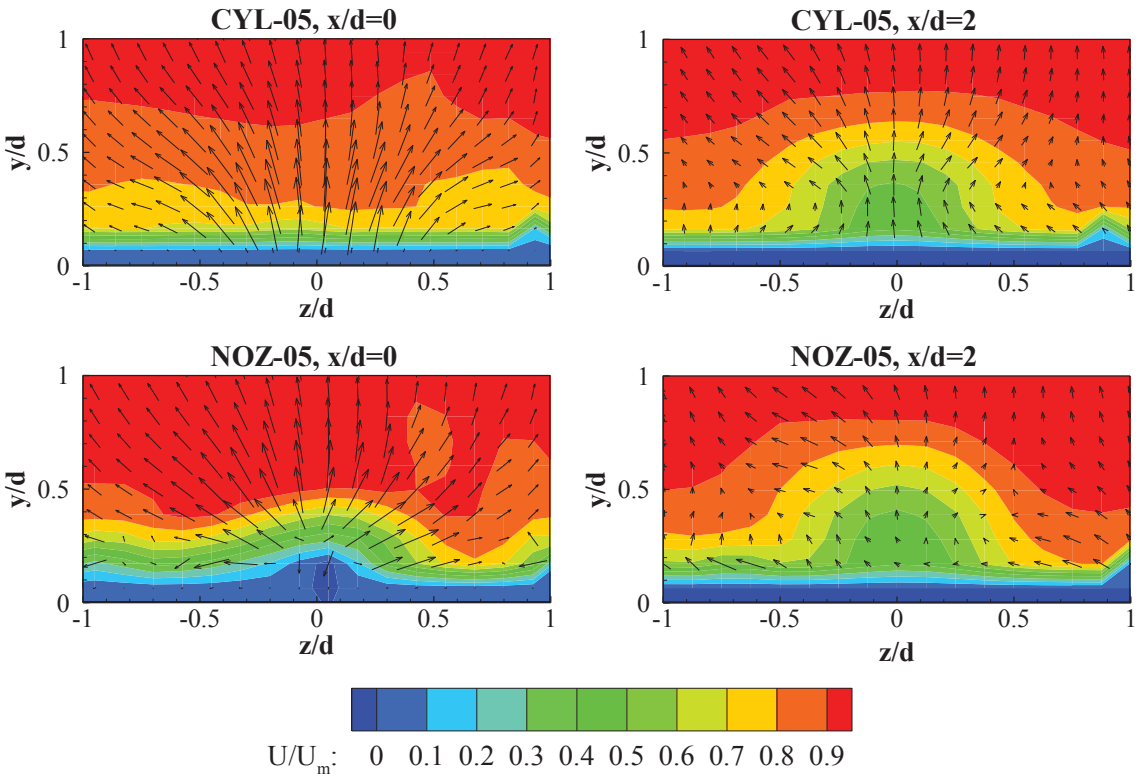

Figure 4.4: Velocity fields of CYL-05 and NOZ-05

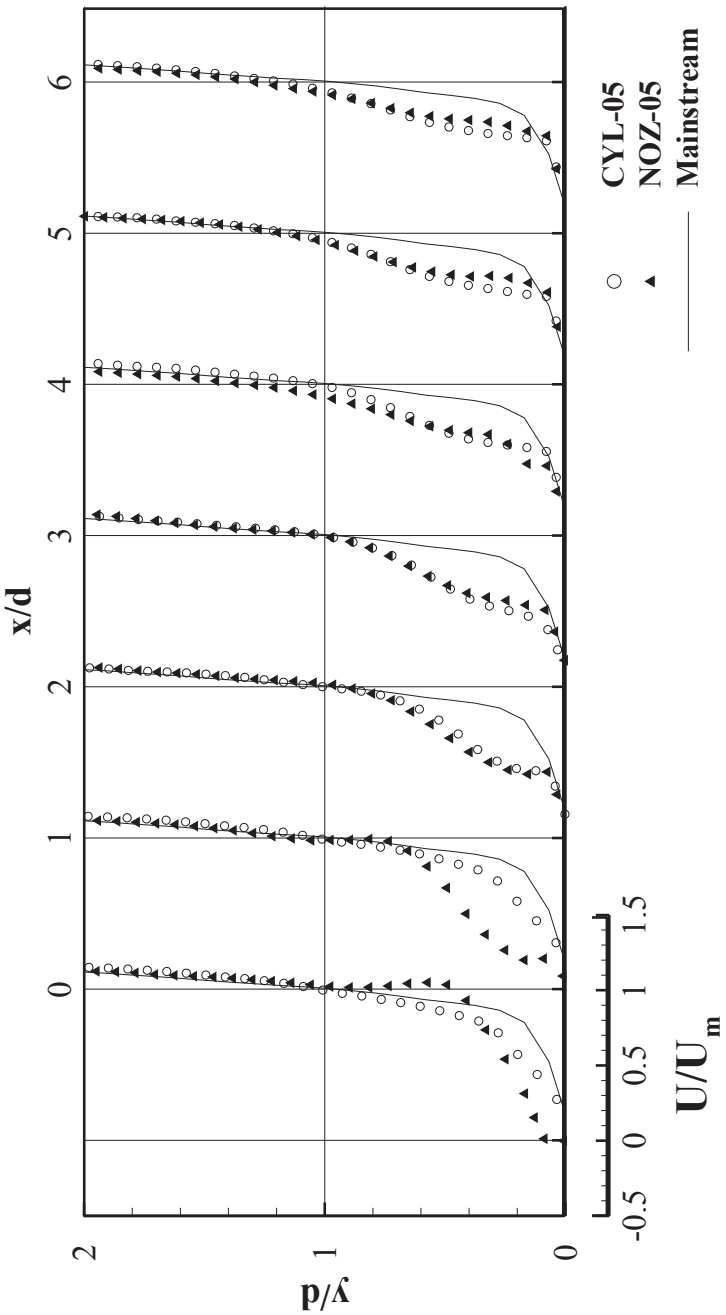

Figure 4.5: Centre plane velocity profiles of CYL-05 and NOZ-05

Figure 4.5 shows the centre plane velocity profiles of CYL-05 and NOZ-05 with the mainstream velocity profile as a reference. Before $x/d = 2$, the nozzle jet shows larger velocity gradient in contrast to the more orderly profile of the cylindrical jet. The velocity peak of the nozzle jet penetrates into a higher position and the near-

surface portion is slower at $x/d = 0$, as in Figure 4.5. A slight reversed flow region can be observed close to the surface. The peak velocity of the nozzle jet slows down as the slow near-surface portion catches up at $x/d = 1$. Due to the low momentum at low blowing ratios, jet diffusion happens more quickly than at high blowing ratios. It can be seen that both cases show similar velocity profiles further downstream due to diffusion and boundary layer shear force. The velocity magnitude of nozzle injection is slightly higher than with cylindrical injection.

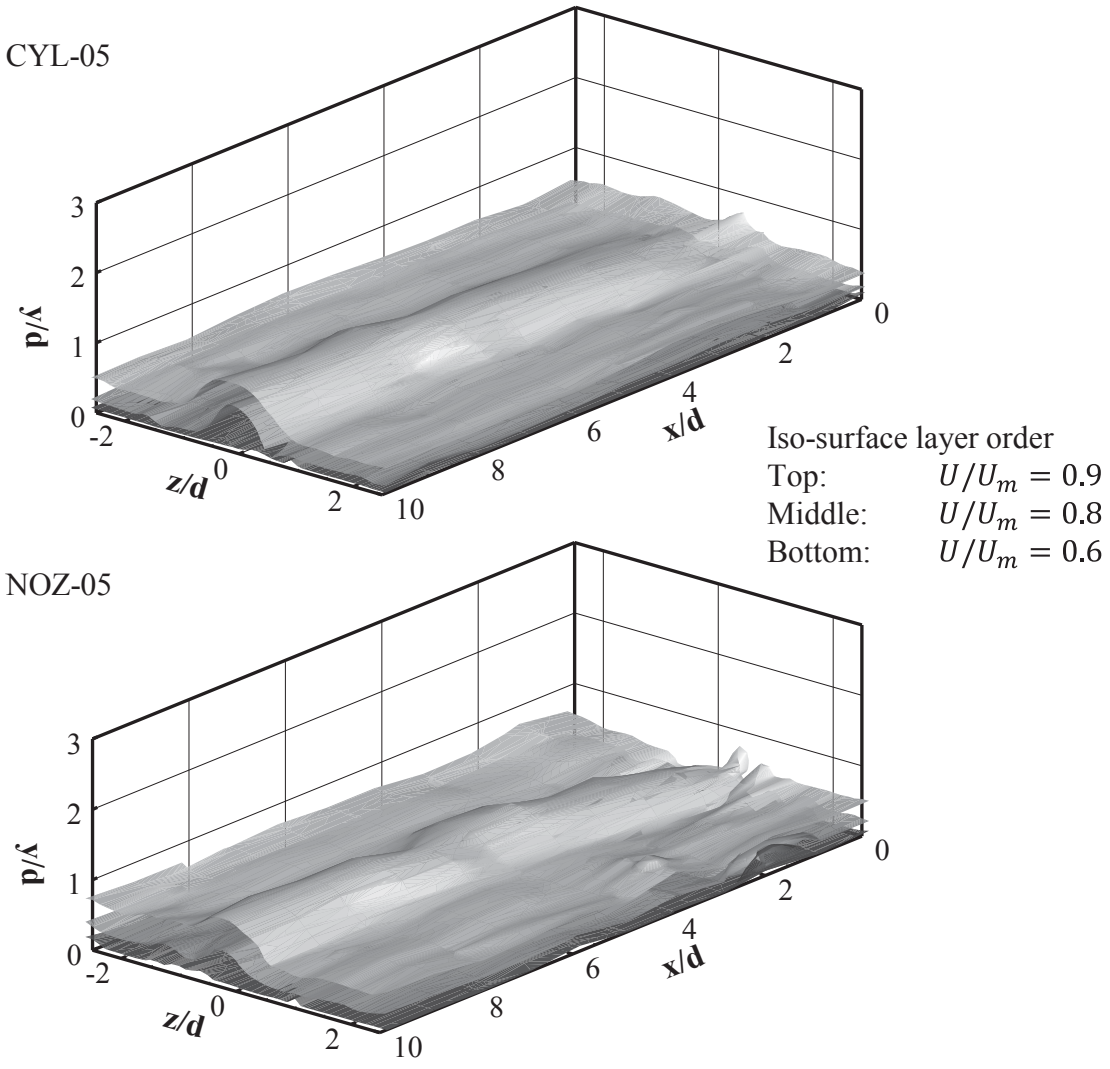

Figure 4.6: Streamwise velocity iso-surfaces of CYL-05 and NOZ-05

It can be seen from the velocity iso-surfaces of both cases presented in Figure 4.6 that the both the cylindrical hole jet and nozzle hole jet gradually form an arch-shaped structure from the plate surface as the result of jet injection. The relatively flat portion at both lateral sides of each iso-surface is the mainstream. The jet flow in the nozzle case shows less uniformity around the injection region in comparison to the cylindrical case, which is attributed to the presence of reversed flow.

4.5.2 Vorticity fields

Although CRVP cannot be visualized directly from the velocity fields and velocity vectors due to the fact that they are actually very weak at low blowing ratios, the vortex structure can still be traced by analysing the vorticity field generated based on velocity field. Figure 4.7 compares the streamwise vorticity field at $x/d = 2$. Solid line circles represent regions of positive Q value, indicating truly vortical flows. Thus, a counter rotating vortex pair can be effectively identified. It can be seen from the Q value lines that the vortical region of the nozzle jet is close to the hole centre $z/d = 0$, because the opening of the orifice is apparently narrower than the cylindrical exit. Some vortices were appearing with respect to the span of the orifice. Despite the fact that the orifice created vortices of the same rotational sense as downstream CRVP in this cross-sectional plane, the strength of those vortices are considerably lower than that of the cylindrical injection, which is essential to cooling performance. In the vorticity field of case NOZ-05, a strong laser reflection created some disturbances at the surface.

Generally, under low blowing ratios, jet attachment of high degree was observed downstream of the two sorts of injection holes. The large velocity gradient in the boundary layer leads to considerable shear force that allows little room for the both jets to show significant structural difference in both streamwise velocity profiles and vortices. Yet as shown in Figure 4.5, the nozzle injection shows slightly higher streamwise velocity in the near surface region, which is attributed to the low jet momentum loss due to weak CRVP.

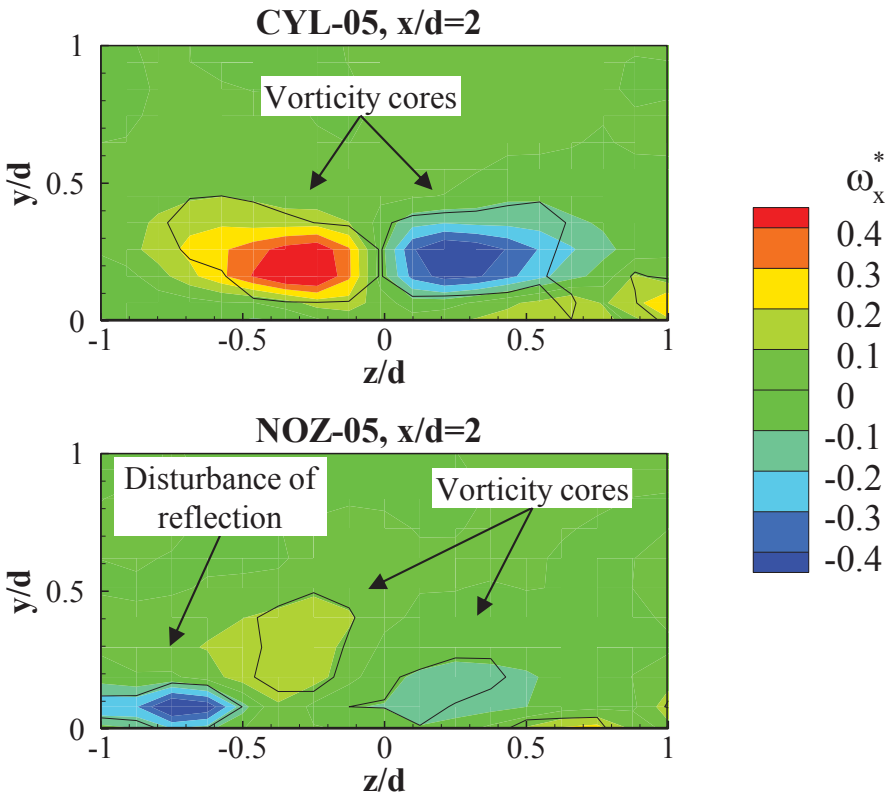

Figure 4.7: Streamwise vorticity field of CYL-05 and NOZ-05 at *x/d*=2

4.6 Flow Fields at High Blowing Ratios

4.6.1 Jet merging in velocity fields

The flow field downstream of the nozzle hole demonstrates very different jet behaviours at blowing ratios of 1, 1.5 and 2. Film cooling jets issued from cylinder based holes lift off from the surface at these blowing ratios. The jets have more freedom to show different manners of evolving when they are away from the wall. This also means more chance for the mainstream to be entrained under the jet. Figure 4.8 presents the streamwise velocity contours and V, W vectors in various *yz*-planes of both hole schemes at a blowing ratio 1.5. The usual kidney-shaped structure of cylindrical injection is clearly observed after $x/d = 2$. A low velocity region exists under the jet due to jet lift-off and mainstream entrainment by the CRVP. Jet lift-off leaves space under it for the mainstream to fill out the region. Moreover, the low speed mainstream decelerates the jet due to the existence of strong shear force when the jet to mainstream velocity ratio is high. The kidney structure remains and increases in size and vertical position as it evolves further downstream. The lateral spreading characteristics of both kinds of injection do not have obvious difference. Despite the fact that the jet downstream of the nozzle hole laterally spreads up to $z/d = \pm 1$ immediately after injection, it does not provide wider spreading further downstream. The wide envelope of the nozzle jet appears due to the fact that there is a reversed flow region in the jet bulk, which pushes the jet fluid outwards.

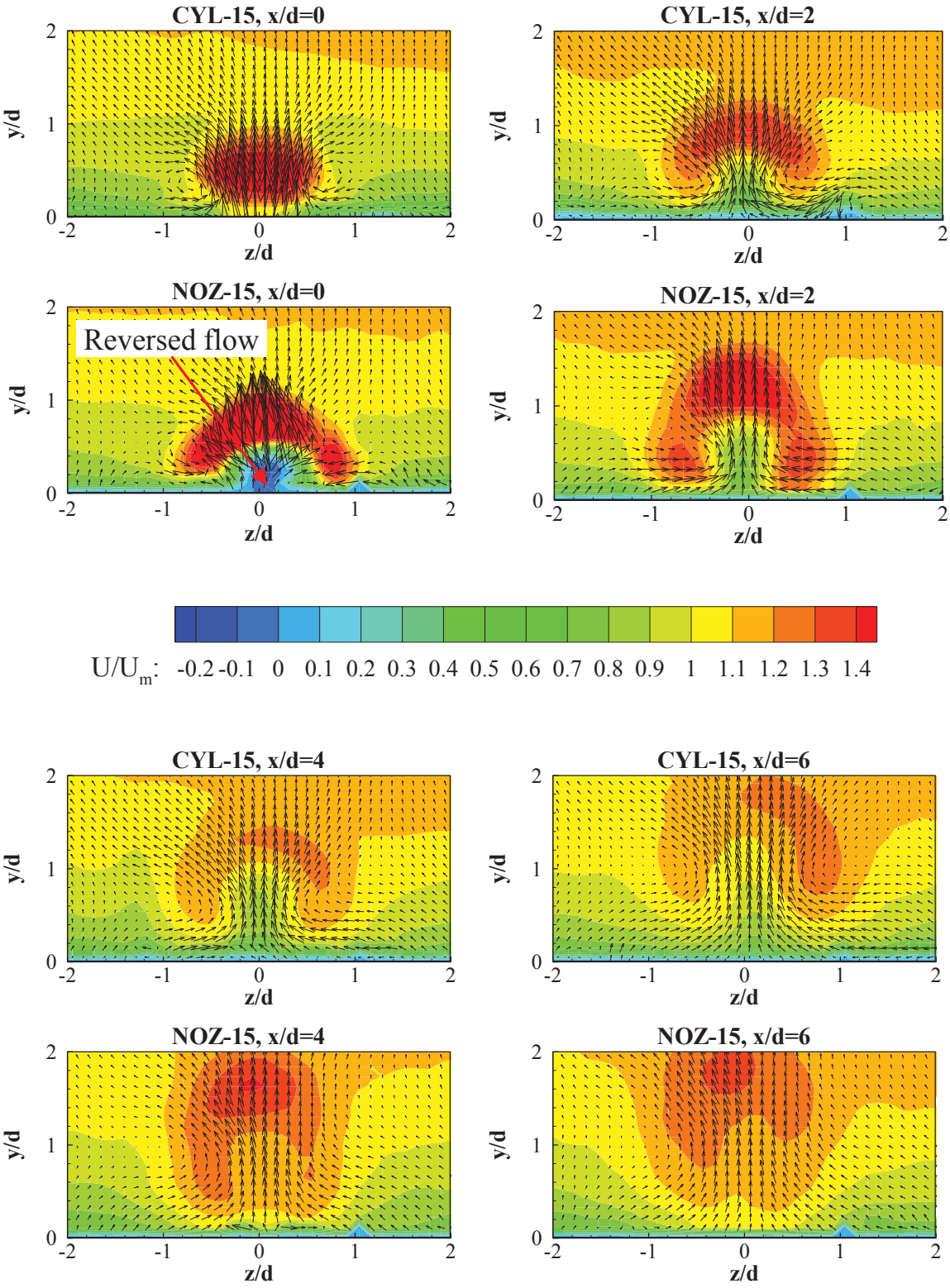

Figure 4.8: Velocity fields of CYL-15 and NOZ-15

On the other hand, nozzle hole injection shows different jet structure throughout the streamwise locations. The nozzle jet laterally spreads more after injection as at $x/d = 0$, forming an umbrella-shaped jet rather than the concentrated cylindrical jet at the same location. Under the umbrella, the flow shows a slightly reversed region. The nozzle jet stretches in height and the umbrella shape breaks into three high velocity regions at x/d =2. Nonetheless, while the kidney-shape cylindrical jet continues and grows in size at $x/d = 4$, the two lower branches of the nozzle jet close to the surface decelerate and start to merge with each other. This merging behaviour fills the low velocity centre region with jet fluid, a phenomenon that continues as a stouter jet bulk appears further downstream. It is clear that the nozzle jet has better coverage over the surface. In contrast, the cylindrical jet has large amount of the mainstream entrained under the kidney shape at $x/d = 4, 6$, as shown in Figure 4.8.

The degree of mainstream entrainment can be observed in the spanwise velocity contours presented in Figure 4.9. It can be seen that there are strong spanwise velocity magnitudes towards the centre in the near-surface region of cylindrical injection. Considering the low compressibility at such a low Mach number, this indicates strong mainstream entrainment by the CRVP. The entrained mainstream fluid from both sides joins and moves upwards at the centre. Due to the amount of entrainment, the jet of cylindrical injection eventually forms the kidney shape as shown at those downstream locations in Figure 4.8. The nozzle injection case shows much weaker spanwise velocity towards the centre, so the amount of entrained mainstream fluids is not able to split the jet.

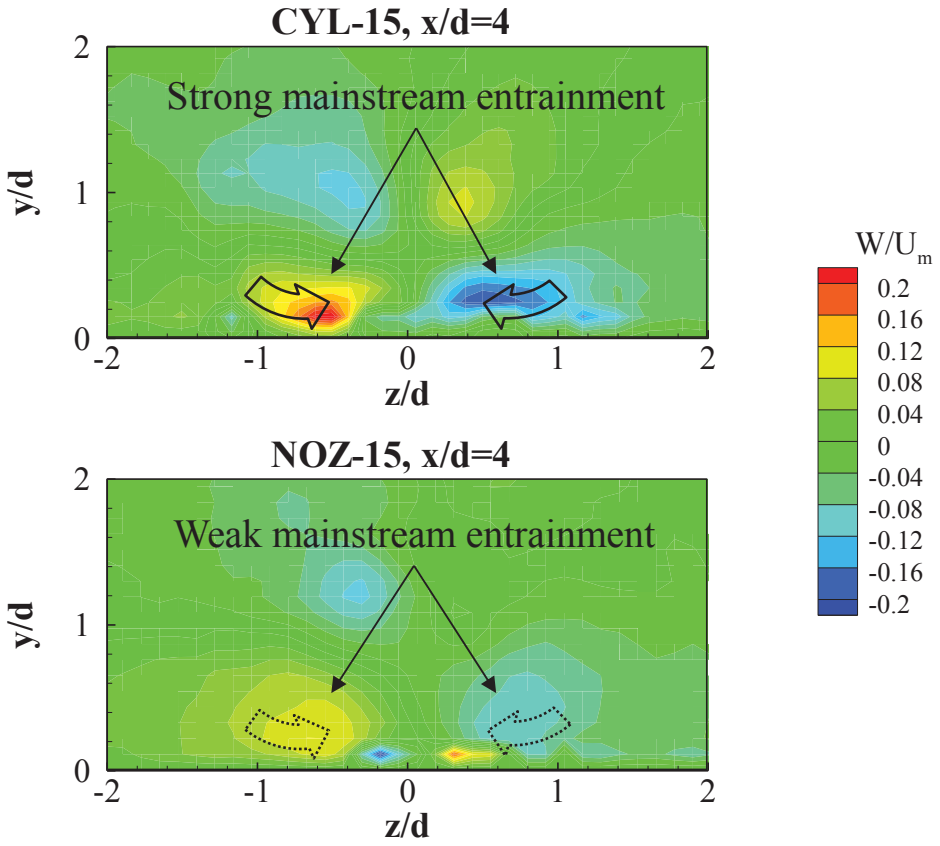

Figure 4.9: Spanwise velocity contour of CYL-15 and NOZ-15

4.6.2 Velocity catch-up

Figure 4.10 shows the streamwise velocity distributions overlaid by streamlines of both cases on the *xy*-plane at $z/d = -0.2$. The streamlines from the injection hole of the CYL-15 case squeeze together downstream at a high position. In contrast, the streamlines of the nozzle hole jet demonstrates less upwash trends, indicating weaker jet lift-off at the centre plane. Faster fluid movement can be observed near the plate surface from $x/d = 2$. The reversed flow region of nozzle injection is zoomed-in in Figure 4.11 along with the result of previous CFD simulation by Li and Hassan (2011). The comparison is made based on a similar momentum flux ratio,

since experimental and CFD cases do not have the same density ratio. The consequent difference in velocity ratio and blowing ratio are neglected herein. It can be seen that experimental and CFD results indicate similar manners of flow, yet there is a difference in velocity distributions in the y-direction. In both experimental and numerical results, the reversed streamlines start from $x/d = 0.5$ and re-join the others after a U-turn. It is conjectured that the reversed flow is caused by the low pressure in a separation region after the orifice.

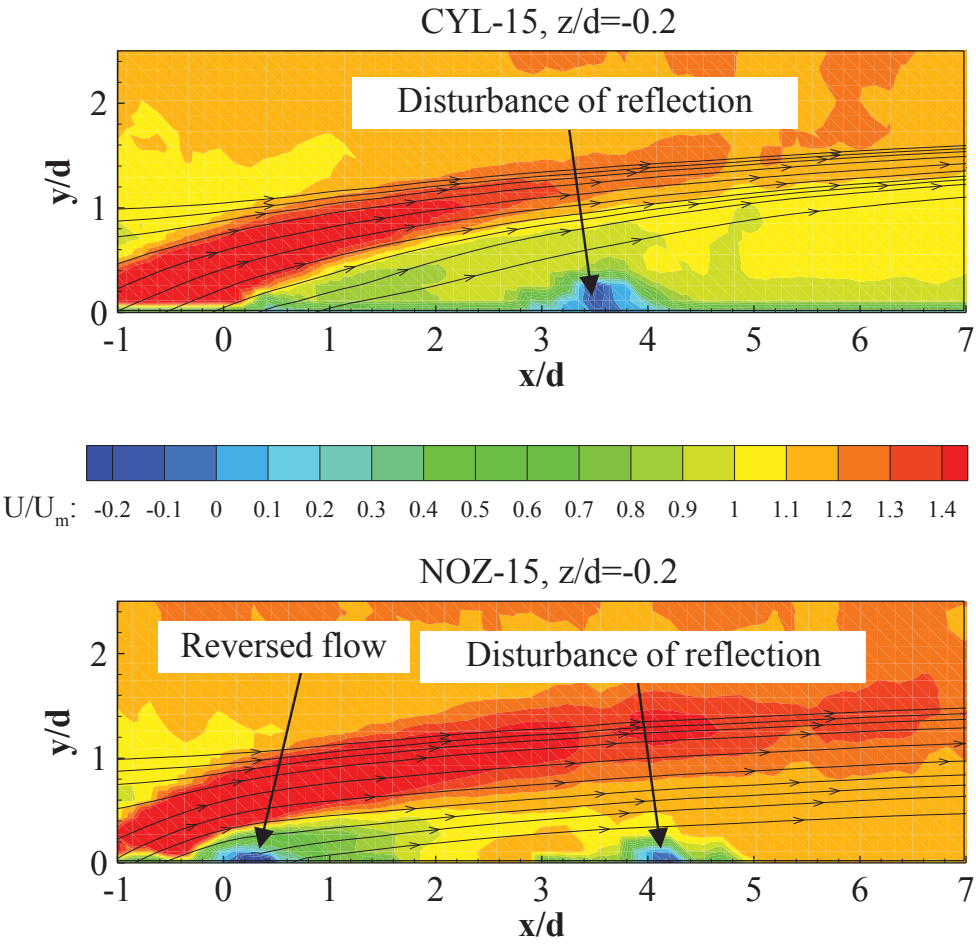

Figure 4.10: Centre plane streamwise velocity field of CYL-15 and NOZ-15

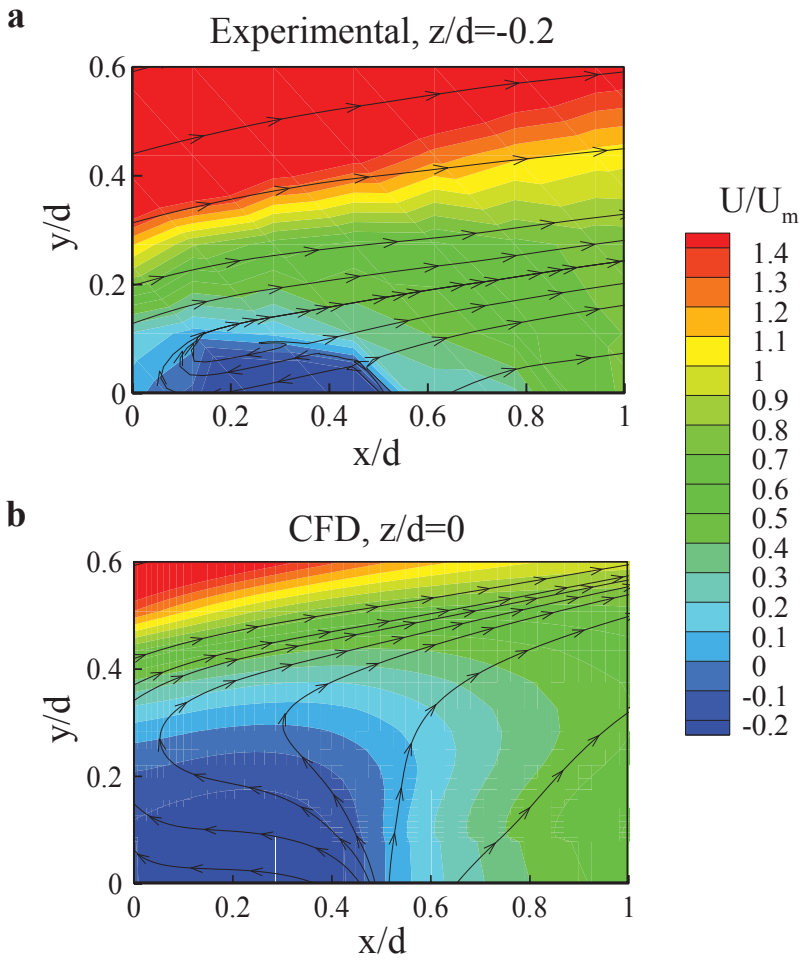

Figure 4.11: Near-hole reversed flow at centre plane, a) experiment at *BR*=1.5, *DR*=1, *I*=2.25, b) CFD at *BR*=2, *DR*=2, *I*=2

The centre plane velocity profiles are compared with reference the mainstream-only velocity profile in Figure 4.12. Good overlapping agreement among mainstream profile and both injection profiles in higher portion suggests that the region is basically unreached by the jets in both cases. As with the low blowing ratio, the nozzle jet shows a stronger velocity gradient in the near-hole region as shown at $x/d = 0$. The streamwise velocity peak reaches $2.5U_m$ at $y/d = 0.7$, while the near-surface portion shows reversed flow. The large gradient dissipates quickly after injection due to the existence of high shear, while the nozzle jet velocity profile starts catching up in the region near the plate surface. After $x/d = 3$, fast profile of nozzle jet is seen near the surface. It should be noticed that the cylindrical jet profiles share a large portion with the mainstream-only profile, and only its velocity peak is convex out of the velocity profile at most of the locations in Figure 4.12. It may suggest the fact that cylindrical jet lifts off clear from the surface at the centre plane. With NOZ-15, despite the high-position velocity peak, faster near-surface profile suggests that more jet fluid moves close to the surface than with CYL-15, which is clear after $x/d = 3$. The velocity profiles become more orderly at $x/d = 8$ for both cases. However, the nozzle jet still has a higher streamwise velocity in the bulk, while the cylindrical jet is almost diffused into the mainstream. The high velocity of the nozzle jet in the far downstream region is considered to be the effect of less CRVP strength, which reduces the mix and the consequent loss in momentum. Less momentum loss of nozzle jet keeps it at a higher velocity, while the cylindrical jet tends to diffuse into the mainstream due to a stronger mix.

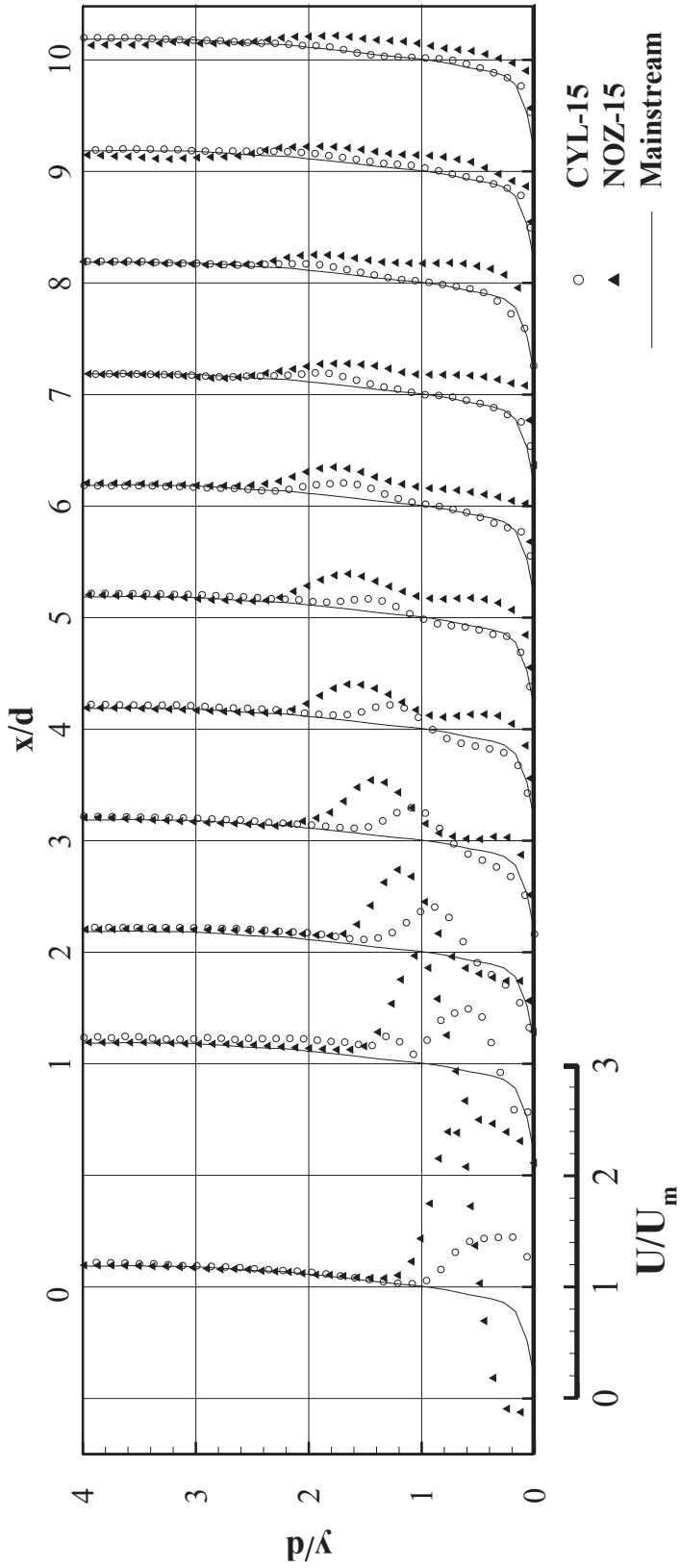

Figure 4.12: Centre plane velocity profiles of CYL-15 and NOZ-15

4.6.3 Vortex structure and vorticity fields

Not only does the nozzle jet have major differences in the velocity field, but the vorticity field downstream of the nozzle hole also shows an intriguing phenomenon. The nozzle jet features double-decker vortices in the region near the hole exit at blowing ratios of 1, 1.5, and 2. Figure 4.13 demonstrates the streamwise vorticity fields and Q value circles of both nozzle hole and cylindrical hole cases at $BR = 1.5$. Solid lines mark the area of positive Q and dashed lines mark negative Q where shear is dominant. At $x/d = 0$, double-decker vortices occur at each side of the nozzle hole at $z/d = \pm 0.5$, with the same sense as the usual CRVP. Due to the higher penetration near the hole exit (discussed above), the upper vortex cores locate at $y/d = 0.8$, higher than that of the cylindrical jet. The lower vortex pair of the nozzle jet has less strength and is closer to the surface. In the middle of the double-decker vortices at each side, the same sense vortices create high shear in the flow, which has considerable vorticity but minus Q value. The high shear tends to cause more friction and dissipates the vortex quickly.

Notable changes of the double-decker vortices happen at $x/d = 2$, as shown in Figure 4.13. The strength of the upper vortex pair of the nozzle jet drops rapidly. A slight upward movement can be seen at the upper vortex cores as the jet has high y-momentum right after injection. The lower vortex pair meanwhile grows and takes the place of the upper vortex pair as the strongest one, but the strength is still less than the vortex cores of cylindrical jet. Observing the position of vortex cores, nozzle injection and cylindrical injection are at the same level, which is around $y/d = 0.5$.

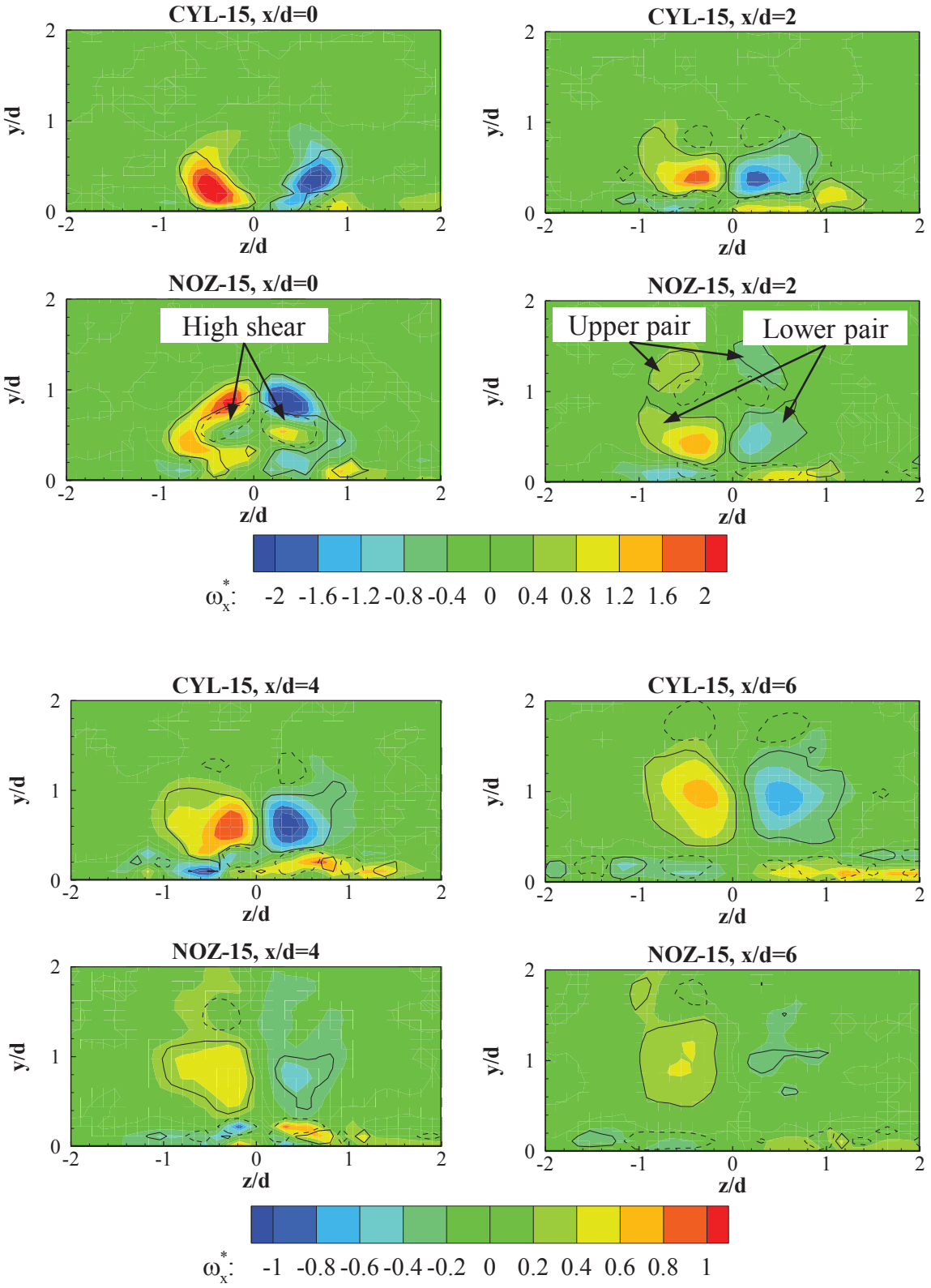

Figure 4.13: Streamwise vorticity fields of CYL-15 and NOZ-15

It can be observed that the upper vortex pair becomes very weak and absorbed by the lower pair after $x/d = 4$. Nozzle jet vortex cores have been considerably dissipated at $x/d = 6$, where there is a merged bulk of nozzle jet. At the same location, the cylindrical jet still features clear vortex cores. Comparing vortex core positions, both jets show a similar lift-off in terms of CRVP position. Generally, the upper and lower vortices tend to cancel each other out, resulting in a single counter rotating vortex pair with less strength. Less mainstream entrainment due to weak CRVP could be considered to be the reason why the merging phenomenon occurs, as the entrained mainstream would split jet bulk into two branches, similar to what happened to the cylindrical jet.

Figure 4.14 presents the wall-normal vorticity field of both injections. As a component of the vortex structure of jet in crossflow, wake vorticity exists downstream of the injection and under the main jet trajectory. It is quite evident in the case of CYL-15, where a pair of wake vortices is observed in the centre of the flow field and grow in height as they move downstream, since the room under the jet expands as the jet penetrates. In the nozzle injection case, there also exist wall-normal vortices, as shown in the figure at $x/d = 2$. The strength of them is not as great as in the cylindrical case, and they almost disappear at $x/d = 4$, because wake vortices occur with jet lift-off. The catching-up of nozzle jet takes the room for wake vortices. On the other hand, the vorticity at the lateral side of the wake vortices in both injections is due to the shear produced by the streamwise velocity difference at the interface of jet and mainstream.

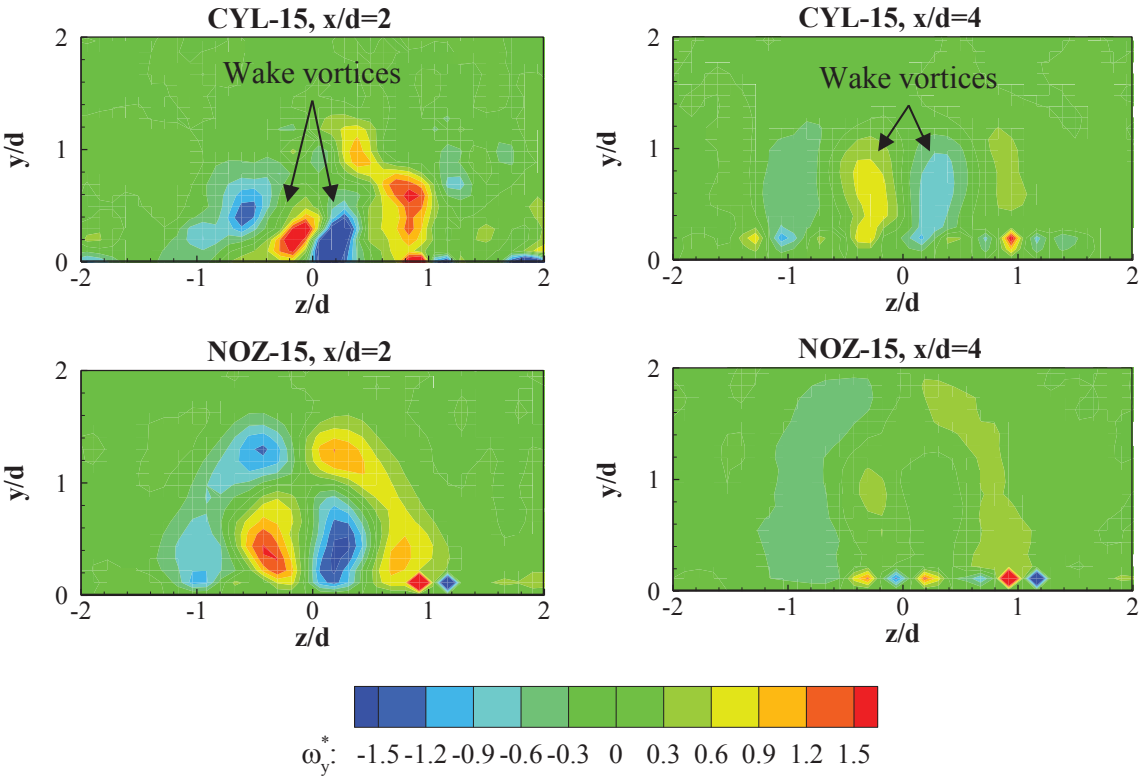

Figure 4.14: Wall-normal vorticity of CYL-15 and NOZ-15

4.7 Similarity under Different Blowing Ratios

The jet structure of the nozzle hole injection under high blowing ratios shows similar characteristics due to the absence of plate surface participating in the interactions. A comparison of velocity field at $x/d = 0$ across high blowing ratios can be seen in Figure 4.15, where a similar umbrella-shaped structure and reversed flow regions are observed at the three high blowing ratios. A difference in velocity magnitude exists simply because the blowing ratio is different. Under $BR = 2$, quite strong CRVP is observable from the velocity vectors in both cylindrical and nozzle jets. Due to the similarity in velocity fields, the merging phenomenon can be expected to happen at blowing ratios of 1 and 2. Figure 4.16 shows the iso-surface of

$U/U_m = 1.22$ at $BR = 2$. The view angle is at a low position under the plate surface, which makes it possible to observe the merging phenomenon of nozzle jet that starts at around $x/d = 5$. It forms quite a round jet flow further downstream, whereas the kidney shape of cylindrical jet remains throughout the range, leaving the lower centre filled with the entrained mainstream. The velocity iso-surface of the nozzle jet is much closer to the plate surface, which could suggest better coolant coverage for film cooling applications.

As discussed with the velocity fields, the vorticity fields also suggest similar features of the nozzle jet at $BR = 1.0$ and $BR = 2$, as shown in Figure 4.17. The measurement plane is at $x/d = 0$, as with the velocity fields above. The increase in vorticity with increasing blowing ratios is clear for both hole geometries.

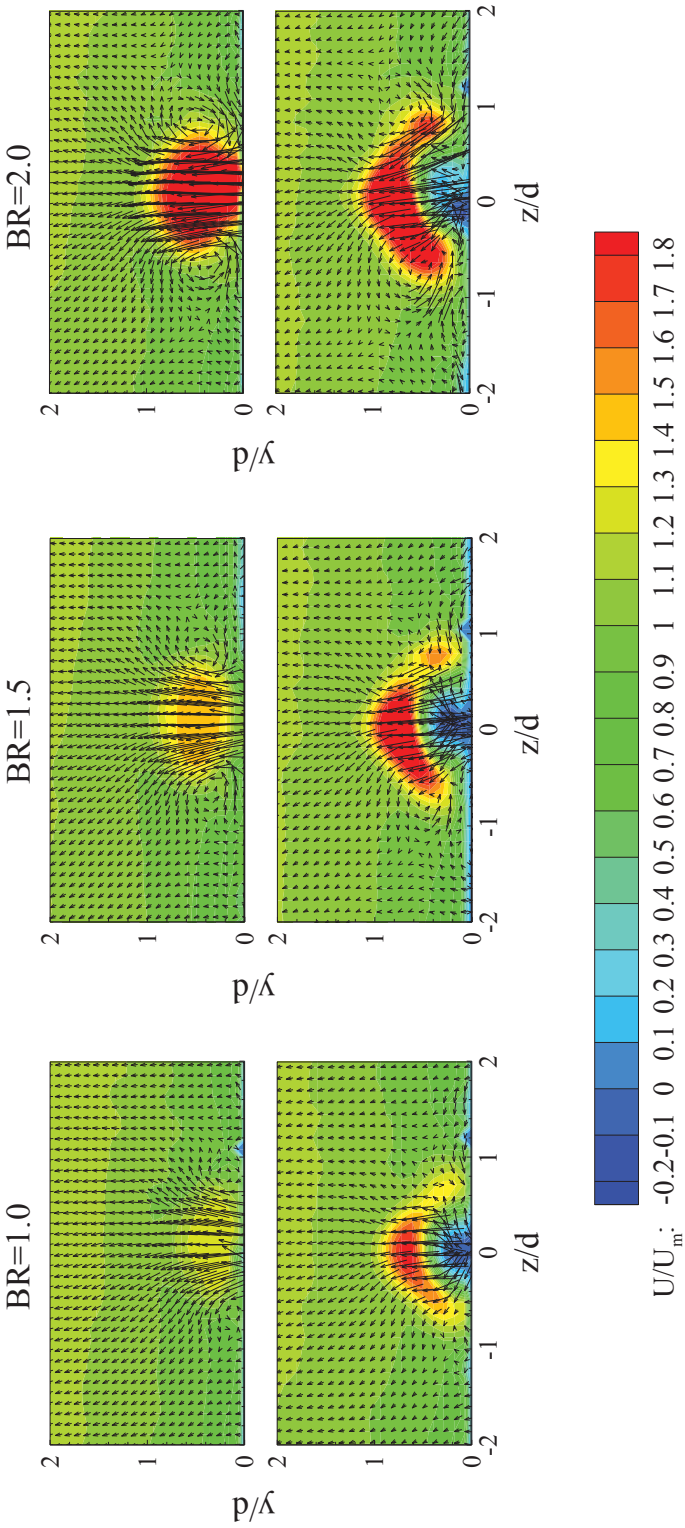

Figure 4.15: Velocity field with various blowing ratios, upper: CYL, lower: NOZ

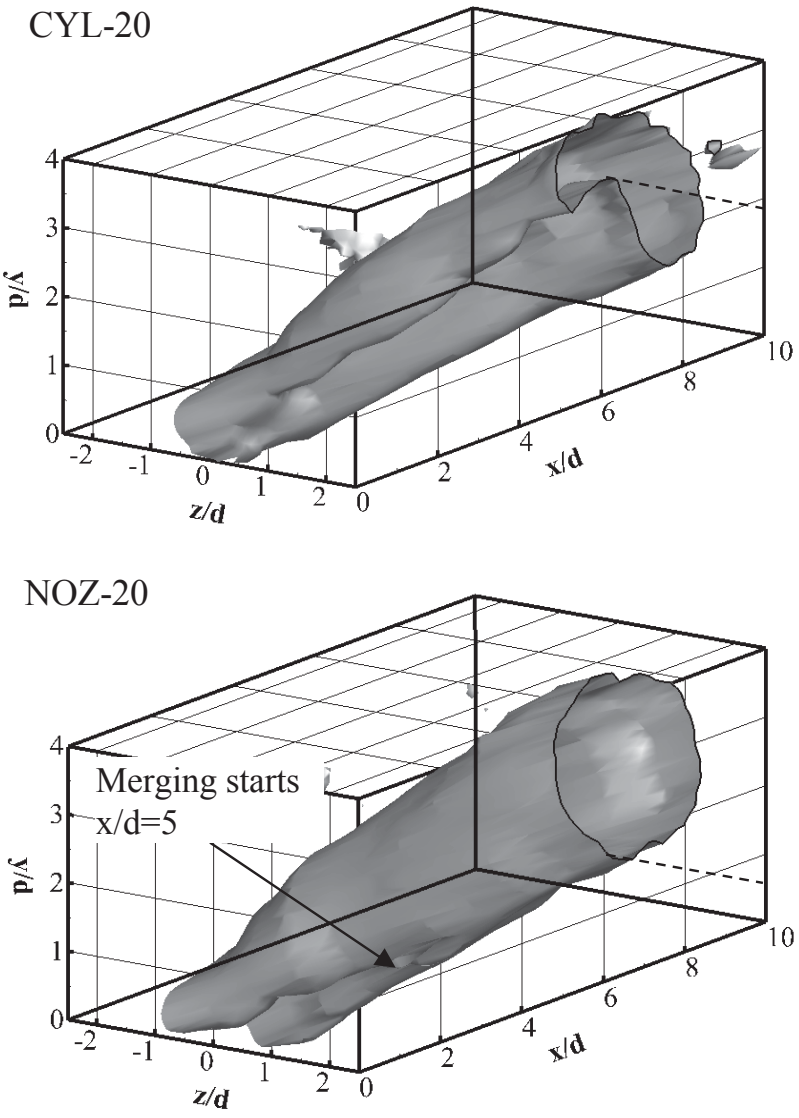

Figure 4.16: U/U_m=1.22 iso-surface of CYL-20 and NOZ-20

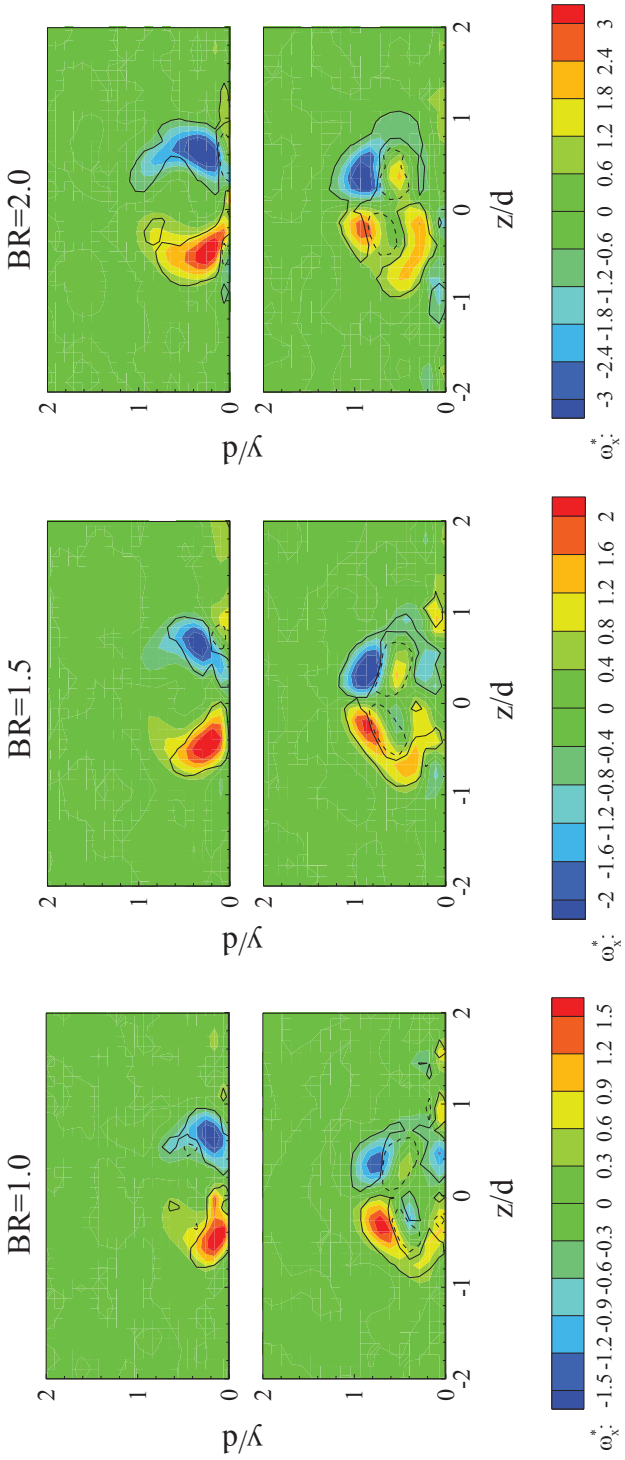

Figure 4.17: Vorticity field with various blowing ratios, upper: CYL, lower: NOZ

4.8 Jet Lift-off and Mix

CRVP strength is thought to be greatly associated with jet flow lift-off. In Haven and Kurosaka (1997), the CRVP strength was weakened by a hole exit with a large aspect ratio and it was suggested that due to the reduced CRVP, the jet lift-off was attenuated. One of the major conclusions of Walters and Leylek (2000) was that reducing the streamwise vortex strength would result in weak jet lift-off. In the present study of two schemes with same hole exit shape, the reduced CRVP strength of the nozzle jet produces a decline in jet lift-off at the centre plane in terms of slope and jet-to-surface distance (as seen in Figure 4.10 and Figure 4.16, respectively), though the velocity peaks of the nozzle jet penetrate to a higher position in mainstream at high blowing ratios, as shown in Figure 4.12. Comparing the position of the vortex cores, as in Figure 4.13, the nozzle jet does not indicate lower positions. The lower CRVP strength of the nozzle jet and less mainstream entrainment in between the two branches make it possible for the two lower branches to merge together forming better coolant coverage in contrast to split and kidney shape of cylindrical jet. In other words, CRVP strength might affect film cooling effectiveness only by jet-mainstream mix characteristics, since the jet bulks of both hole schemes are at almost the same height.

Under real engine conditions, the density ratio will be higher than the 1.0 used in the present study; it can be up to 2. Considering the effect of a denser jet, CRVP intensity could be lower for both nozzle and cylindrical cases, compared to those of the same blowing ratio but with $DR = 1$. Density difference could pull the jet of both

schemes down towards the surface, and CRVP would be weakened due to lower jet velocity and a stronger confining effect of the surface. In addition, the low momentum of jet would result in less penetration into the mainstream.

4.9 Summary

A film cooling test module was designed and fabricated to investigate the flow field downstream of a short orifice-featured injection hole at blowing ratios ranging from 0.5 to 2.0 with a fully developed turbulent mainstream. PIV-based volumetric velocity field data were collected, based on which vorticity fields were also generated. The experimental results suggest that nozzle hole injection significantly reduces the downstream CRVP strength in comparison with cylindrical injection. Jet structure is divided into two categories with respect to blowing ratio. Attached jets are observed at low blowing ratio $BR = 0.5$ for both nozzle hole and cylindrical hole injection. At high blowing ratios of 1.0, 1.5 and 2.0, cylindrical hole injection shows a common kidney-shaped jet structure with strong mainstream entrainment. In contrast, due to the reduced CRVP strength downstream of the nozzle hole, less mainstream fluid is entrained, which leads to a merged jet bulk better attached to the plate surface. Double-decker vortices are observed at high blowing ratios. The high shear between the upper and lower vorticity pairs dissipates the vorticity effectively. Reversed flow is observed near the exit region immediately after injection in nozzle cases, at both low and high blowing ratios. CRVP strength is found not to have obvious effect on jet lift-off.

Chapter 5

Effect of Orifice Geometry

5.1 Introduction

The orifice had considerable influence on the film cooling flow field. The downstream CRVP strength of the nozzle jet was found to greatly decrease, and some interesting phenomena were discovered: for example, double-decker vortices and jet merging. This chapter aims to examine the effect of various orifice widths and positions inside the injection hole, as well as to provide an in-depth explanation for the CRVP suppressing mechanism of the orifice. For most of the cases, the blowing ratio used in this phase is 1.5, at which a cylindrical jet will show lift-off and jet merging will occur for the nozzle hole injection. This could be considered a typical situation for investigating the effect of orifice geometry. Injection at a blowing ratio of 1.0 is also studied for the effect of blowing ratio. The previously examined nozzle hole inherited the geometry of an early study by the research group. Nonetheless, a short injection hole length of 1.75d might have a certain impact on the flow structure and consequently interfere with the investigation of

the effects of the orifice before issuing the jet. Therefore, an injection hole with a length of 6d is used in this chapter.

5.2 Test Matrix for Orifice Geometry Study

In order to investigate the effect of the geometrical parameters of the orifice, such as opening width and in-hole position, seven different orifice geometries were selected to conduct an independent study of each parameter. The injection hole length was extended to $6d$ to minimise the impact of an orifice close to the hole inlet. A sketch indicating the orifice geometry variations is provided in Figure 5.1 a. Orifice opening width (W) indicates the non-material opening, and orifice axial position (P) is measured from the leading edge of the hole exit. The experiments include three opening widths, $0.36d$, $0.5d$ and $0.64d$, and four in-hole positions, $0d$, $0.15d$, $0.3d$ and $0.45d$. All of them were selected based on the dimensions of the original nozzle hole geometry, which has a width of $0.5d$ and a position of $0.3d$. To investigate the effect of orifice position, an opening width of $0.5d$ was utilised, while investigating the effect of opening width, the orifice was positioned at $0.3d$ from the leading edge of hole exit. Table 5.1 summarises the geometrical parameters along with case names and JICF parameters. The original short nozzle hole was investigated again with the mainstream conditions used in this phase to see the effect of injection hole length. In addition, the short and long injection hole with the same orifice geometry were investigated at $BR = 1$ to study the effect of blowing ratio.

Table 5.1: Phase 2 test matrix

Case	Description	d (mm)	BR	DR	W (d)	P (d)	L (d)
W00P00	Cylindrical	7	1.5	1	-	-	6
W50P00	Long	7	1.5		0.5	0	6
W50P15	Long	7	1.5		0.5	0.15	6
W50P30	Long	7	1.5		0.5	0.3	6
W50P45	Long	7	1.5		0.5	0.45	6
W36P30	Long	7	1.5		0.36	0.3	6
W64P30	Long	7	1.5		0.64	0.3	6
W50P30-10	Long	7	1.0		0.5	0.3	6
NOZ-10b	Short	6.4	1.0		0.5	0.3	1.75
NOZ-15b	Short	6.4	1.5		0.5	0.3	1.75

Table 5.2: Phase 2 mainstream conditions

Q_1	230 CFM
P_1	19 psi
T_1	21 °C
$\dot{m}_m$	0.1320 kg/s
U_m	20.7 m/s
ρ_m	1.216 kg/m^3
Re_m	96500
Ma	0.06
$\overline{TI}_m$	10%

Due to the limitation in the capacity of the air reservoir, the flow rate was slightly reduced to 230 CFM so as to supply the wind tunnel continuingly without the need of breaks for refilling. The mainstream mean velocity was $U_m = 20.7\ m/s$, and the Reynolds number dropped slightly to 96500. Mainstream pressure and temperature were the same as in the previous investigations. Detailed test parameters are listed in Table 5.2.

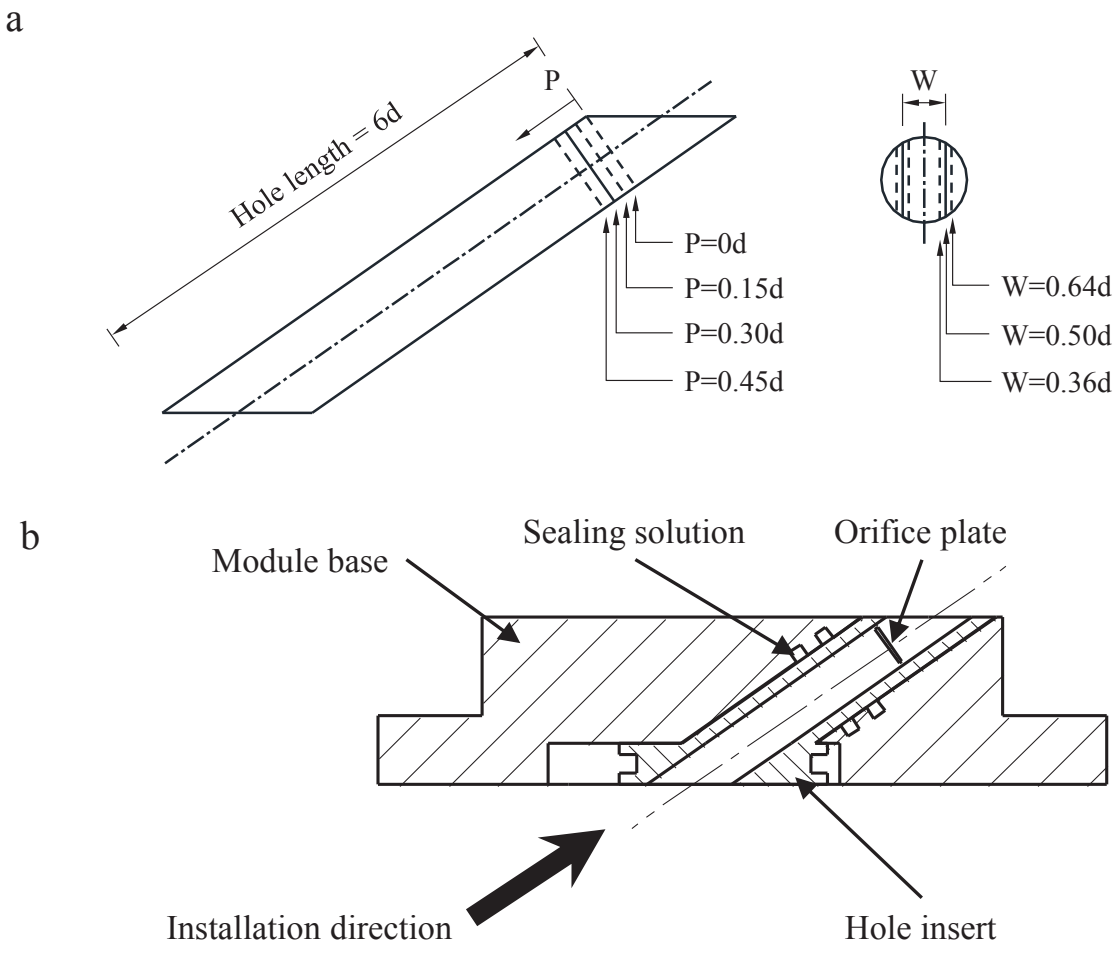

Figure 5.1: Test module for orifice geometry study: a) Sketch of orifice geometry variation, b) Test module design

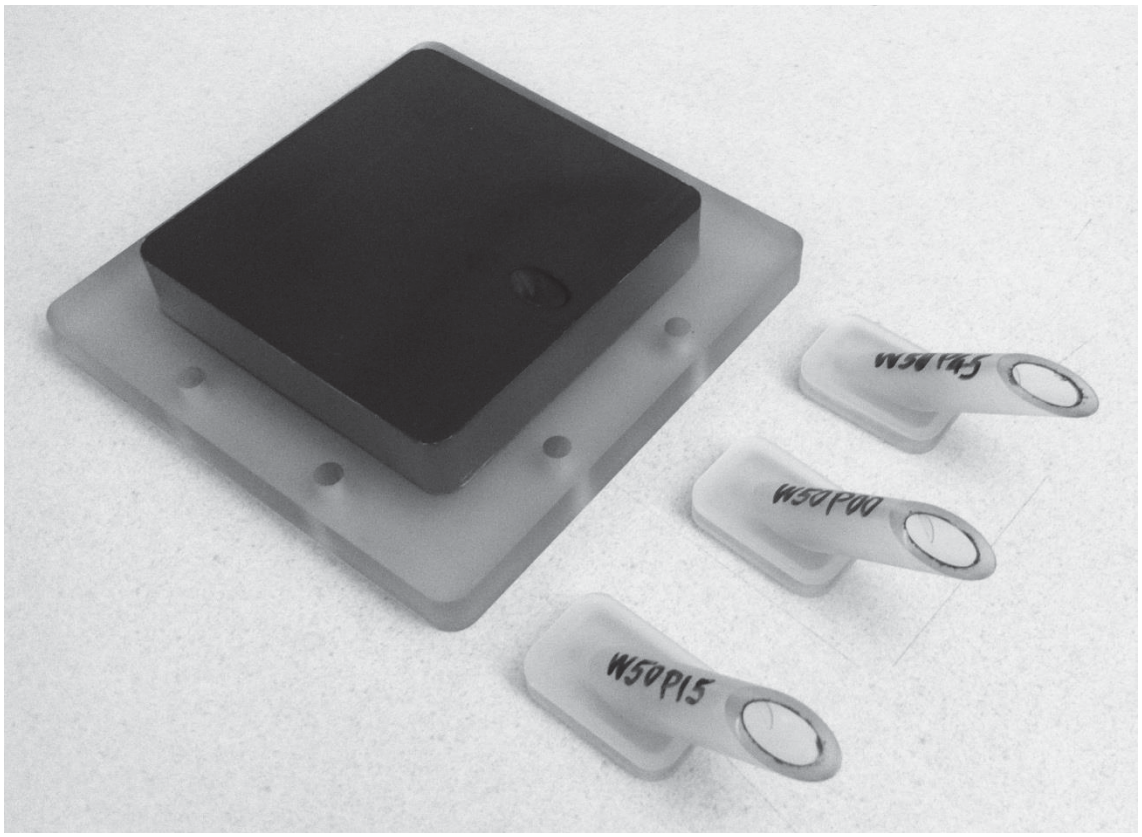

Figure 5.2: Demonstration of test module and hole inserts

5.3 Test Module

In order to reduce the cost for 3D printing, an interchangeable nozzle hole module was developed. Figure 5.1 b presents the design of the test module. The module has the same dimensions as the basic module, but has a hole mount position for installing different hole inserts. Thus for each orifice geometry, only the hole insert needs to be fabricated. The hole insert was installed from the bottom of the module base and positioned using the insert pedestal. The groove on the insert pedestal was designed to install rubber ring for more friction. A top cover was placed onto the top surface of the module to cover the gaps between the module base and the hole

insert. A bottom cover was used to cover the gap for insert installation. The assembly of the module base, hole insert and the top and bottom covers was then mounted to the test section in the same way as the basic fixed-hole module. Figure 5.2 presents the manufactured test module and some hole inserts.

5.4 Effect of Injection Hole Length

5.4.1 Inlet flow separation

It has been pointed out in many studies that the acute angle of the injection hole inlet edge causes flow separation. Figure 5.3 demonstrates the flow separation around injection hole inlet reported by Issakhanian et al. (2012). The separation occurs at the downstream side of the inner wall. Due to the existence of the separation region, the fluid has less effective cross section to get through. Therefore, the fluid flows at the upstream side of the wall and accelerates, which results in unsymmetrical velocity profiles for the in-hole flow. The flow can be recovered from separation by a contain length of tube after. According to the authors, an injection hole length of $4d$ is considered long enough to eliminate the asymmetrical velocity profile and beyond which the length has little effect on the in-hole flow pattern. The flow in a short injection hole has less possibility to recover from separation, and the asymmetrical velocity profile transmits influence onto the jet structure. The influence can be seen in some cases in the hole exit plane. The upstream part of the hole exit shows a higher jet velocity than the downstream part. This phenomenon is more obvious and influential when the hole is equipped with an orifice.

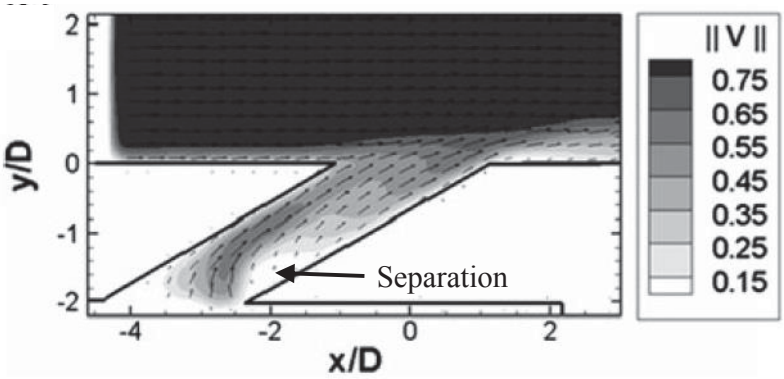

Figure 5.3: Example of injection hole inlet separation (Issakhanian et al. 2012)

5.4.2 Effect of injection hole length

A long hole length of 6*d* is used in this phase to independently study the effect of an orifice. In realistic applications, cooling hole length usually ranges from 3d to 5d. As a length greater than 4d does not have more critical impact on injection than 4d, the length of 6d can be considered close to realistic applications.

The previously investigated nozzle hole had a length of 1.75d and the orifice was located just after the inlet of the hole. A region containing reversed flow was found immediately after injection at both low and high blowing ratios, though the degree of reversed flow at $BR = 0.5$ ratio was actually quite low. The short nozzle hole was tested again with the mainstream setup being the same as the long-hole cases in this phase. Figure 5.4 compares the velocity field of a short nozzle hole (case NOZ) and the long orifice hole (case W50P30) at blowing ratios of 1.0 and 1.5. All cases had the same orifice geometry, and the only difference was hole length. The jet bulk of NOZ-10b and NOZ-15b have similar shapes as of the results under a slightly higher mainstream velocity in the last chapter. The reversed flow region is clear at both

blowing ratios, though in the cases of long hole length, the reversed flow region is not detected at both blowing ratios.

The major difference in hole length is the reason for this phenomena. In a short nozzle hole, the orifice is highly exposed to the plenum, and the flow separation caused by the acute inlet angle is added to by the separation caused by orifice plates at lateral side. Since a length of 1.75*d* is quite small, the strong separation extends itself to the hole exit and creates a reversed flow. The reversed flow region can actually be deemed part of the flow separation. Due to the existence of the separation, the jet fluid is pushed outwards, so it can be seen in Figure 5.4 that NOZ cases have slightly bigger jet envelopes.

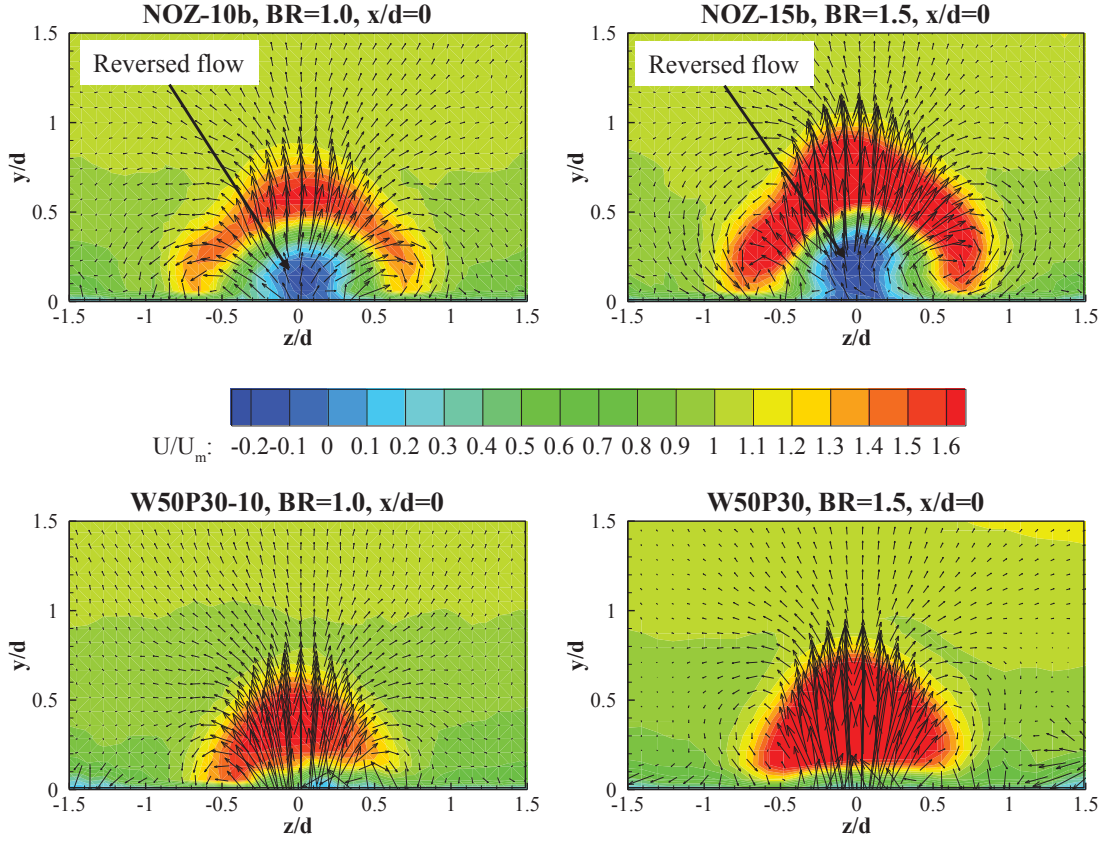

Figure 5.4: Effect of hole length on velocity field at various blowing ratios

The reversed flow makes the catch-up phenomenon occur late in short length nozzle cases. As seen in Figure 5.5, a low streamwise velocity region exists in between the two legs of the jet in NOZ cases at each blowing ratio. In W50P30 cases, the corresponding region is filled with high velocity jet fluid, which means that the merging of the jet happens earlier after the long injection hole. Figure 5.6 shows the velocity profiles at each downstream location under different blowing ratios. Slightly higher penetration of NOZ cases are observed at $x/d = 0$ due to the pushing by the separation region. At $x/d = 4$, W50P30 cases show greater streamwise velocity indicating that the jet is merged. In summary, the effect of injection hole length is mainly seen in the existence of reversed flow and delay of jet merging.

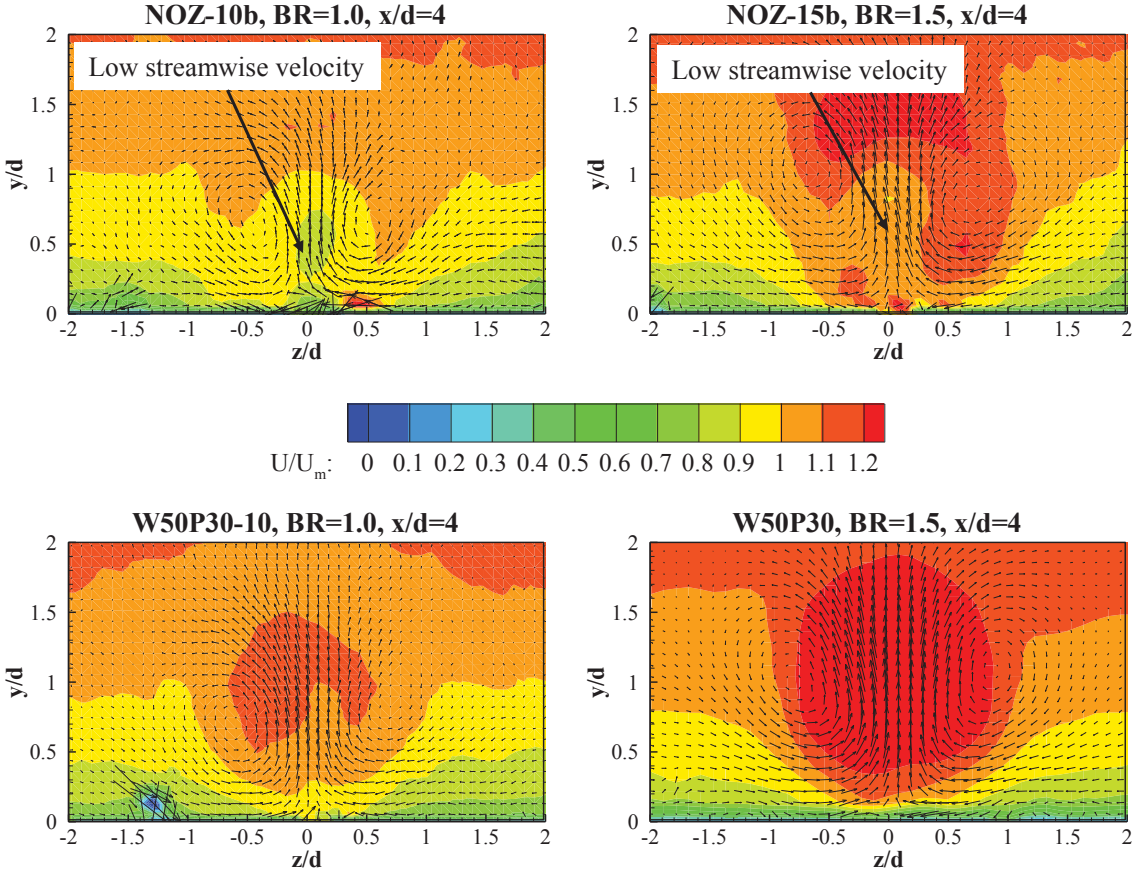

Figure 5.5: Effect of hole length on catch-up phenomenon

5.4.3 Comparison of different blowing ratios

The experimental results for the same geometry at different blowing ratios suggest that the difference in blowing ratio does not have structural impact on the flow field. As discussed in the previous chapter, from $BR = 1.0$ to $BR = 2.0$, the jet penetrates into the mainstream instead of being attached to the surface. This means that jets issued from the same geometry behave in a similar manner. For the long injection hole, a single positive velocity peak occurs in the profiles and becomes more uniform downstream. For a short injection, reversed flow region exists after injection and velocity catch-up occurs downstream. The major contribution of blowing ratio is found in the velocity magnitude and penetration height. It is clear in the velocity profiles in Figure 5.6 that the velocity peaks of both cases at $BR = 1.5$ have higher vertical positions than the counterparts at $BR = 1$.

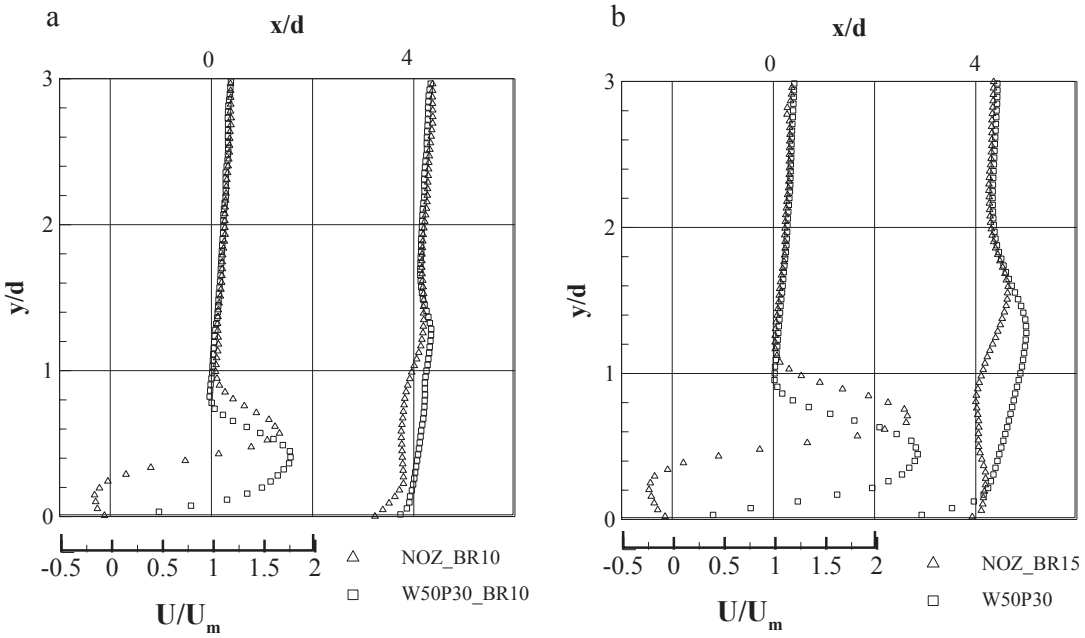

Figure 5.6: Velocity profiles comparing short and long injection hole a) *BR*=1.0 b) *BR*=1.5

5.5 Effect of Orifice Width

5.5.1 Velocity fields

It can be seen from the velocity field in Figure 5.7 that at $x/d = 0.5$, a kidney-shaped jet is seen for all the cases, but the difference in velocity magnitude is huge. The orifice accelerates the jet as the opening shrinks. In the W36P30 case, the streamwise velocity almost doubles that of case CYL.

The counter-rotating vortex pairs are clearly observed from the vectors in Figure 5.7 for all the cases. The centres of CRVP vectors are marked by the letter "C". It can be seen that in the cylindrical case the CRVP cores have higher in-plane velocity than those orifice cases. The high velocity radially extends from the centre of CRVP cores. On the one hand, the length of CRVP vectors becomes shorter in orifice cases as the opening reduces. However, high vertical momentum occurs between the CRVP cores due to the acceleration caused by the orifice, which brings the CRVP centres to slightly higher positions in orifice cases. Spanwise positions of CRVP suggest little difference between orifice and cylindrical cases. The cores are at $z/d = \pm 0.6\ to\ 0.7$.

The streamwise velocity profiles of each orifice width are compared with the cylindrical case in Figure 5.8. Orifice width apparently has a strong effect on jet velocity. At $x/d = 0$, all the velocity profiles have a jet portion near the surface. As usual, the cylindrical jet lifts off from the surface at $x/d = 2$, which confirms with the velocity profile in previous investigation phase. At the same location, the catch-

up phenomenon near the surface becomes visible in the velocity profiles of orifice cases, indicating merged bulk emerges in these cases. Comparing the profiles at $x/d = 1$ and $x/d = 2$, it can be seen that the phenomenon is most notable in case W36P30 and continues further downstream. At $x/d = 7$ where the cylindrical jet is almost diffused into mainstream, all the orifice jets demonstrate high velocity bulk flowing over the surface. W36P30 shows the fastest velocity profile, since it has the highest momentum in jet fluid.

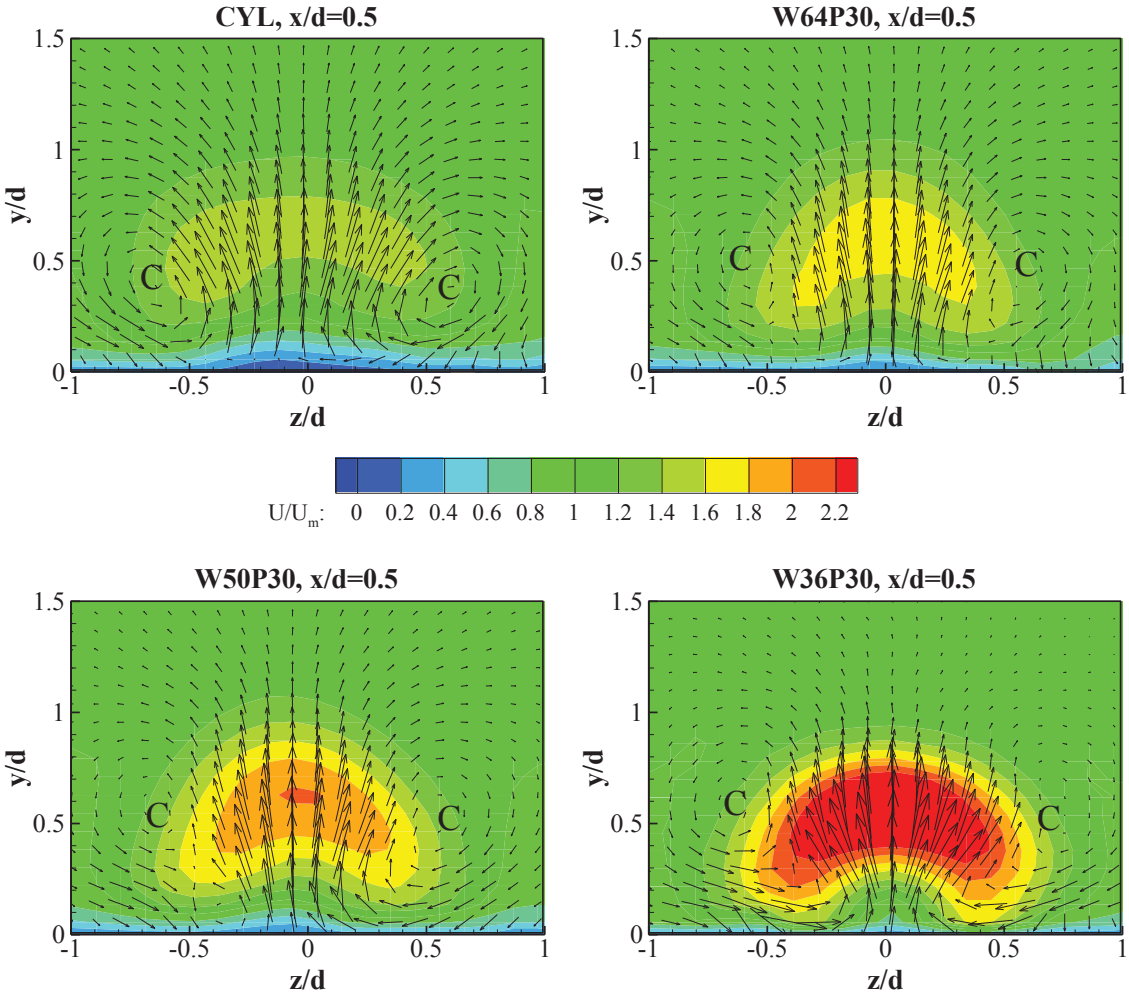

Figure 5.7: Velocity field vs. orifice width at x/d=0.5

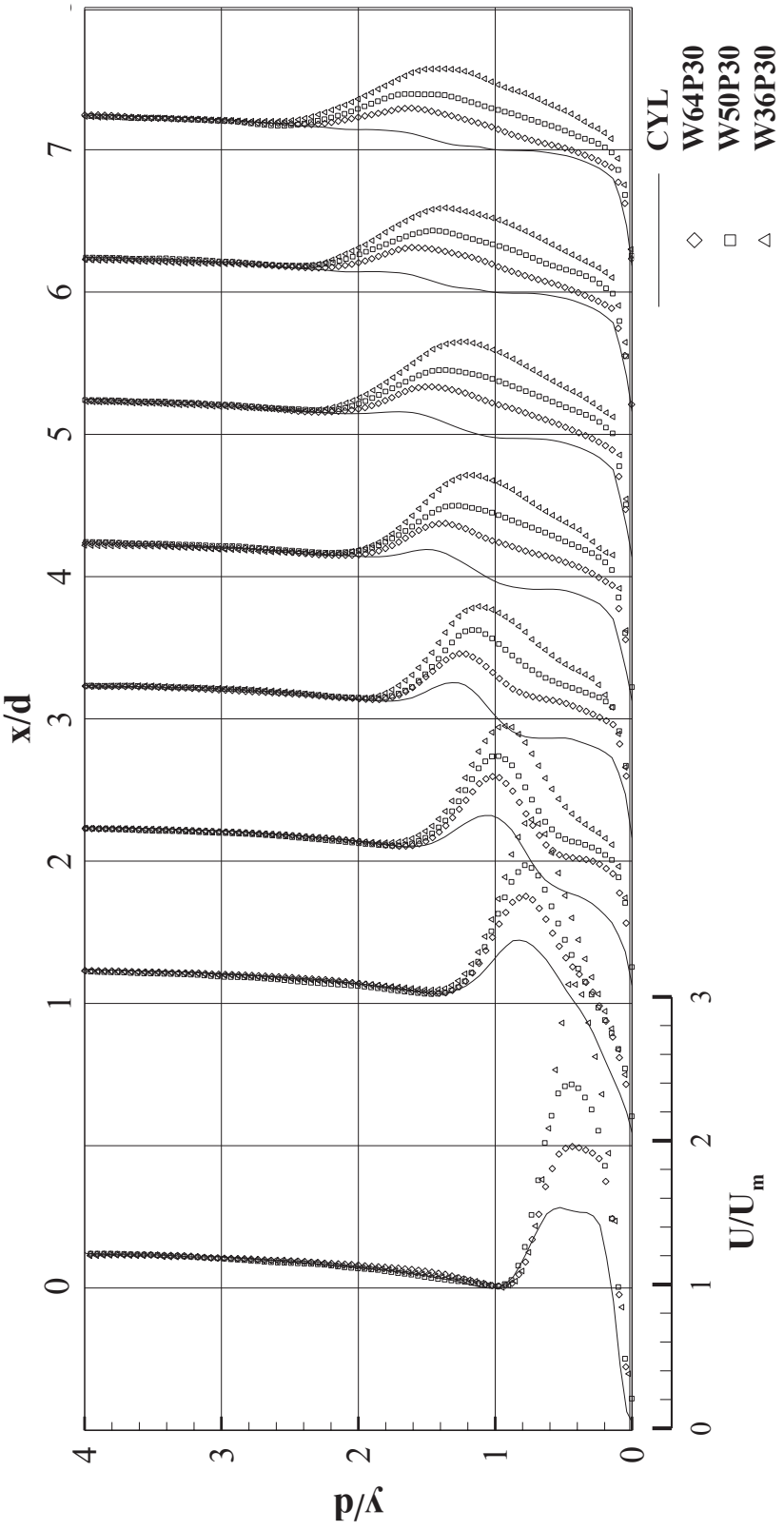

Figure 5.8: Streamwise velocity profile vs. orifice width

Figure 5.9 presents the cutaway streamwise velocity iso-surfaces of each case, from which the jet structures are clearly observable. The streamwise velocity of CYL slows down quickly after injection. A large-scale cavity of low velocity fluid occurs far downstream at $x/d = 10$. In case W64P30, a relatively small kidney-shaped jet occurs at $x/d = 10$ with a higher velocity in jet. The kidney-shaped structure disappears as the orifice is narrowed. Round jet bulks are seen far downstream in W50P30 and W36P30 cases. The iso-surfaces of W36P30 are more densely piled up near the surface at the downstream end, indicating strong wall-normal gradient in streamwise velocity. This is due to the large velocity maintained throughout jet flow that changes the boundary layer velocity distribution on the centre plane.

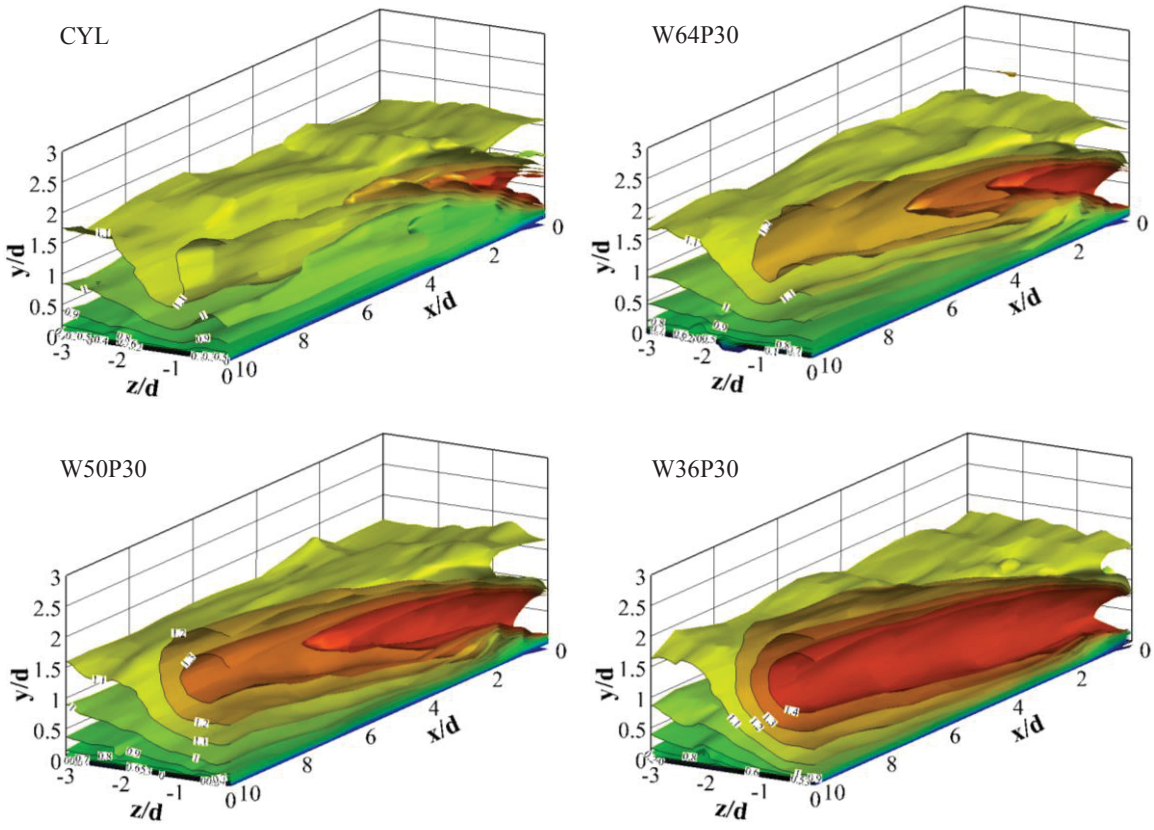

Figure 5.9: Velocity iso-surfaces of orifice width variation

5.5.2 Vorticity fields

Typical CRVP arrangement is found in the CYL case, as shown in Figure 5.10. The intense vorticity sits around $z/d = \pm 0.5$, as they are mainly developed from the hanging vortices at hole lateral edges. It can be seen that the centres of CRVP cores in the CYL case are close to the peaks of vorticity. The deviation of the vorticity peaks from the CRVP cores is attributed to the fact that the entrained fluid towards the centre plane is drawn upwards by the wall-normal momentum of the jet. Strong vorticity is then generated. In orifice cases, the distance between CRVP cores and vorticity peaks is greater. In fact, the CRVP vectors in orifice cases carry much lower vorticity. The intense vorticity is found within the lateral span of the injection hole found between $x/d = 0$ and $x/d = \pm 0.5$. This is a major effect of the orifice. The phenomenon is quite clear in the vorticity field and vectors of the W36P30 case in Figure 5.10, since its opening is quite narrow. The region of intense vorticity finds its vortical source in the rapidly turned vectors, as the fluid passes through the orifice. Due to the very narrow opening, the turning of the vectors has more bending than in W64P30 and W50P30 cases.

Figure 5.11 depicts the Q value and vorticity of the four cases at $x/d = 0.5$. The CYL case shows a typical CRVP structure, and the Q value contour matches with the lines marking its vorticity, where dash lines indicate negative vorticity. A shear region exists under each vortex core as the fluid flows over the surface. Case W64P30 has the weakest vortex pair at this location. As the orifice opening becomes narrower, stronger vortex cores emerge in the flow and higher shear appears above

the vortex cores, which has few traces in the CYL case. The narrowest opening of W36P30 delivers a vortex pair of high intensity. Accompanying the intense vorticity, there are high shear regions above and under the vorticity cores.

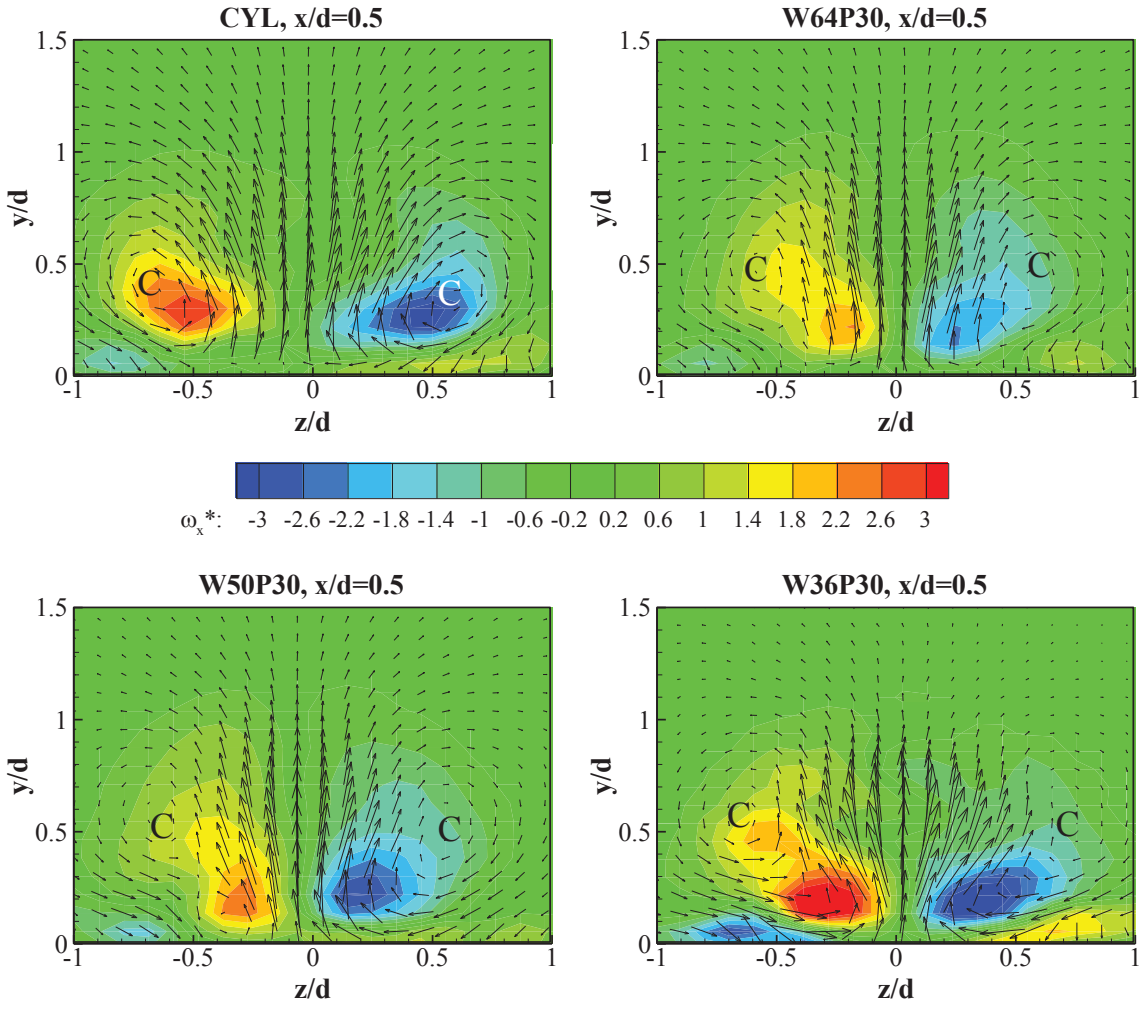

Figure 5.10: Streamwise vorticity vs. orifice width at *x/d*=0.5

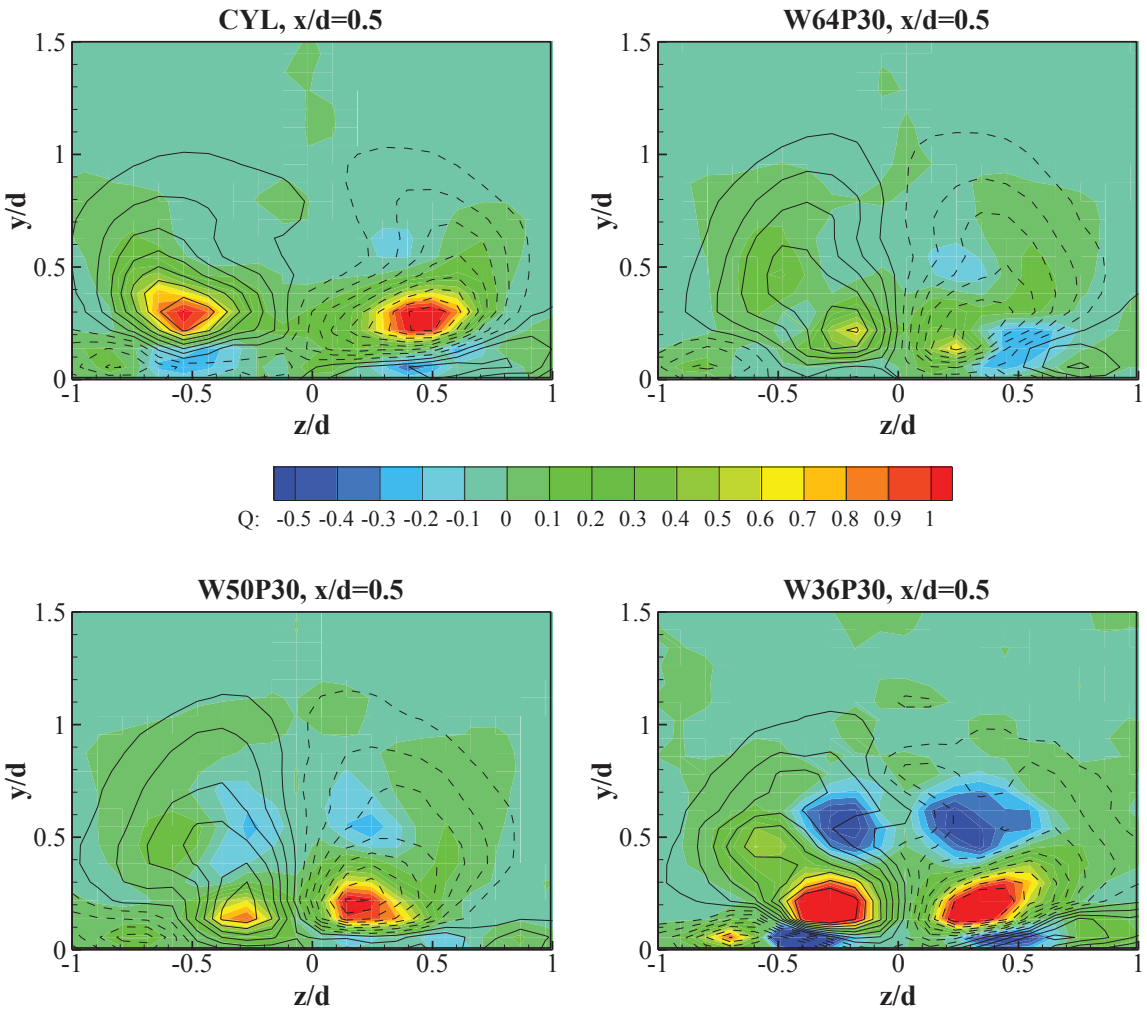

Figure 5.11: Q value field vs. orifice width at x/d=0.5

The strong after-orifice vorticity decays quickly downstream as after-orifice turning gradually fuses into CRVP vectors. The strong shear is important in this process. Case W36P30 has the most significant vorticity drop. Figure 5.13 presents the vortex strength in each case at $x/d = 4$, and case CYL reveals the highest CRVP strength. The circulation of vectors is clear in the figure, and it can be seen that case W36P30 has the weakest CRVP, though the most intense after-orifice vorticity is found around its exit. Among orifice cases, W64P30 has the weakest effect on reducing vortex strength. It almost doubles the vorticity observed in case W36P30.

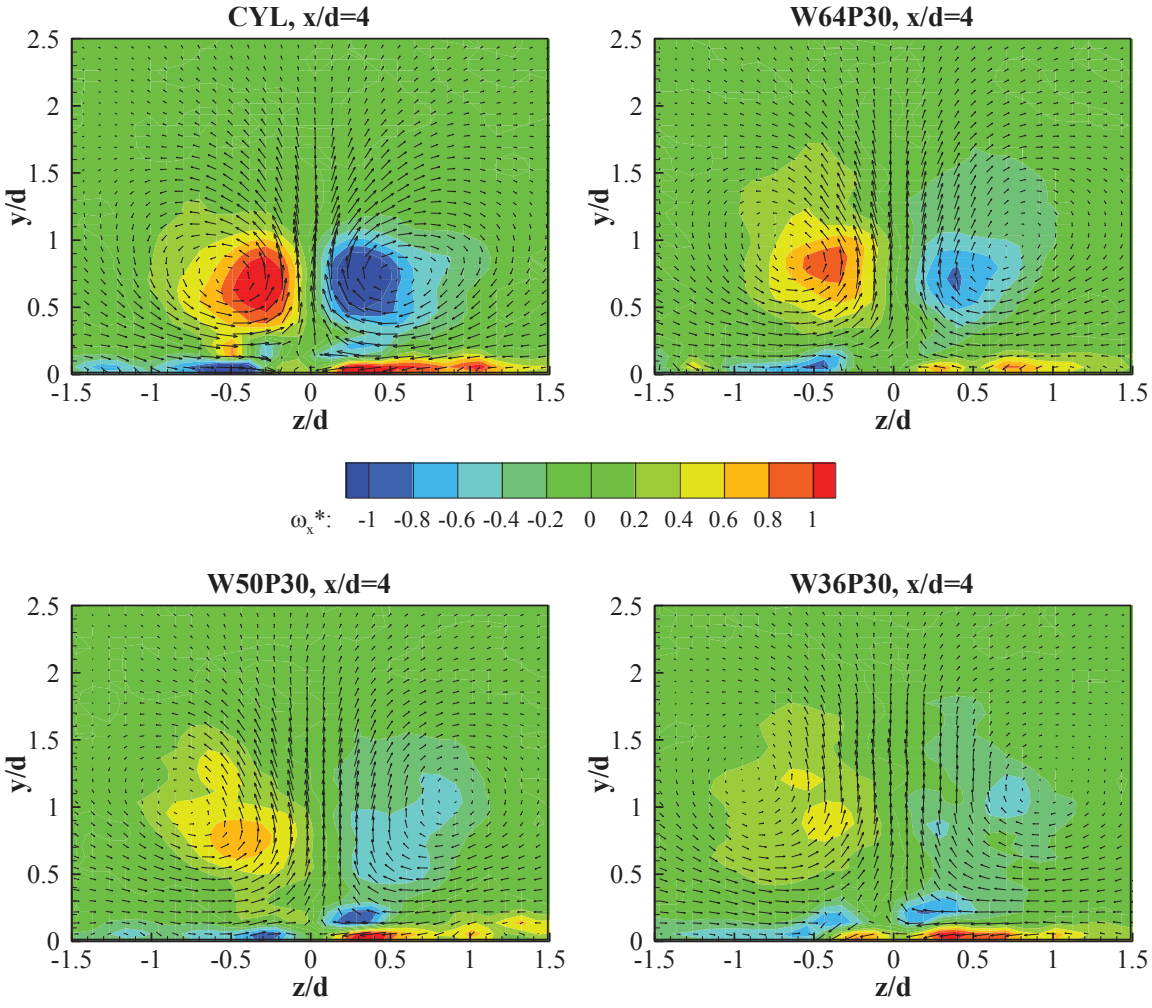

Figure 5.12: Streamwise vorticity vs. orifice width at *x/d*=4

5.5.3 Downstream vorticity variation

The near-hole region is a critical area for the orifice to apply its effect. Further downstream, a stable vorticity decrease is seen for all the cases. Figure 5.13 presents the peak vorticity of the vorticity fields of each case. All the orifice cases suggest lower vorticity than in CYL after $x/d = 0.5$. Case W36P30, with the narrowest opening, has the strongest effect in reducing vorticity after $x/d = 1$, and the orifice with the widest opening is the least effective among them. It can be pointed out that the orifice plate area is an important factor. A larger area would help reduce downstream CRVP after injection, despite the fact that it might cause some intense vortical structures inside the hole and immediately after the exit. For example, case W36P30 shows the highest vorticity before $x/d = 1$ and W64P30 is at the opposite end. This is attributed to the after-orifice vortex. A narrower opening creates stronger after-orifice vorticity in the region near hole exit. This kind of vorticity dissipates and merges into CRVP after $x/d = 1$. Although they have the same rotational sense in the *yz*-plane as downstream CRVP, their contribution to CRVP development is minor, which is observed from the case of W36P30 and W64P30. The high after-orifice vorticity (Figure 5.13, W36P30 at $x/d = 0$) does not help increase CRVP. Vice versa, the weak after-orifice vorticity (Figure 5.13) does not suggest weak downstream vorticity.

The curves of all cases bear a relatively mild vorticity decrease from $x/d = 0.5$ to $x/d = 1.5$, and W64P30 cases even shows a slight increase at $x/d = 1$. A similar feature can be found in previous experiment results of cylindrical jet at $BR = 1.5$, as

shown in Figure 4.3. Considering the complex origins of CRVP, this feature might reflect one of the major contributing sources of CRVP, which is the mainstream and secondary stream shear layer induced by the warping effect of the mainstream. The enhancement is more distinct in case W64P30 and the cylindrical case.

It is common to focus on the vorticity peaks in the study of CRVP, as in Hyams and Leylek (2000) and Recker et al. (2010). As discussed, the CRVP cores do not correspond to the peak vorticity of the vorticity fields. Therefore, in the present study the vorticity at the CRVP cores is recorded separately. The locations of the CRVP cores were determined from the streamlines of the vortex, as shown in the CYL case (Figure 5.14). The cores' locations are offset from the vorticity peaks as discussed previously. In most cases, the vorticity peaks are closer to the centre plane than the CRVP cores. Figure 5.15 presents the vorticity at the CRVP cores. It is obvious that for all the orifice cases, though the orifice creates high after-orifice vorticity right after injection, the vorticity at the CRVP cores is much lower at the locations. However, it is reasonable to characterise CRVP strength using the highest vorticity in the field due to the complexity of the nature of the vortex.

In conclusion, the orifice width has its influence mainly in affecting jet velocity and CRVP strength. The jet velocity increases as the orifice becomes narrower, while CRVP intensity decreases. The jet with higher momentum can maintain farther downstream, while the low velocity jet tends to be diffused into mainstream. The stronger CRVP suppressing effect makes merging occur earlier, which provides better jet coverage over the surface. The high momentum in *y*-direction causes the

CRVP cores in orifice cases to move slightly higher than cylindrical jet, but the effect is negligible. Overall, jet coverage could be deemed improved as orifice open shrinks.

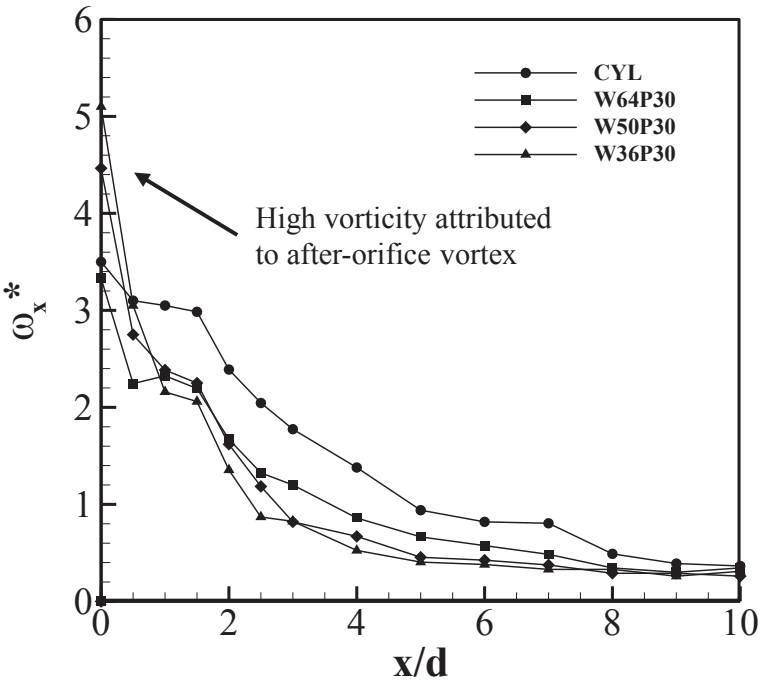

Figure 5.13: Streamwise vorticity peak of various orifice widths

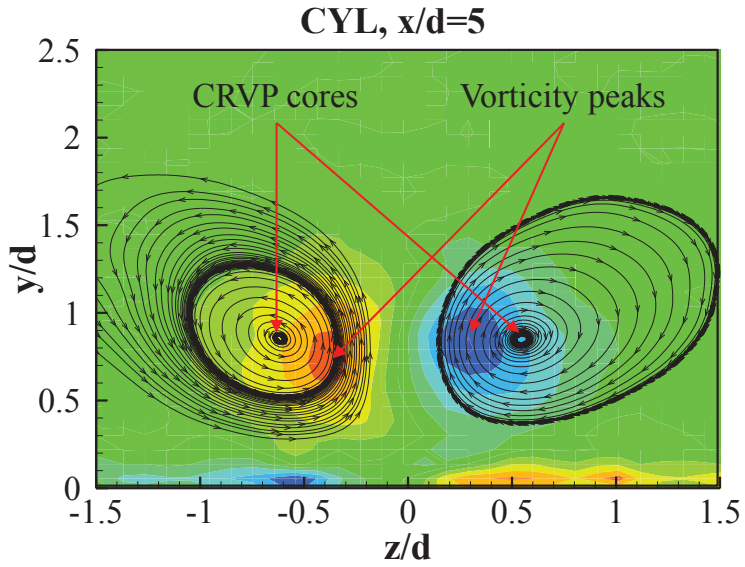

Figure 5.14: Determination of CRVP core locations

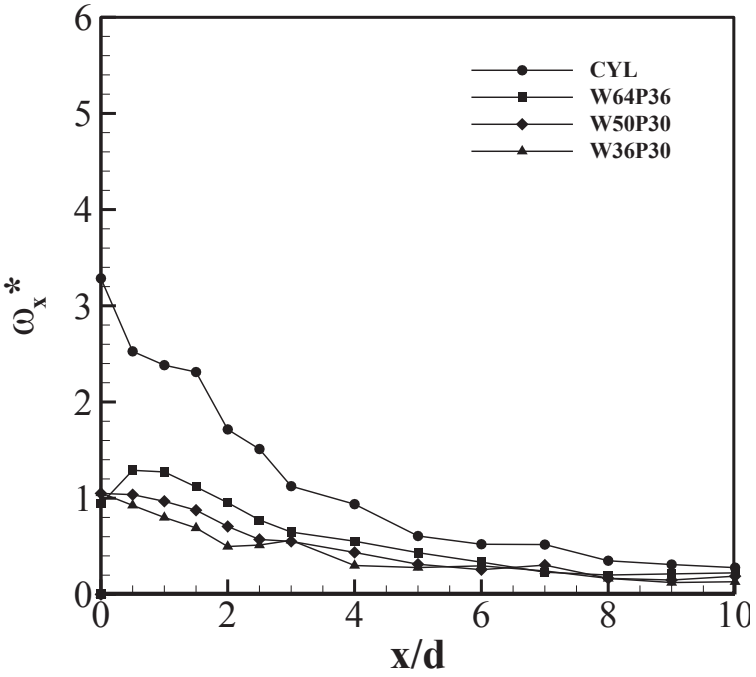

Figure 5.15: Streamwise vorticity at CRVP cores of various orifice widths

5.6 CRVP Suppressing Mechanism of Orifice

5.6.1 Formation of CRVP

The formation of CRVP is a highly complex phenomenon, involving several flow structures and interactions in the flow field, such as the in-hole vorticity existing in the boundary layer, the hanging vortices at the lateral edges of the hole exit and the mainstream wrapping after injection due to shear force. For an inclined injection, it has been pointed out in many studies that there is additional wall-normal vorticity that exists in the hole, which will later merge into wake vortices after injection. Since the jet is naturally inclined, the vorticity has components in both streamwise and wall-normal directions. According to the literature, the hanging vortices are the

major contributor to the formation of CRVP, though the other sources also promote the process.

5.6.2 Elimination of hanging vortices

The orifice was found capable of weakening the hanging vortices. In cylindrical injection, a vortex ring forms along the hole edge. At both lateral sides of the edge, streamwise vortices are generated and have the same rotational sense as downstream CRVP. The vorticity field of the cylindrical case, shown in Figure 5.16, reveals the hanging vortices at both lateral sides at $x/d = -0.5$. Obvious vortical vectors and strong vorticity in the CYL case can be seen around $z/d = \pm 0.5$, where the lateral edges are. The streamwise vorticity at CRVP cores reaches 4.3 and -4.8, respectively, and Q values are 1.5 and 2.5. These two vortical cores become major contributors to the formation of downstream CRVP. In contrast, the W36P30 case does not show strong vorticity and obvious vortical vectors at lateral edges. At CRVP cores, the streamwise vorticity and Q value are negligible when compared with the cylindrical case. The intensive vorticity is mainly within the hole and they are actually the after-orifice vorticity. Looking into the formation of hanging vortices, they develop from the boundary layer vorticity at both lateral walls inside the injection hole (Bernsdorf et al. 2006). The orifice plates at the lateral walls can cease the development of boundary layer vorticity when the in-hole flow travels over them. The hole length after orifice is not enough for redeveloping boundary layer with vorticity. Therefore, few hanging vortices are seen in orifice cases.

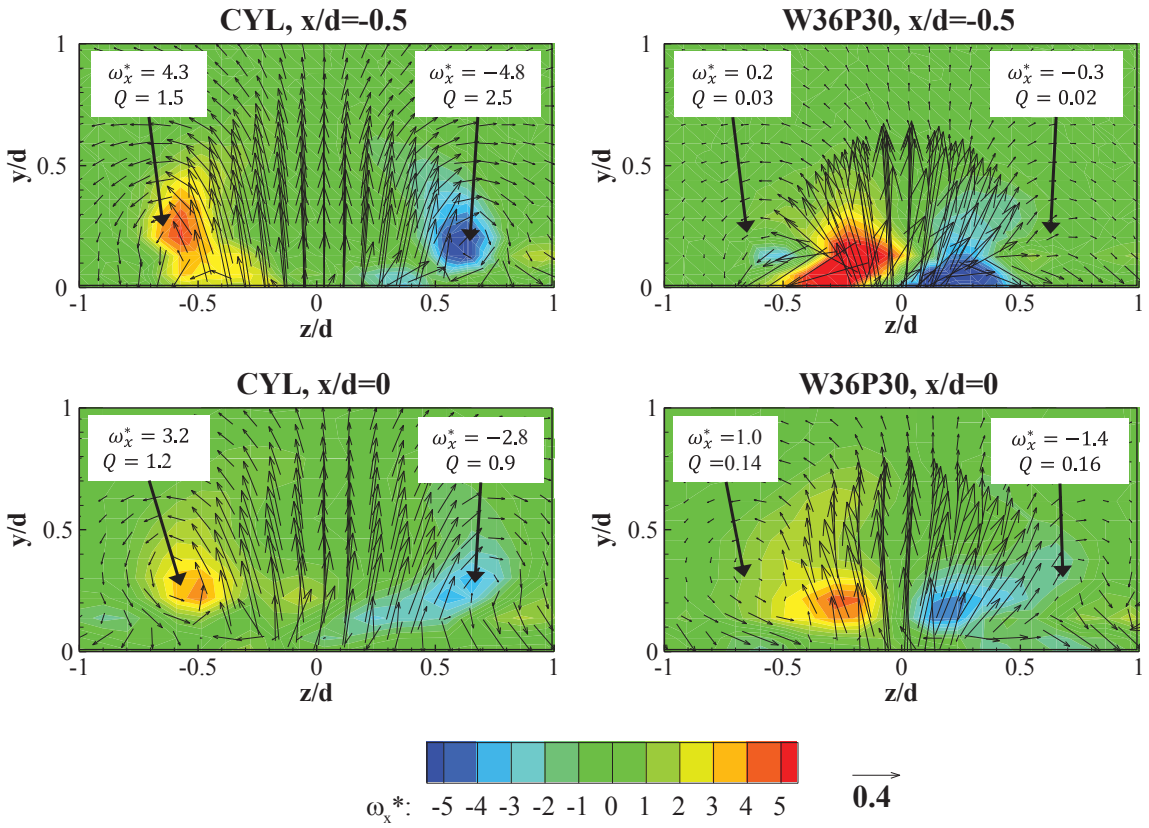

Figure 5.16: Lateral edge hanging vortices development at *BR*=1.5

The streamwise vorticity of the cylindrical jet decreases to 3.2 and -2.8 as the jet moves to $x/d = 0$, as shown in Figure 5.16. The Q value also drops to 1.2 and 0.9 for each core, respectively. The velocity vectors nevertheless suggest a more complete structure of CRVP, as circulating vectors are present. A similar formation of circulating vectors exists in the orifice case. The vortices are not as strong as seen in the CYL case, though the streamwise vorticity increase at $x/d = 0$, as shown in the Figure 5.16. This is attributed to the other sources that contribute to the formation of CRVP, and in addition, the after-orifice vorticity might also contribute. Yet the vortex strength at the CRVP cores is still much lower than that of the cylindrical jet. Overall, the orifice case shows weak CRVP at early stages of injection, which is quite

important for reducing downstream vorticity, since those contributing sources no longer have an effect soon after injection.

5.6.3 Opposite effect to in-hole vortices

The CRVP suppressing effect of an orifice is not limited to reducing hanging vortices. It can also reduce the additional wall-normal vorticity inside an inclined hole. Figure 5.17 shows the vorticity normal to the plate surface at an *xz*-plane just above the exit. The vortex ring along injection hole exit edge is clear in the CYL case, though only its y-component is demonstrated for the inclined vortex ring. The vortex pair downstream of the hole at $x/d = 0.5$ to $x/d = 1$ comprises the y-components of CRVP vorticity. The wall-normal vorticity in the cylindrical hole is clear. The in-hole vortices have the same rotational sense as downstream CRVP but their intensity is lower since the major contributors are hanging vortices. Nonetheless, breaking each source helps to impair downstream CRVP.

On the other hand, all the orifice cases feature strong after-orifice vorticity as the result of a sudden expansion. The structure of this sort of vortex is similar to the vortex ring of jet issued from a hole, yet since the orifices do not have a perfect circular shape, the vortex ring is not created. The most intense vorticity is instead located at both lateral sides according to the configuration of orifice plates. As in Figure 5.17, case W36P30 shows the most intense after-orifice vorticity as it has the narrowest opening. The strong vorticity in orifice holes have an opposite direction to that in a cylindrical hole and replace them as major vortex structure inside orifice holes. Although the strong vorticity is seen to extend over the lateral edge, they have

little effect on promoting CRVP as hanging vortices do. It can be seen in Figure 5.16 that the streamwise vorticity carried by the after-orifice vortices is weak at the lateral edges.

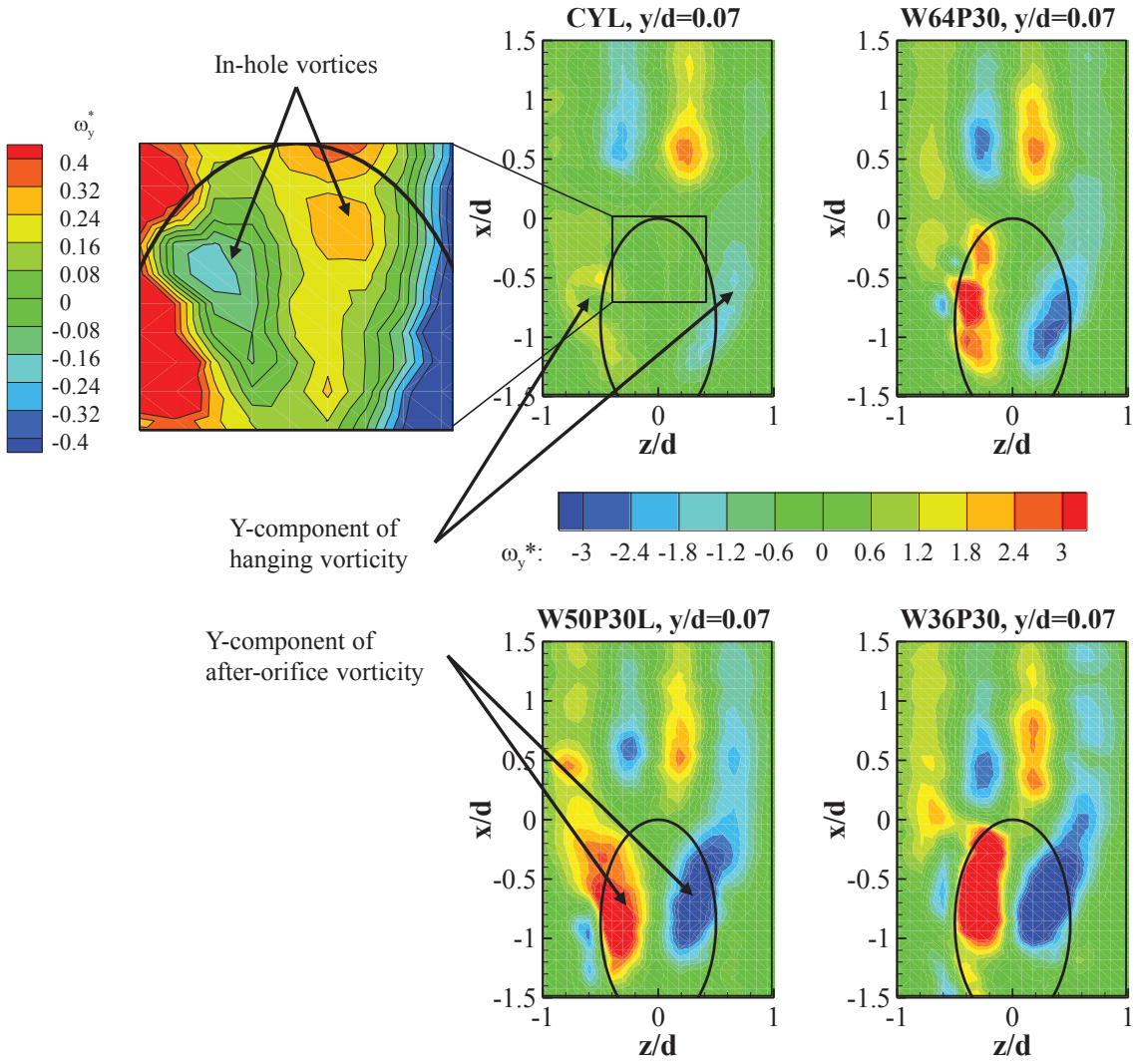

Figure 5.17: Wall-normal vorticity vs. orifice width at exit plane *y/d*=0.07

5.7 Effect of Orifice Position

5.7.1 Vorticity variation downstream of the injection

It has been mentioned that the orifice opening width has a huge impact on flow structure and vortex intensity, but the orifice position is another parameter that makes difference in flow structure. In the present study, the orifice position varies between $0d$ and $0.45d$ from the leading edge of hole exit. Despite the high jet penetration and strong CRVP in case W50P00, the other three orifice positions show obvious reductions in vortex intensity and proportional changes with respect to orifice position. Figure 5.18 gives the peak streamwise vorticity variation at different streamwise locations. W50P00 has almost no effect in weakening CRVP. The vorticity is actually higher than cylindrical jet at most of the locations. However, as the orifice moves towards the inside of the injection hole, the vorticity becomes weaker than the cylindrical case after $x/d = 0.5$. Overall, W50P45 features the lowest vorticity further downstream, though only small difference in strength is seen among W50P15, W50P30 and W50P45 after $x/d = 1.5$. However in the region near the hole exit, the most deeply positioned orifice creates the highest after-orifice vorticity, which is the case of W45P50. Similar to the cases of varying width, the high after-orifice vorticity decays quickly. Figure 5.19 presents the streamwise vorticity at CRVP cores. It can be observed that despite the impact of after-orifice vorticity, the CRVP core vorticity of case W45P50 has the lowest magnitude.

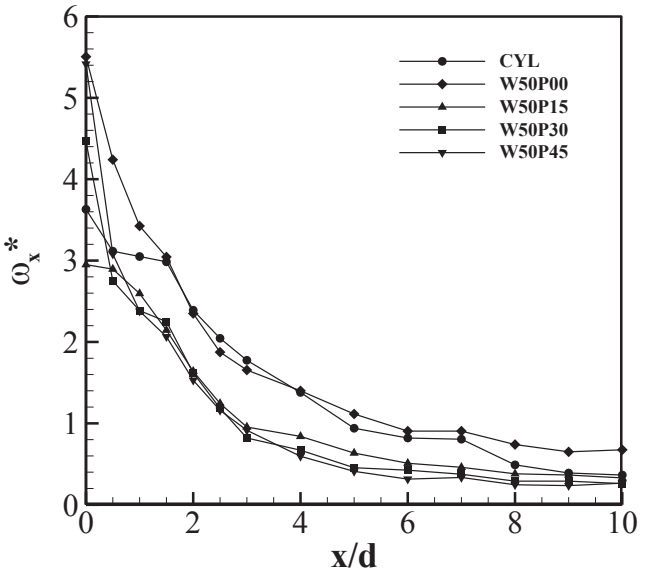

Figure 5.18: Streamwise vorticity peak with various orifice positions

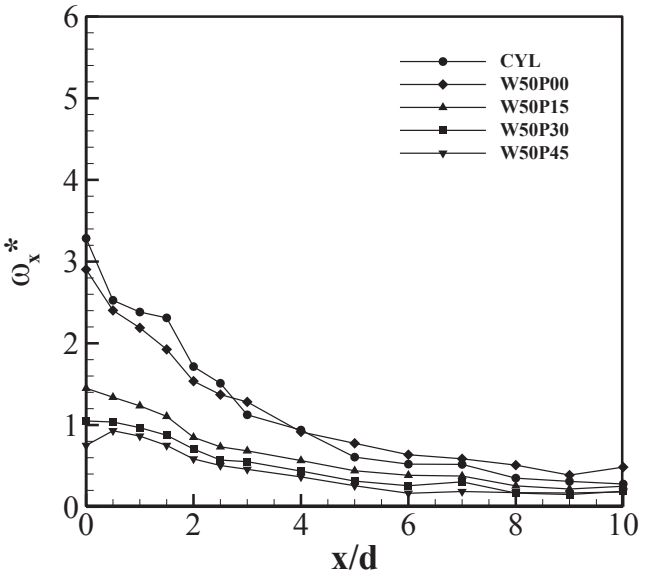

Figure 5.19: Streamwise vorticity at CRVP cores with various orifice positions

5.7.2 Velocity fields

In the velocity fields of varying orifice positions as shown in Figure 5.20, all orifice cases except W50P00 show a triangle-shaped jet bulk of similar velocity level. However, the jet bulks indicate obvious differences in bulk height and lateral

spreading as the orifice position varies. W50P15 features the tallest bulk with the least lateral spreading. The deepest-positioned orifice of W50P45, in contrast, delivers the widest lateral spreading and the least height, which is relatively a flat jet. Comparing the location of CRVP cores, the same trend can be seen as the cores move downwards and away from the centre from case W50P15 to W50P45. W50P00 suggests significant differences in the velocity field. Large scale CRVP and two streamwise velocity peaks are observed. Nevertheless, it still conforms with the trends discussed above. W50P00 jet bulk penetrates over $y/d = 1$ while little lateral spreading was seen. CRVP cores move towards the centre and find themselves in a higher position compared with W50P15.

When the secondary stream passes the orifice, the in-hole fluid accelerates due to the throat effect of the orifice. After passing the orifice, the fluid decelerates and redevelops with respect to the injection hole wall. Obviously, an orifice close to the hole exit delays the occurrence of the acceleration and the following deceleration. Therefore, the secondary stream is injected into the mainstream with different velocity as orifice position changes. Figure 5.21 compares the streamwise velocity component U/U_m and wall-normal velocity component V/U_m distribution at the exit plane. By observing the U/U_m contours, it can be seen that the W50P15, W50P30 and W50P45 cases demonstrate similar jet bulk structure in the downstream portion of hole exit, but the position of the jet moves downstream as the orifice goes deeper into the hole. Case W50P45 shows the most lateral spreading and W50P15 shows the least, which corresponds to the findings in Figure 5.20. Case W50P00 indicates that its jet bulk does not have the forward U/U_m distribution as in the

other cases. A strip-shaped jet lays over the scope of the orifice with two streamwise velocity peaks being seen, but their magnitude is apparently lower compared to the other cases. On the other hand, great wall-normal velocity V/U_m is observed in case W50P00, which almost doubles that after deeper-positioned orifices. Case W50P45 shows the lowest wall-normal velocity, pointing out the least severe jet penetration.

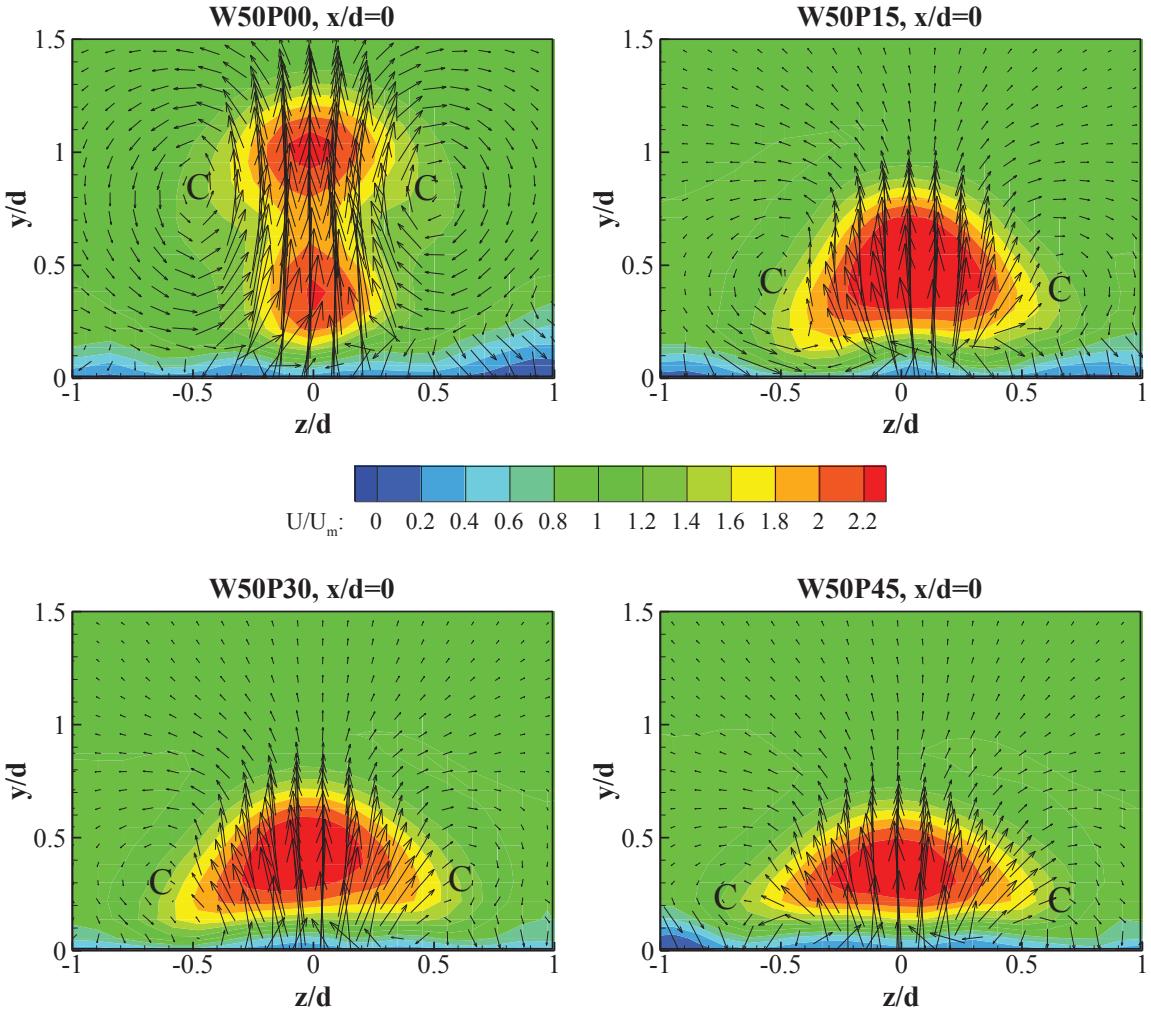

Figure 5.20: Velocity field vs. orifice position at x/d=0

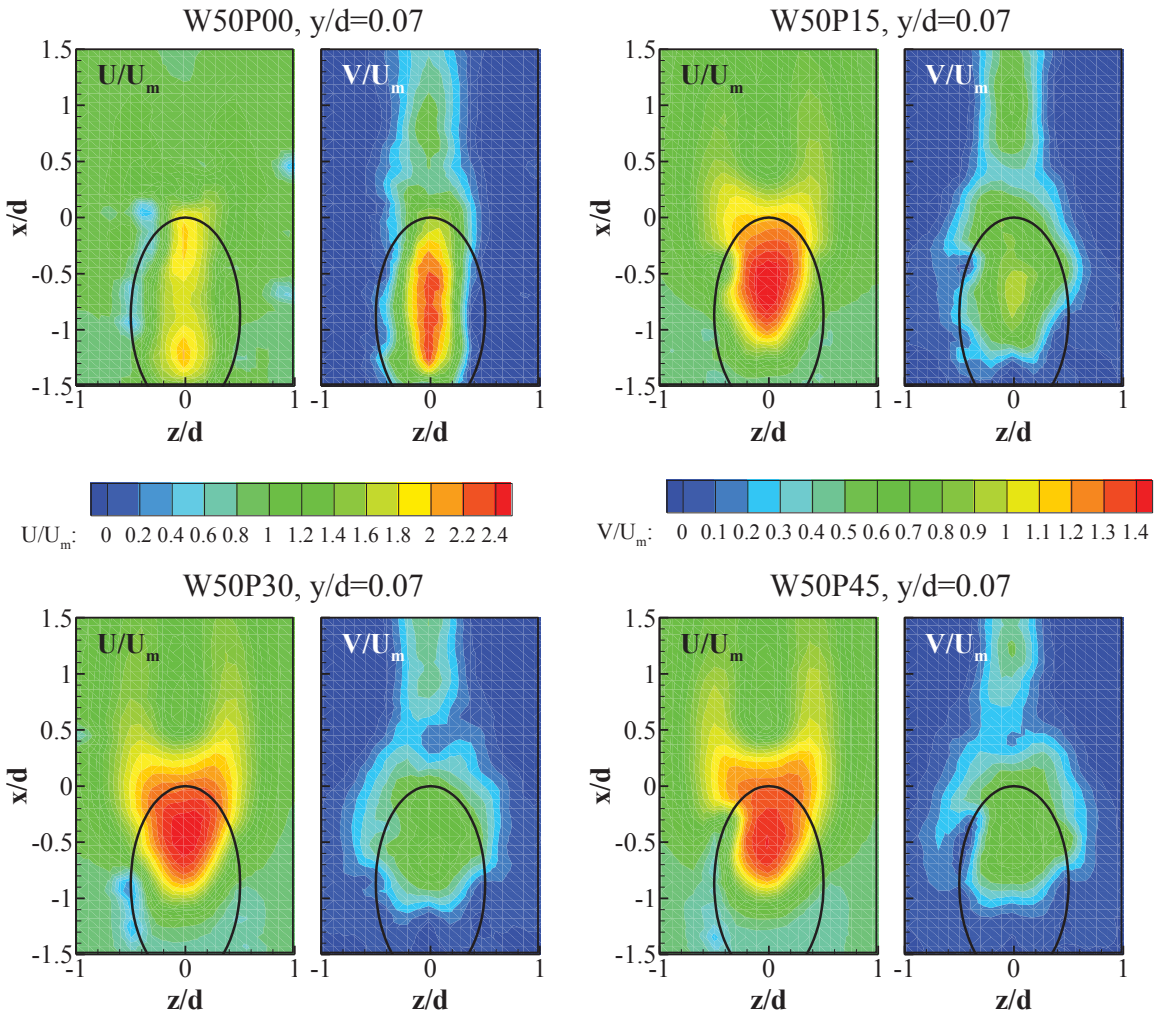

Figure 5.21: Velocity field at exit plane at *y/d*=0.07

The velocity fields at $x/d = 4$ are shown in Figure 5.22. An obvious kidney-shaped jet and CRVP are visible in case W50P00, and the jet totally lifts off and hangs at a high position due to strong wall-normal momentum. Strong mainstream entrainment occurs, since a complete kidney-shaped jet bulk is observed. It is formed due to the split effect of the entrained mainstream fluid. Among the other cases, the difference in jet structure is relatively small, though case W50P15 shows more of a tendency to form a kidney shape. The change in jet penetration characteristics is the main result of varying the orifice position. The jet bulk is seen closer to the surface with a more deep-positioned orifice.

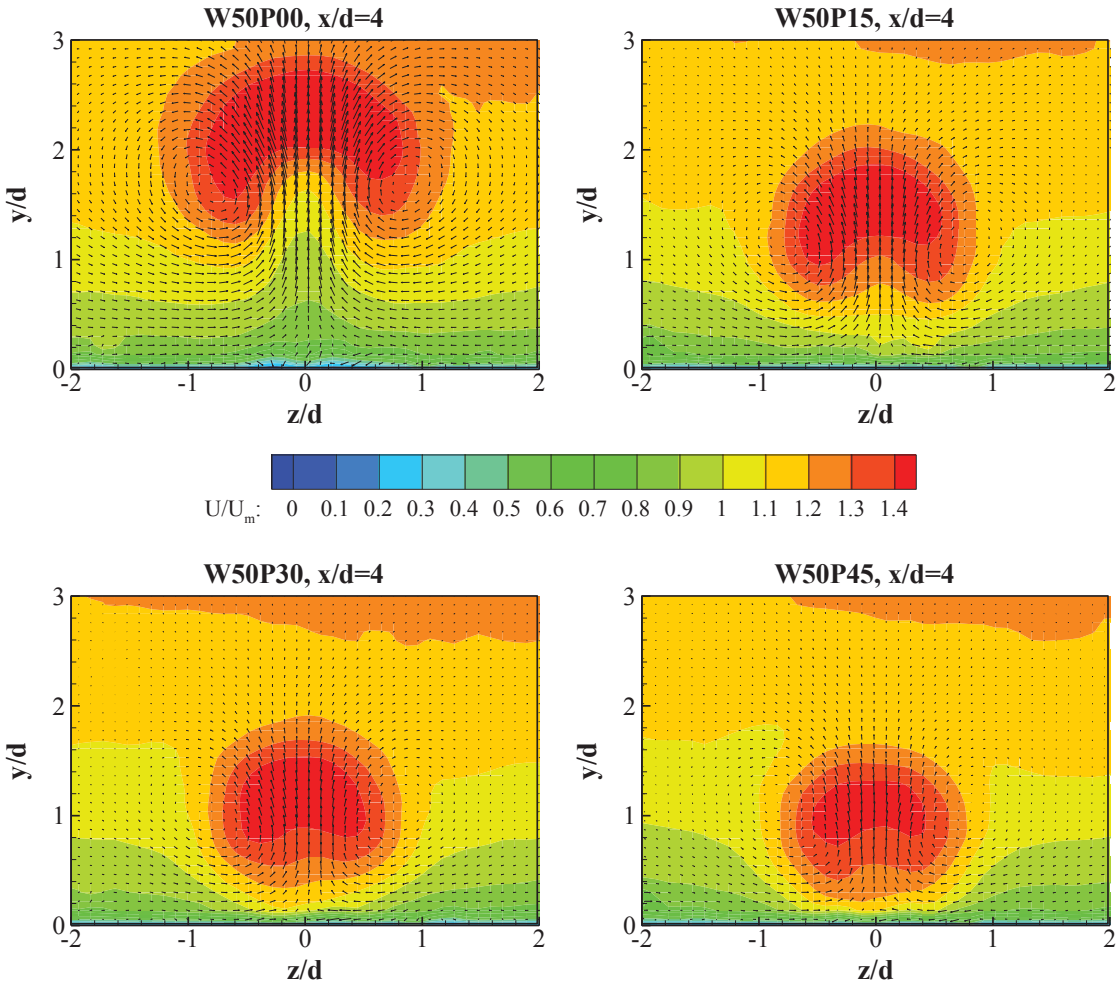

Figure 5.22: Velocity field vs. orifice position at x/d=4

Figure 5.23 presents the streamwise velocity profiles of orifice cases in comparison to the cylindrical case. The evolution of each case can be clearly observed. The in-hole position of the orifice shows evident influence on jet penetration characteristics. When the orifice moves deeper into the injection hole, jet trajectory demonstrates a lowering trend as the velocity peak gradually moves towards the surface. W50P45 features the lowest jet penetration among the orifice cases due to its deepest in-hole position, but the difference with W50P30 is small, especially in far downstream region. In addition to jet penetration, the orifice has an effect on the near-surface jet velocity as well. W50P45 shows not only the lowest penetration, but also the highest velocity near the surface and the most evident catch-up phenomenon. This means that it forms a merged jet bulk earlier than in the other cases, and the jet bulk is better attached to the surface yielding more surface coverage. Yet, the velocity peak magnitude is found to be inversely proportional to jet penetration height. In other words, the profile of a high penetrating jet features high velocity peak magnitude and low near-surface velocity, which is clear after $x/d = 5$. This is explained by the conservation of mass, since the amount of fluid in each case is identical. The streamwise velocity profiles of case W50P00 bears two velocity peaks at $x/d = 0$, but the lower peak disappears rapidly due to strong entrainment of low velocity mainstream. The two peaks originate from the two velocity peaks at the hole exit, as shown in Figure 5.21. The upstream peak develops to the upper peak in the velocity profile when the jet is bended by the mainstream.

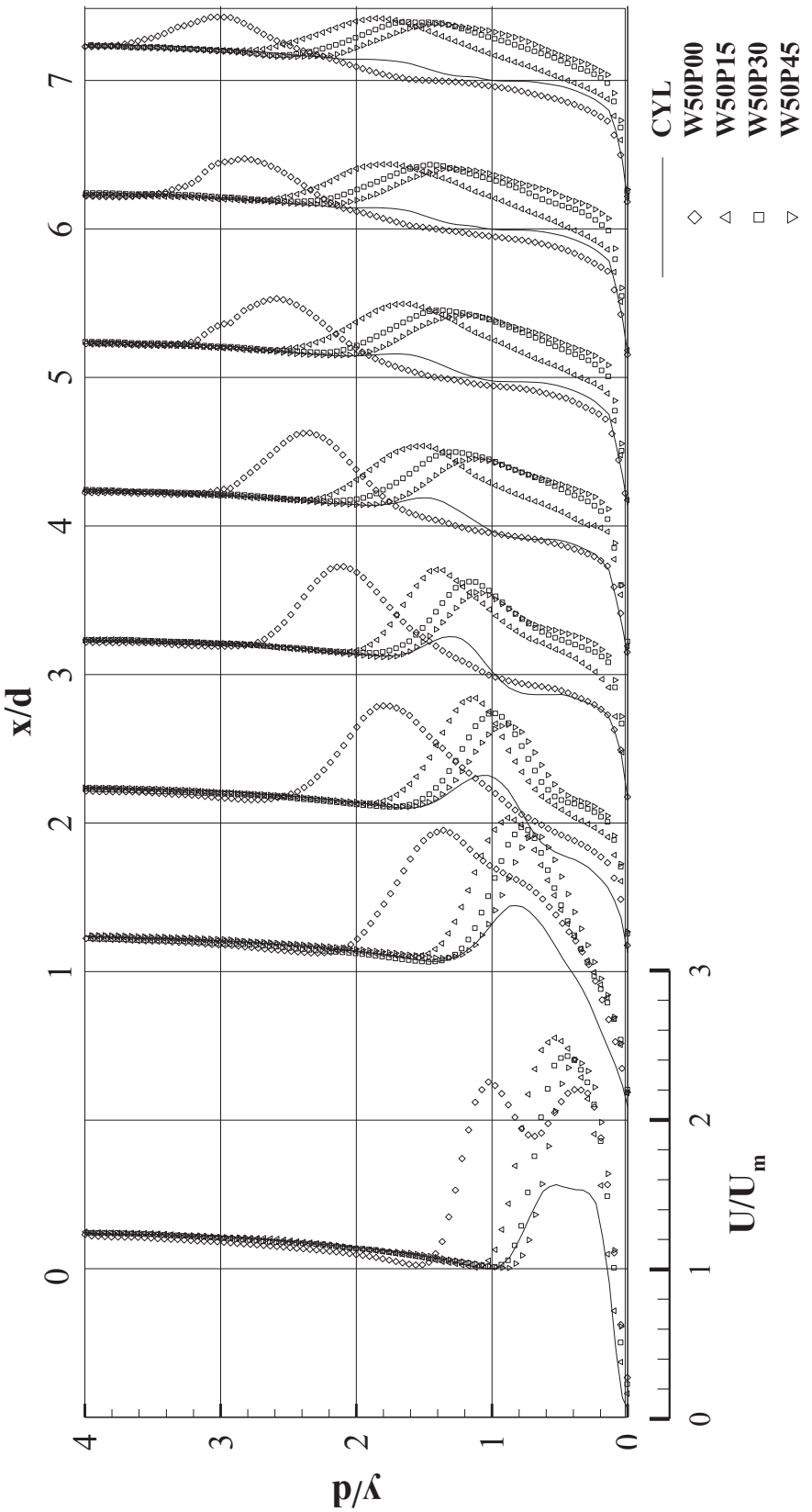

Figure 5.23: Velocity profiles vs. orifice position

The streamwise velocity iso-surfaces of each orifice case are presented in Figure 5.24. The jet penetration of case W50P00 is clearly much higher than that of the others. The core velocity iso-surface hits a high position and the under the jet, the loose iso-surfaces indicate strong mainstream entrainment and an obvious kidney-shaped structure. At the far downstream end, the jet bulk of W50P0 diffuses to a large area due to the introduction of large amount of mainstream fluid. On the other hand, the core iso-surfaces of those cases with deep-positioned orifices show much lower trajectories. In those cases, the iso-surfaces near the centre plane do not indicate major mainstream entrainment.

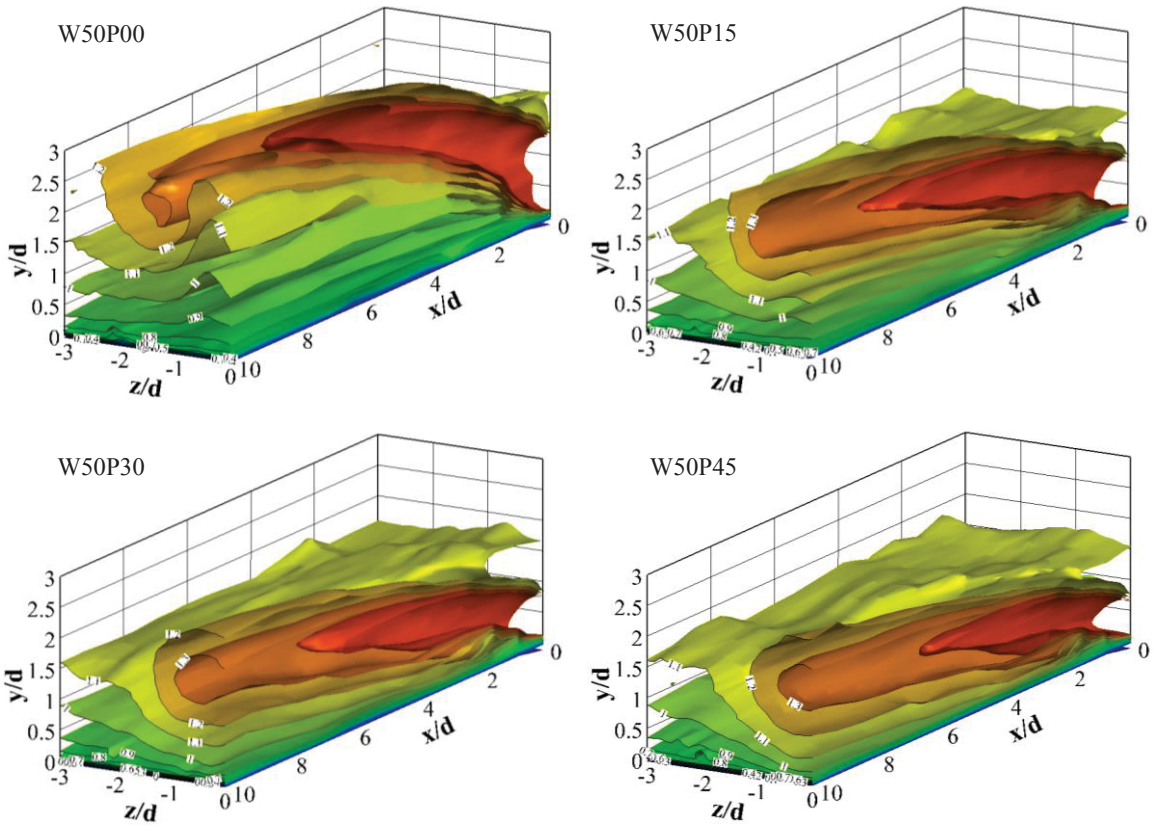

Figure 5.24: Velocity iso-surfaces of cases of orifice width variation

5.7.3 Vorticity fields

The high penetrating jet of W50P00 leaves a large space under the jet to develop strong CRVP, as shown in Figure 5.25. The extensive vorticity zone of the case is actually a double-decker vortex structure with a negative Q value in the middle. The double-decker vortex phenomenon becomes less evident as the orifice moves to a deeper position inside the injection hole. This phenomenon is mostly related to the existence of two U/U_m peaks at hole exit though it is only clear in the W50P00 case. Each velocity peak in W50P00 features a vortex pair. The upper and lower pairs have the same rotational sense and equivalent intensity, as the two velocity peaks share the same magnitude, as shown in Figure 5.23. In those cases of deeper-positioned orifice, the upstream U/U_m peak already dissipates at the hole exit. It can be seen that the upper pair becomes less evident when the orifice moves to deeper positions and creates higher velocity downstream of the hole due to bending. At the same time as the orifice position varies, jet penetration abates and CRVP cores move to a lower position, as in Figure 5.20.

It can be concluded that the orifice position also has a considerable effect on the downstream flow field structure and CRVP strength, and consequently a potential influence on film cooling performance. The main effect of the orifice is that it determines when the acceleration and the following deceleration of the secondary stream occur before being injected into mainstream. With an orifice at a deep in-hole position, the secondary stream decelerates so that it is bended and pushed forwards by mainstream easily, as in case W50P45. The late occurrence of orifice

throat effect makes the secondary stream penetrate into mainstream with high wall-normal momentum, since the fluid cannot decelerate enough. The high wall-momentum leads to less bending of the jet, resulting in extraordinary jet lift-off, as in case W50P00. The effect of orifice position on CRVP strength is related to the jet penetration characteristics. For a high jet trajectory, more space exists below the jet for CRVP to develop and entrain more mainstream fluid. Lowering the jet trajectory can involve the plate surface to limit CRVP development due to large shear in boundary layer.

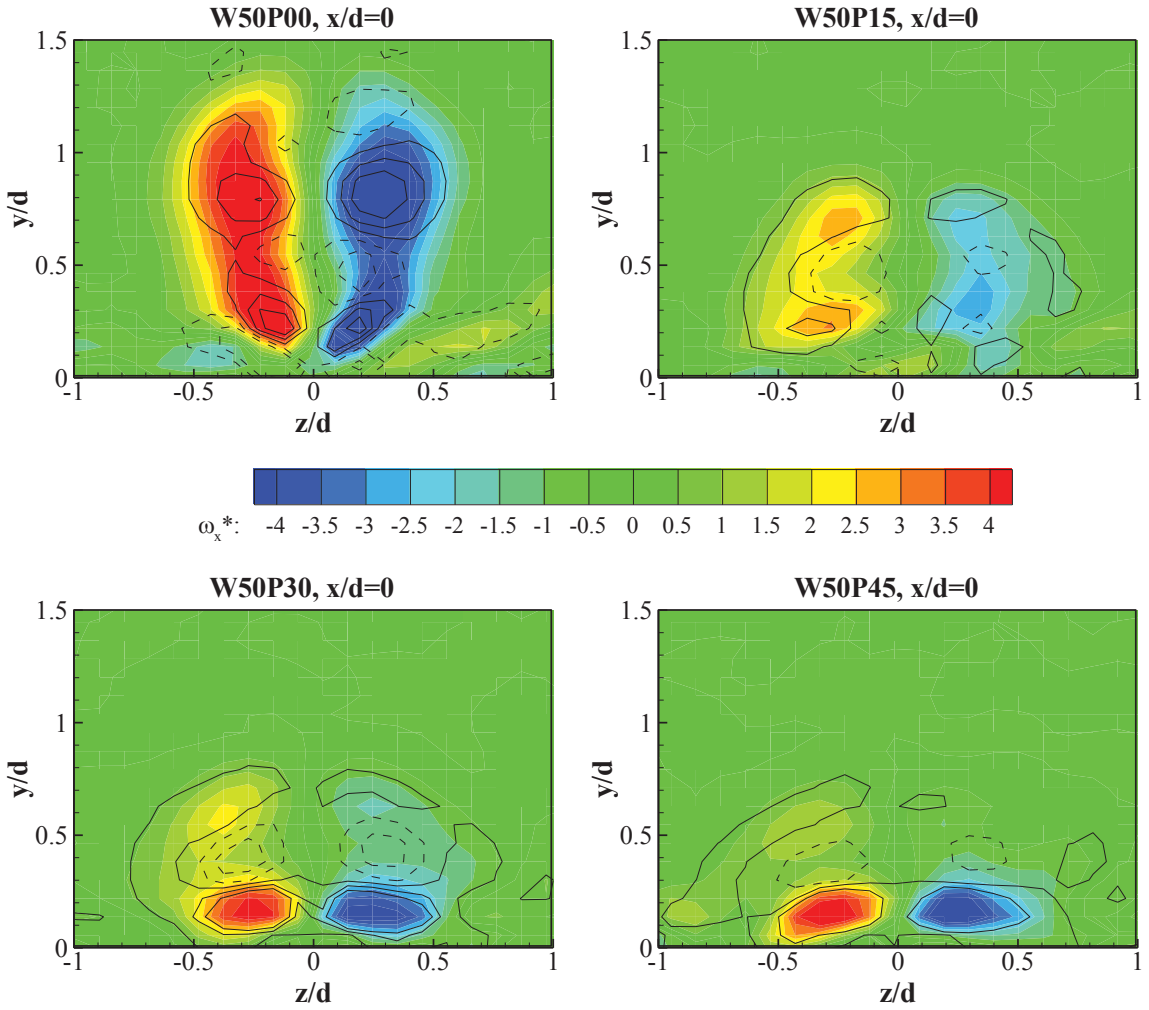

Figure 5.25: Vorticity field vs. orifice position at *x/d*=0

5.8 Summary

An interchangeable test module was designed and fabricated to investigate the effect of principal geometrical parameters of the orifice in the cooling hole. The injection hole length, orifice opening width and in-hole position were of major interest in the investigations. The effect of blowing ratio was also investigated. Seven different parameter combinations were selected to establish an independent analysis of each one. The previous short nozzle hole geometry was tested again under the same mainstream conditions in this phase to provide a comparable reference.

A long injection hole (6d) is reported capable of eliminating the reversed flow present in the near-hole exit region downstream of the short nozzle hole. Jet merging occurs earlier at the same blowing ratio in long injection hole cases due to the absence of reversed flow after injection. The blowing ratio variation is found to have little impact on jet structure, but considerable influence on velocity magnitude. A narrower opening orifice provides lower downstream CRVP strength. The orifice position on the other hand has a major impact on jet penetration. An orifice at a deep position inside injection hole features the lowest jet trajectory, while low jet penetration is reported to help reduce CRVP strength. The CRVP suppressing mechanism in orifice cases is attributed to the elimination of hanging vortices and the elimination of in-hole vortices. In using orifices to weaken CRVP in inclined JICF applications, a combination of a narrow opening and deep position would be recommended.

Chapter 6

Conclusions and Future Directions

6.1 Conclusions

As a new film cooling hole geometry featuring an orifice, referred to as a nozzle hole, has been proposed and demonstrated to improve cooling performance in previous numerical studies, the scheme draws interests in the sole effect of CRVP on cooling characteristics. The flow field of a short nozzle hole, which was the original geometry in the previous numerical study, was investigated experimentally and compared with a cylindrical injection hole across low and high blowing ratios of 0.5, 1.0, 1.5 and 2.0 with a fully developed turbulent mainstream. The results reveal that the nozzle hole significantly reduced CRVP strength by an average of 55% within 10d downstream range at a low blowing ratio of 0.5, and by 34%–40% for high blowing ratios of 1.0, 1.5 and 2.0. At the low blowing ratio, the quick diffusion of the jet due to lower momentum and the confining effect of the surface leads to similar jet characteristics for both nozzle and cylindrical injection. Nozzle jet shows double-decker vortices near the hole exit at high blowing ratios, which could cancel out the

vorticity produced after the orifice and consequently influence the growth of downstream CRVP. Less mainstream fluid is found entrained by the weak CRVP of nozzle jet to split the jet bulk as in cylindrical hole injection. The merged jet features a round bulk offering better jet coverage over the surface than the kidney-shaped cylindrical jet did. Effective slope reduction is found in nozzle jet streamlines, though the reduced CRVP of the nozzle jet does not lower vortex core position. The improved coolant coverage is attributed to reduced CRVP strength and the consequent jet-mainstream mix characteristics.

A long version of the nozzle hole is designed in the present study to investigate the mechanism of CRVP suppression by the in-hole orifice and the effect of orifice geometry parameters. The long hole length isolates the influence of short length injection such as strong in-hole separation. The reversed flow that occurs in short orifice hole injection is found absent in long orifice hole injection due to flow recovery from separation. The absence of the reversed flow allows jet merging to occur earlier than in short orifice hole injection. In addition, it is found that in the same category of blowing ratio ($BR = 1.0$ and $BR = 1.5$), the blowing ratio does not have a structural impact on jet flow, though apparent differences in velocity magnitude are observed.

The experimental results provide clues to the mechanism of CRVP suppressing effect of the orifice. It is observed that the orifice plates are able to break the development of in-hole boundary layer vorticity that creates hanging vortices at the lateral edges of the injection hole exit. Apart from eliminating hanging vortices, the orifice is also shown to create high momentum after-orifice flow and opposite

vorticity due to its throat effect and sudden expansion. The after-orifice flow acts against the in-hole vorticity, which is another source of CRVP formation. By eliminating hanging vortices and in-hole vorticity, orifice-featured injection hole debilitates downstream CRVP. The suppressing effect is observed to be stronger with an orifice featuring a narrow opening, for example, in case W36P30, because the narrower opening has a more evident throat effect and generates higher momentum and opposite vorticity. In fact, the major contribution of orifice opening width is to influence CRVP strength. The opening width has little effect on jet trajectory, which suggests that CRVP strength would not affect jet penetration characteristics. The jet trajectory is mainly affected by orifice position inside the hole. An orifice at a deeper in-hole position results in a lower jet penetrating trajectory, as shown in case W50P45. Jet penetration could, on the contrary, affect CRVP development. The plate surface produces a strong confining effect on CRVP when jet flows are near the surface. Higher jet penetration provides more room for CRVP to develop without interference of the plate surface, which results in strong CRVP intensity, as seen in case W50P00.

Considering the effect of orifice width and position, a deep-positioned orifice with a narrow opening is the preferred choice in applications aiming to deliver a flat and well-spread jet with low CRVP strength. This preference is also good for short injection holes, as the main flow characteristics far downstream are the same as in the cases without exit reversed flow.

6.2 Future Directions

Future investigations could include the following improvements and directions:

- To better understand the CRVP suppressing effect of an orifice, more emphasis could be focused on the in-hole flow structure. Developing new measurement techniques would be necessary.
- The effect of design parameters of an orifice might not affect the flow structure monotonically. For deeper orifice positions, a long channel after the orifice might recover the in-hole flow to a level similar to a cylindrical jet. An excessively narrow orifice would cause strong resistance and choke in the injection hole. Determining the optimal design parameters would be important.
- The strong after-orifice vorticity dissipates quickly after injection and few traces are seen further downstream. An in-depth investigation of this dissipation would help better understand the flow field downstream of an orifice.

Publications

Journal

Zheng, Yingjie and Hassan, Ibrahim, “Experimental Flow Field Investigations of a Film Cooling Hole Featuring Orifice”, Applied Thermal Engineering, 62(2), pp. 766-776, 2014.

Conference

Zheng, Yingjie and Hassan, Ibrahim, “Experimental Flow Field Investigations of Nozzle Film Cooling Scheme on a Flat Plate Using Stereo PIV”, ASME Summer Heat Transfer Conference, Minneapolis, MN, USA, 2013.

References

Aga, V. and Abhari, R. S., Influence of Flow Structure on Compound Angled Film Cooling Effectiveness and Heat Transfer, J. Turbomach., 133:031029 (12 pp.), 2011.

Aga, V., Rose, M. and Abhari, R. S., Experimental flow structure investigation of compound angled film cooling, J. Turbomach., 130:031005-1-8, 2008.

An, B., Liu, J., Zhang, C. and Zhou, S., Film cooling of cylindrical hole with a downstream short crescent-shaped block, J. Heat Transfer, 135:031702 (9 pp.), 2013.

Asghar, F. H. and Hyder, M. J., Computational study of film cooling from single and two staggered rows of novel semi-circular cooling holes including coolant plenum, Energy Conversion and Management, 52:329-334, 2011.

Azzi, A., Abidat, M., Jubran, B. A. and Theodoridis, G.S., Film cooling predictions of simple and compound angle injection from one and two staggered rows, Numerical Heat Transfer, 40:273-94, 2001.

Azzi, A. and Jubran, B. A., Numerical modelling of film cooling from converging slot-hole, Heat and Mass Transfer, 43:381-8, 2007.

Bernsdorf, S., Rose, M. G. and Abhari, R. S., Experimental validation of quasisteady assumption modeling of unsteady film-cooling, J. Turbomach., 130:2008.

Brittingham, R. A. and Leylek, J. H., A detailed analysis of film cooling physics: Part IV- Compound-angle injection with shaped holes, J. Turbomach., 122:133-145, 2000.

Bruce-Black, J., Davidson, F. T., Bogard, D. G. and Johns, D. R., Practical slot configurations for turbine film cooling applications, 2009 ASME Turbo Expo, June 8, 2009 - June 12, 3:607,Orlando, FL, United states, 2009.

Bunker, R. S., A review of shaped hole turbine film-cooling technology, J. Heat Transfer, 127:441-453, 2005.

Dai, K. Y., Liu, G. R., Lim, K. M. and Gu, Y. T., Comparison between the Radial Point Interpolation and the Kriging Interpolation Used in Meshfree Methods, Comput.Mech., 32:60-70, 2003.

Dhungel, A., Lu, Y., Phillips, W., Ekkad, S. V. and Heidmann, J., Film cooling from a row of holes supplemented with antivortex holes, J. Turbomach., 131:1-10, 2009.

Elnady, T., Hassan, I., Kadem, L. and Lucas, T., Cooling effectiveness of shaped film holes for leading edge, Exp.Therm.Fluid Sci., 44:649-661, 2013.

Farhadi-Azar, R., Ramezanizadeh, M., Taeibi-Rahni, M. and Salimi, M., Compound triple jets film cooling improvements via velocity and density ratios: Large eddy simulation, J Fluids Eng- Trans ASME, 133:031202 (13 pp.), 2011.

Fric, T. F. and Roshko, A., Vortical structure in the wake of a transverse jet, J. Fluid Mech., 279:1-47, 1994.

Ghorab, M. G., Hassan, I. G. and Lucas, T., An experimental investigation of film cooling performance of louver scheme, Int. J. Heat Mass Transfer, 54:1387-1399, 2011.

Graf, L. and Kleiser, L., Flow-field analysis of anti-kidney vortex film cooling, J. Thermal Science, 21:66-76, 2012.

Graf, L. and Kleiser, L., Large-Eddy Simulation of double-row compound-angle film cooling: Setup and validation, Computers and Fluids, 43:58-67, 2011.

Hada, S., Tsukagoshi, K., Masada, J. and Ito, E., Test Results of the World's First 1,600C J-series Gas Turbine, Mitsubishi Heavy Industries Technical Review, 49:18-23, 2012.

Haller, G., An objective definition of a vortex, J. Fluid Mech., 525:1-26, 2005.

Haven, B.A. and Kurosaka, M., Kidney and anti-kidney vortices in crossflow jets, J. Fluid Mech., 352:27-64, 1997.

Heidmann, J. D., A numerical study of anti-vortex film cooling designs at high blowing ratio, Proc. ASME Turbo Expo, 4:789, Germany, 2008.

Heidmann, J. D. and Ekkad, S., A novel antivortex turbine film-cooling hole concept, J. Turbomach., 130:1-9, 2008.

Hyams, D. G. and Leylek, J. H., A detailed analysis of film cooling physics: Part III-Streamwise injection with shaped holes, J. Turbomach., 122:122-132, 2000.

Hyung, H. C., Rhee, D. H. and Kim, B.G., Enhancement of film cooling performance using a shaped film cooling hole with compound angle injection, Fluids and Thermal Engineering, 44:99-110, 2001.

Issakhanian, E., Elkins, C. J. and Eaton, J. K., In-hole and mainflow velocity measurements of low-momentum jets in crossflow emanating from short holes, Exp.Fluids, 53:1765-1778, 2012.

Kampe, T. A. D., Volker, S., Samel, T., Heneka, C., Ladisch, H., Schulz, A. and Bauer, H., Experimental and Numerical Investigation of Flow Field and Downstream Surface Temperatures of Cylindrical and Diffuser Shaped Film Cooling Holes, J. Turbomach., 135:011026 (10 pp.), 2013.

Kelso, R. M., Lim, T. T. and Perry, A. E., An experimental study of round jets in cross-flow, J. of Fluid Mech., 306:111-44, 1996.

Kusterer, K., Bohn, D., Sugimoto, T. and Tanaka, R., Double-jet ejection of cooling air for improved film cooling, J. Turbomach., 129:809-815, 2007.

Li, H., Hassan, O. and Hassan, I., The Effects of Counter-rotating Vortex Pairs' Intensity on Film Cooling Effectiveness, Proc. of the ASME IMECE, Energy and Water Scarcity, Denver, CO, USA, 2011.

Ligrani, P. M., Wigle, J. M., Ciriello, S. and Jackson, S. M., Film-cooling from holes with compound angle orientations. Part 1. Results downstream of two staggered rows of holes with 3d spanwise spacing, J. Heat Transfer, 116:341-352, 1994a.

Ligrani, P. M., Wigle, J. M. and Jackson, S. W., Film-cooling from holes with compound angle orientations. Part 2. Results downstream of a single row of holes with 6d spanwise spacing, J. Heat Transfer, 116:353-362, 1994b.

Liu, C., Zhu, H., Bai, J. and Xu, D., Film cooling performance of converging slot-hole rows on a gas turbine blade, Int. J. Heat Mass Transfer, 53:5232-41, 2010.

Marzouk, Y. M. and Ghoniem, A. F., Vorticity structure and evolution in a transverse jet, J.Fluid Mech., 575:267-305, 2007.

Miao, J. and Wu, C., Numerical approach to hole shape effect on film cooling effectiveness over flat plate including internal impingement cooling chamber, Int. J. Heat Mass Transfer, 49:919-938, 2006.

Oldfield, M. L. G. and Lock, G. D., UK patent 9821639.3,. Coolant Passages for Gas Turbine Components, 1998.

Porter, J. S., Sargison, J. E., Walker, G. J. and Henderson, A. D., A comparative investigation of round and fan-shaped cooling hole near flow fields, J. Turbomach., 130:2008.

Raffel, M., Willert, C. and Kompenhans, J. 2002, Particle Image Velocimetry - A Praticle Guide, Springer, p.22.

Recker, E., Bosschaerts, W., Wagemakers, R., Hendrick, P., Funke, H. and Börner, S., Experimental study of a round jet in cross-flow at low momentum ratio, 15th Int Symp on Applications of Laser Techniques to Fluid Mechanics, Lisbon, Portugal, 2010.

Sargison, J. E., Guo, S. M., Oldfield, M. L. G., Lock, G. D. and Rawlinson, A. J., A converging slot-hole film-cooling geometry-Part 1: Low-speed flat-plate heat transfer and loss, J. Turbomach., 124:453-460, 2002.

Sargison, J. E., Oldfield, M.L.G., Guo, S. M., Lock, G. D. and Rawlinson, A.J., Flow visualisation of the external flow from a converging slot-hole film-cooling geometry, Experiments in Fluids, 38:304-318, 2005.

Schlegel, F., Wee, D., Marzouk, Y. M. and Ghoniem, A. F., Contributions of the wall boundary layer to the formation of the counter-rotating vortex pair in transverse jets, J. Fluid Mech., 676:461-490, 2011.

Shinn, A. F. and Pratap Vanka, S., Large eddy simulations of film-cooling flows with a micro-ramp vortex generator, J. Turbomach., 135:011004 (13 pp.), 2013.

Walters, D. K. and Leylek, J. H., A detailed analysis of film-cooling physics: Part I-Streamwise injection with cylindrical holes, J. Turbomach., 122:102-112, 2000.

Westerweel, J., Dabiri, D. and Gharib, M., Effect of a Discrete Window Offset on the Accuracy of Cross-correlation Analysis of Digital PIV Recordings, Exp. Fluids, 23:20-28, 1997.

Wilcock, R. C., Young, J. B. and Horlock, J. H., The effect of turbine blade cooling on the cycle efficiency of gas turbine power cycles, J. Eng. Gas. Turb. Power, 127:109-120, 2005.

Zaman, K. B. M. Q., Rigby, D. L. and Heidmann, J. D., Experimental study of an inclined jet-in-cross-flow interacting with a vortex generator, 48th AIAA Aerospace Sciences Meeting Including the New Horizons Forum and Aerospace Exposition, Orlando, FL, USA, 2010.